Université du Québec à Chicoutimi

Télésurveillance des changeurs de prises en charge (CPC) pour transformateurs de puissance

par Fataneh Dabaghi Zarandi

Thèse présentée à l'Université du Québec à Chicoutimi en vue de l'obtention du grade de Philosophiae Doctor (Ph. D.) en ingénierie

Jury :

Prof. Stephan Brettschneider, Département des sciences appliquées à l'UQAC, Président du Jury

Dr. Hossein Hemmatjou, Transformateurs Delta Star, Inc., Membre externe

Dr. Naivonirina Ravelomanantsoa, EXP, Membre externe

Prof. Issouf Fofana, Département des sciences appliquées à l'UQAC, Membre interne

Prof. Hassan Ezzaidi, Département des sciences appliquées à l'UQAC, Membre interne

Dr. Patrick Picher, Hydro-Québec Research Institute (IREQ), Membre interne

Québec, Canada

Résumé

Le transformateur est un composant critique du système électrique, comprenant diverses parties. Un élément essentiel est le Changeur de Prise en Charge (CPC), qui régule le niveau de tension. Récemment, la gestion des défauts de ce composant est devenue une préoccupation majeure pour prévenir les pannes des transformateurs. Selon la littérature, environ 20 % des défauts de transformateurs sont dus à des défaillances des CPC. Par conséquent, la détection précoce des défauts de ce composant peut prévenir les pannes des transformateurs. Cette thèse vise à utiliser l'analyse des signaux vibro-acoustiques pour surveiller le CPC en temps réel et déclencher une alarme en cas de changements dans les enveloppes des signaux de vibration.

Cette technique implique de mesurer les signaux de vibration du CPC à l'aide d'un accéléromètre. De plus, d'autres paramètres, tels que la température (en raison de son impact sur les signaux de vibration), sont également mesurés. Ce système de surveillance a été installé sur trois transformateurs du réseau Hydro-Québec, et les signaux vibro-acoustiques sont surveillés en continu depuis 2016.

Il est important de noter que les signaux de vibration sont complexes et contiennent une quantité importante d'informations. L'extraction de l'enveloppe du signal est utilisée pour obtenir l'enveloppe à partir du signal de vibration. Dans cette thèse, la transformée de Hilbert et le filtre passe-bas (LPF) sont appliqués pour extraire l'enveloppe du signal. La température influence les enveloppes des signaux vibro-acoustiques, créant un décalage temporel et d'amplitude entre les enveloppes. Pour comparer les enveloppes des signaux de vibration, la technique de réalignement temporel de premier ordre est appliquée pour supprimer le décalage temporel entre les enveloppes.

Pour analyser les enveloppes des signaux vibro-acoustiques mesurés, il est nécessaire d'en extraire des caractéristiques. Cette thèse se concentre sur l'extraction des principaux pics de chaque enveloppe. En fonction de la position du pic principal, plusieurs zones clés sont identifiées dans les enveloppes des signaux. En calculant la distance euclidienne pour chaque zone et chaque pic situé dans chaque enveloppe par rapport à une enveloppe de référence, il devient possible de détecter des changements dans les enveloppes. L'extraction des principaux pics et zones ainsi que le calcul de la distance euclidienne facilitent la détection, l'identification, la localisation et le suivi des changements dans les enveloppes. De plus, les principaux pics et zones présentant des changements au fil du temps sont automatiquement sélectionnés à l'aide de la régression linéaire et du R^2.

Bien que les parties changeantes dans les enveloppes aient été automatiquement détectées, il est difficile de déterminer la date exacte du début des changements. Pour détecter cela, une détection des anomalies doit être appliquée. Dans cette thèse, un autoencodeur convolutionnel profond est utilisé pour identifier les anomalies dans les distances euclidiennes calculées en temps réel à partir des zones des enveloppes. Enfin, trois types d'alarmes, y compris les anomalies négligeables, les changements à long terme et les altérations significatives, sont introduits.

En outre, plusieurs paramètres statistiques sont calculés pour chaque zone, et les plus adaptés sont sélectionnés sur la base de la régression linéaire, du R^2 et de la valeur-p.

Il convient de noter que des enveloppes sont également analysées à l'aide d'un autoencodeur variationnel convolutionnel (CVAE), avec les objectifs de visualisation 2D des enveloppes, de génération des enveloppes et de détection des anomalies. Le CVAE compresse les enveloppes en un espace latent bidimensionnel, une représentation de dimension inférieure capturant les caractéristiques essentielles des données. Dans ce contexte, les enveloppes peuvent être affichées sur un graphique bidimensionnel, offrant une visualisation basée sur la température ou les années. De plus, il est possible de générer des enveloppes avec ou sans anomalies à partir de différents points dans l'espace latent. Enfin, les anomalies peuvent être détectées et un seuil optimal est déterminé.

Finalement, les méthodologies et les résultats de cette thèse font progresser le domaine de la surveillance des CPC par l'analyse des signaux vibro-acoustiques. Ces réalisations facilitent l'extraction des caractéristiques des enveloppes des signaux de vibration, ainsi que la détection, la localisation et l'identification des changements dans les enveloppes. De plus, l'application de l'apprentissage profond permet la détection

précoce des anomalies, la génération des enveloppes et la visualisation 2D des enveloppes. En outre, les changements à long terme et les variations soudaines ont été détectées.

Abstract

The transformer is a critical component of the electric power system, comprising various parts. The On-Load Tap Changer (OLTC) is an essential component that regulates the voltage level. Recently, addressing the faults of this component has become a major concern to prevent transformer outages. According to the literature, around 20% of transformer faults are due to OLTC failures. Therefore, early detection of faults in this component can prevent transformer failures. This thesis aims to use the technique of vibro-acoustic signal analysis to monitor the OLTC in real time and trigger an alarm in case of changes in vibration signal envelopes.

This technique involves measuring vibration signals from the OLTC using an accelerometer. Other parameters, such as temperature (which impacts vibration signals), are also measured. This monitoring system was installed on three transformers in the Hydro-Québec network, and vibro-acoustic signals have been continuously monitored since 2016.

Notably, vibration signals are complex and contain a significant amount of information. Signal envelope extraction is used to obtain the envelope from the vibration signal. In this thesis, the Hilbert transform and low-pass filter (LPF) are applied to extract the signal envelope. Temperature influences vibro-acoustic signal envelopes and creates a time and amplitude displacement between envelopes. To compare vibration signal envelopes, the first-order time-realignment technique is applied to remove time displacement between envelopes.

To analyze the vibro-acoustic signal envelopes measured, it is necessary to extract features from them. This thesis focuses on extracting the main peaks from each envelope. Based on the position of the main peak, several key zones are identified within the signal envelopes. By calculating the Euclidean distance for each zone and peak located in each envelope relative to a reference envelope, it becomes possible to detect changes in the envelopes. Extracting main peaks and zones and computing the Euclidean distance facilitates the detection, identification, localization, and tracking of changes in the envelopes. Furthermore, the main peaks and zones exhibiting changes over time are automatically selected using linear regression and R^2.

Although the changing parts in envelopes were automatically detected, it is challenging to pinpoint the exact date when changes began. To detect this, anomaly detection must be applied. In this thesis, a deep convolutional autoencoder is used to identify anomalies in computed Euclidean distances from zones within the envelopes in real time. Finally, three alarms, including ignorable anomalies, long-term changes, and significant alterations, are introduced.

Furthermore, several statistical parameters are computed for each zone, and the best-fit statistical parameters are selected based on linear regression, R^2, and P-value.

It should be noted that the envelopes are also analyzed using a Convolutional Variational Autoencoder (CVAE), with the objectives of 2D visualization of envelopes, generating envelopes, and detecting anomalies. The CVAE compresses the envelopes into a two-dimensional latent space, which is a lower-dimensional representation capturing the essential features of the data. In this regard, envelopes can be displayed on a two-dimensional graph, providing a visualization based on temperature or years. Additionally, it is possible to generate envelopes with or without anomalies from different points in the latent space. Finally, anomalies can be detected, and an optimal threshold is determined.

Finally, the methodologies and results from this thesis advance the field of OLTC monitoring through vibro-acoustic analysis. These achievements facilitate the extraction of features from vibration signal envelopes, as well as the detection, localization, and identification of changes in the envelopes. Additionally, the application of deep learning enables the early detection of anomalies, generation of envelopes, and 2D visualization of envelopes. Furthermore, long-term changes and sudden variations have been detected.

Table des matières

Liste des tableaux

Liste des figures

Liste des abréviations et acronymes

CPC : Changeur de Prises en Charge
DRM : Mesure de la Résistance Dynamique
DGA : Analyse des Gaz Dissous dans l'huile
LPF : Filtre Passe-Bas
VMD : Décomposition en Modes Variationnels
SMA : Moyenne Mobile Simple
WMA : Moyenne Mobile Pondérée
EMA : Moyenne Mobile Exponentielle
CWT : Transformée en Ondelettes Continue
DWT : Transformée en Ondelettes Discrète
WPT: Transformée en Paquets d'Ondelettes
EMD : Décomposition en Modale Empirique
HSA : Analyse Spectrale de Hilbert
IMF : Fonctions Modales Intrinsèques
FFT: Transformée de Fourier Rapide
SVM : Machine à Vecteurs de Support
GA-SVM : Machines à Vecteurs de Support Optimisées par Algorithme Génétique
ED : Distance Euclidienne
KDE : Estimation Par Noyau
MSE : Erreur Quadratique Moyenne
RNN : Réseau Neuronal Récurrent
LSTM : Mémoire à Long Terme et Court Terme
OCC : Classification à Une Classe
PCC : Coefficient de Corrélation de Pearson
RMS : Racine Carrée de la Moyenne des Carrés
Kurt : Kurtosis
Skew : Asymétrie
SD : Écart-type
Min: Opérateur min()
Max : Opérateur max()
Minmax : Opérateur min(max())
AAD : Différence Moyenne Absolue
ASLE : Somme Absolue des Erreurs Logarithmiques
Cov : Covariance
CUSUM: Cumulative Sum
SOM : Carte Auto-Organisatrice
MQE : Erreur de Quantification Minimale
LIFO : Dernier Entré, Premier Sorti
AE : Autoencodeur
VAE : Autoencodeur Variationnel
CVAE : Autoencodeur Variationnel Convolutionnel
CNN : Réseau Neuronal Convolutionnel

List of abbreviations and acronyms

OLTC : On-Load Tap Changer
DRM : Dynamic Resistance Measurement
DGA : Dissolved Gas-in-oil Analysis
LPF : Low Pass Filter
HHT : Hilbert–Huang Transform
VMD : Variational Mode Decomposition
SMA : Simple Moving Average
WMA : Weighted Moving Average
EMA : Exponential Moving Average
CWT : Continuous Wavelet Transform
DWT : Discrete Wavelet Transform
WPT : Wavelet Packet Transform
EMD : Empirical Mode Decomposition
HAS : Hilbert Spectral Analysis
IMF : Intrinsic Mode Function
FFT : Fast Fourier Transform
WPD : Wavelet Packet Decomposition
SVM : Support Vector Machine
GA-SVM : Genetic optimization Support Vector Machines
ED : Euclidean Distance
KDE : Kernel Density Estimation
MSE : Mean Squared Error
RNN : Recurrent Neural Network
LSTM : Long Short-Term Memory
OCC : One-Class Classification
PCC : Pearson Correlation Coefficient
RMS : Root Mean Square
Kurt : Kurtosis
Skew : Skewness
SD : Standard Deviation
Min : Min() operator
Max : Max() operator
Minmax : Min(Max()) operator
AAD : Absolute Average Difference
ASLE : Absolute Sum of Logarithmic Error
Cov : Covariance
CUSUM : Cumulative Sum
SOM : Self-Organizing Map
MQE : Minimum Quantization Error
LIFO : Last In, First Out
AE : AutoEncoder
VAE : Variational AutoEncoder
CVAE : Convolutional Variational AutoEncoder
CNN : Convolutional Neural Network

Dédicace

"À mes chers Alireza et Armita."

Remerciements

Je tiens à exprimer ma profonde gratitude à mon directeur de thèse, le Professeur Fofana, pour son accompagnement continu, son soutien, sa motivation et sa bienveillance. Je suis vraiment chanceuse de travailler avec quelqu'un qui est non seulement très compétent, mais qui incarne également les meilleures qualités humaines. J'ai beaucoup appris pendant mes études de doctorat, et pour cela, je suis profondément reconnaissante.

Je remercie sincèrement mes co-directeurs, le Professeur Ezzaidi et le Dr. Picher, pour leur soutien indéfectible et leur bienveillance. Travailler avec eux a été un atout inestimable.

Je tiens à remercier le Dr. Behjat et M. Gauvin pour leurs précieux retours et leur soutien technique durant ma recherche.

Je voudrais également exprimer ma gratitude à la Chaire de recherche sur le vieillissement des infrastructures des réseaux électriques (ViAHT), qui a non seulement facilité le développement de précieuses amitiés, mais a aussi apporté un soutien financier tout au long du projet. Je tiens également à remercier mes amis pour leur soutien et leurs encouragements. En particulier, je remercie Marie Lucia Yapi, Ghada Gmati, Jayasree Thota, U. Mohan Rao, Mouloud Bouzar, Esther Ogwa Obebe, Samson Okikiola, et tous ceux qui ont contribué.

Je souhaite exprimer ma sincère gratitude à ma famille pour leur soutien indéfectible pendant mes études de doctorat. Je tiens à remercier chaleureusement ma fille, Armita, mon mari, Alireza, ainsi que mes parents et ma sœur Fahimeh.

Chapitre I
Introduction générale

1.1. Introduction

Un des composants importants dans les systèmes électriques et les réseaux de distribution est le transformateur. Il est donc crucial de détecter les défauts de cet équipement à un stade précoce pour éviter les pannes [1-3]. Le changeur de prises en charge (CPC) dans les transformateurs joue un rôle essentiel dans la régulation de la tension en ajustant le nombre de tours dans un enroulement. La Figure I.1 montre les pourcentages de pannes dans chaque composant du transformateur. Comme il est évident, le CPC est la troisième cause la plus courante de pannes, après les enroulements et les traversées [4]. Par conséquent, la surveillance continue de ce dispositif est essentielle pour assurer le bon fonctionnement et la fiabilité du système de transformateur.

Il convient de noter que la plupart des CPC utilisent un principe de commutation mécanique. Dans ces systèmes, le changement de position de prise se fait sans interruption de courant. Cependant, si un CPC utilise un seul contact de commutation pendant l'opération du changeur de prises, le courant sera interrompu jusqu'à ce que le contact se connecte à la position de prise finale. Par conséquent, le concept de contact "fermer avant d'ouvrir" est recommandé pour prévenir les interruptions de courant. Avant de rompre le contact avec la position de prise primaire, la position de prise finale est connectée, permettant au commutateur de se connecter simultanément à deux prises, créant ainsi un courant de circulation. Pour limiter ce courant de circulation, une impédance de transition est appliquée sous forme de réactance ou de résistance [5-7].

Les pannes du CPC peuvent survenir en raison de causes mécaniques ou électriques. La plupart des pannes sont causées par des défaillances mécaniques telles que le desserrage des contacts, le blocage du mécanisme de fonctionnement, le glissement des engrenages, etc. [8-10].

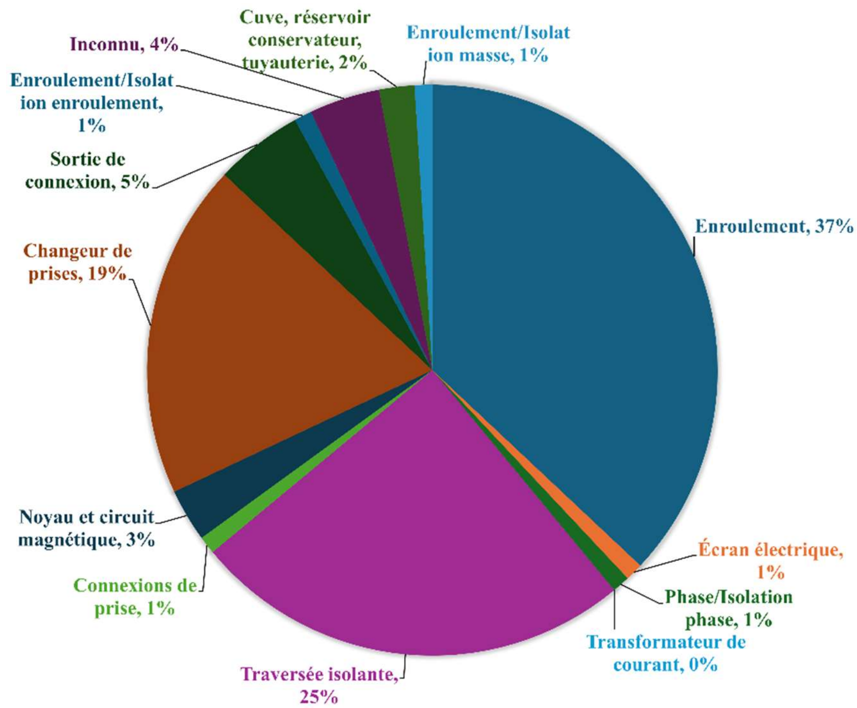

Figure I.1 Les pourcentages de pannes dans les composants du transformateur [4].

Plusieurs techniques sont utilisées pour détecter les pannes du CPC. Les plus applicables et pratiques sont brièvement expliquées ci-après [11-14].

- **Mesure de la résistance dynamique (DRM):** Cette méthode est utilisée comme une approche hors ligne. Dans ce cadre, des informations sur l'état du CPC sont obtenues sans le retirer du réservoir principal. Ces données aident à déterminer le taux d'usure des contacts.
- **Analyse des gaz dissous dans l'huile (DGA):** Le test d'analyse des gaz dissous dans l'huile est utilisé comme méthode en ligne. Cette méthode utilise des gaz tels que l'hydrogène (H_2), le méthane (CH_4), l'éthane (C_2H_6), l'éthylène (C_2H_4), l'acétylène (C_2H_2) et le monoxyde de carbone (CO) pour détecter les pannes du CPC.
- **Analyse des signaux vibro-acoustiques:** Cette technique est utilisée en ligne et en temps réel. Les pannes du CPC sont détectées en analysant les ondes acoustiques générées par ses composants.

- **Analyse de la tension-courant du moteur et des signaux vibro-acoustiques:** Certaines méthodes utilisent les paramètres du courant d'entraînement du moteur et des signaux vibro-acoustiques pour détecter les pannes du CPC. Des caractéristiques telles que le temps de commutation, les délais entre le démarrage du moteur et la commutation, l'amplitude, etc., peuvent être surveillées en utilisant ces paramètres.
- **Analyse vibro-arc:** Il convient de noter que le fonctionnement du CPC produit des signaux d'arc en plus des signaux de vibration. Dans [15, 16], ces deux types de signaux ont été utilisés pour détecter les pannes du CPC.
- **Analyse du courant de commutation:** Cette méthode permet d'identifier les défaillances des contacts, les défaillances des résistances de transition et d'autres défaillances mécaniques.
- **Analyse de la puissance d'arc:** L'analyse de la puissance d'arc est utilisée comme méthode en temps réel. Dans cette approche, la quantité de puissance et d'énergie d'arc peut être calculée en utilisant la tension aux bornes d'entrée et de sortie de chaque phase et le courant traversant chaque phase. Ensuite, ces valeurs sont utilisées pour détecter les pannes du CPC.

Chacune des techniques ci-dessus peut détecter certaines pannes du CPC [11, 17-19], comme expliqué dans le Tableau I.1 Comme mentionné, les méthodes de détection existantes sont classées en trois catégories : hors ligne, en ligne et en temps réel.

Dans cette thèse, nous nous concentrons sur les méthodes basées sur l'analyse des signaux vibro-acoustiques pour trois raisons. Premièrement, cette approche est utilisée comme méthode en ligne et en temps réel. Dans ce contexte, les signaux vibro-acoustiques sont obtenus sans affecter les opérations du CPC et du transformateur [15]. Deuxièmement, les pannes du CPC peuvent être détectées très tôt, car il est possible de mesurer en continu et de détecter tout changement dans les ondes acoustiques. Enfin, cette approche devrait permettre de détecter de nombreux types de pannes dans un CPC [20].

Tableau I.1 Les techniques utilisées pour surveiller le CPC.

Nom de la technique	Catégorie	Type de panne
DRM	Hors ligne	Cette méthode peut détecter les pannes du CPC telles que l'érosion des contacts, les interruptions de commutation et les problèmes de dégradation.
DGA	Hors ligne et en ligne	Cette méthode est très efficace pour détecter les défauts diélectriques et les dégradations.
Analyse des signaux vibro-acoustiques	En ligne et en temps réel	Cette méthode peut découvrir de nombreuses pannes mécaniques qui peuvent survenir dans un CPC.
Analyse de la tension-courant du moteur et des signaux vibro-acoustiques	En ligne	Cette méthode peut bien détecter les pannes du CPC, y compris les déviations de temps causées par l'usure des contacts, des problèmes de lubrification ou de synchronisme.
Analyse vibro-arc	En ligne	Cette méthode peut détecter les pannes dues à l'usure électrique des contacts d'arc du CPC.
Analyse du courant de commutation	En ligne	Cette méthode peut détecter certaines pannes, telles que la panne des bornes de contact, la panne des résistances de transition et certaines pannes mécaniques.
Analyse de la puissance d'arc	En temps réel	Cette méthode peut détecter l'usure électrique des contacts d'arc liée à la commutation du CPC.

1.2. Motivation et objectifs de la recherche

Le CPC génère des signaux de vibration presque similaires lorsque ses composants effectuent un mouvement. Lorsqu'une panne se produit, ces signaux changent. Par conséquent, les pannes du CPC peuvent être détectées en analysant ces signaux [21]. De plus, la surveillance continue aide à détecter tout changement de condition mécanique en comparant les derniers signaux mesurés aux anciens. Dans ce contexte, si des différences sont observées, un changement de condition mécanique peut être détecté. Cette approche est connue sous le nom de méthode "avant-après" [22].

Il existe une préoccupation nécessitant des investigations supplémentaires concernant la surveillance des CPC par l'analyse des signaux vibro-acoustiques. Les principales lacunes incluent la détection automatique des changements au fil du temps, la subdivision automatique des signaux en plusieurs parties, l'application de techniques d'apprentissage profond pour détecter les anomalies et l'évaluation des signaux vibro-acoustiques sur la base de paramètres statistiques. La présente recherche vise à combler ces lacunes existantes dans la surveillance des CPC en utilisant l'analyse des signaux vibro-acoustiques pour les améliorer ou les résoudre. À cet égard, l'objectif général est d'analyser le comportement des OLTC basé sur les signaux vibro-acoustiques. Pour atteindre cet objectif général, les objectifs spécifiques suivants ont été définis :

1. Extraction des principaux pics et zones des enveloppes de signal, et sélection automatique des pics et zones présentant des changements au fil du temps.
2. Détection des comportements anormaux dans les CPC à l'aide d'algorithmes d'apprentissage profond, et identification des changements à long terme ainsi que des variations soudaines dans les enveloppes de signal.
3. Extraire les paramètres statistiques les plus adaptés aux variations temporelles de l’enveloppe du signal vibro-acoustique.
4. Examiner les enveloppes des signaux de vibration au fil du temps, générer des enveloppes de signaux de vibration et détecter des anomalies dans les enveloppes de signal.

1.3. Originalité de la recherche

L'avantage principal de cette thèse par rapport aux travaux existants réside dans l'analyse d'un ensemble de données unique dérivé de l'étude des signaux vibro-acoustiques pour examiner les CPC. Contrairement à la littérature existante, qui se concentre principalement sur des données simulées, de laboratoire ou à court terme en conditions réelles, cette thèse se distingue par la mesure continue des enveloppes de signaux sous des conditions opérationnelles réelles de 2016 à 2023. Les méthodologies appliquées à ces données posent des défis significatifs en raison de leur complexité et nécessitent une analyse approfondie et pertinente. Les principales contributions de cette thèse peuvent être soulignées comme suit :

Dans l'analyse des signaux vibro-acoustiques, les principaux pics jouent un rôle crucial dans l'évaluation du comportement du CPC [23-25]. Connaître leur nombre, leur amplitude et le délai temporel entre eux permet de détecter des changements, ce qui aide à identifier les pannes d'un CPC [23].

- En extrayant les principaux pics des enveloppes de signal, les principales zones sont identifiées en fonction de leur position.
- De plus, les zones et les pics qui présentent des changements au fil du temps sont sélectionnés automatiquement.

Dans la surveillance des CPC par l'analyse des signaux vibro-acoustiques, l'application des méthodes d'apprentissage profond est insuffisamment développée. Bien que certains travaux aient utilisé l'apprentissage automatique pour évaluer le comportement des CPC [26, 27], il existe une lacune dans la détection des changements aux premiers stades. Afin d'adresser cette lacune, la thèse propose la solution suivante :

- Dans cette thèse, un autoencodeur convolutionnel profond est utilisé pour détecter les anomalies. En conséquence, trois types d'alarmes sont introduits : anomalies négligeables, changements à long terme et altérations significatives.
- Par ailleurs, un autoencodeur variationnel convolutionnel profond est utilisé pour analyser les enveloppes de signal au fil du temps et pour générer de nouvelles enveloppes de signal. Il est également appliqué pour détecter les anomalies, avec plusieurs seuils testés afin d'identifier le seuil optimal pour la détection des anomalies.

Une autre lacune dans la surveillance des CPC par les signaux vibro-acoustiques réside dans l'évaluation de leur comportement à travers des paramètres statistiques calculés à partir des enveloppes de vibration.

- Calculer certains paramètres statistiques connus à partir des zones des enveloppes des signaux de vibration et sélectionner automatiquement les plus adaptés.

1.4. Organisation de la thèse

Cette thèse est une thèse par articles et est organisée autour les objectifs spécifiques énoncés dans la section 1.2. Ces objectifs spécifiques ont été atteints avec succès grâce à la publication de trois articles de recherche dans des revues prestigieuses. L'organisation de cette thèse est expliquée comme suit:

Le premier chapitre fournit une introduction générale au CPC et à ses méthodes de surveillance. Il aborde également l'originalité et les objectifs de la thèse.

Le chapitre 2 présente une revue de la littérature. Il explique les types de CPC, leurs composants, les pannes, et les approches de surveillance CPC basées sur l'analyse des signaux vibro-acoustiques.

Le troisième chapitre présente le premier objectif spécifique. Une méthodologie est utilisée pour extraire les principaux pics des enveloppes des signaux de vibration. Les principales zones sont identifiées en fonction de la position de ces pics. La distance Euclidienne (ED) est calculée pour chaque zone et chaque pic principal. Enfin, le pic ou la zone montrant des changements au fil du temps est automatiquement sélectionné en appliquant la régression linéaire et du R^2. Il convient de mentionner que ce chapitre correspond à un article déjà publié dans une revue prestigieuse.

Le chapitre 4 décrit le deuxième objectif spécifique, qui consistent à appliquer l'apprentissage profond pour détecter les anomalies dans les caractéristiques extraites des enveloppes de signaux vibro-acoustiques. Dans ce cadre, un autoencodeur convolutionnel profond est utilisé pour obtenir la valeur de reconstruction de l'entrée. De plus, l'estimation par noyau (KDE) est appliquée pour établir des seuils et des scores d'anomalie. Des anomalies ont été détectées, ce qui a conduit à la création de trois types d'alarmes : anomalies négligeables, changements à long terme et altérations significatives, qui aident à évaluer l'état global du CPC. Il convient de mentionner que ce chapitre correspond à un article déjà publié dans une revue prestigieuse.

Le chapitre 5 présente le troisième objectif spécifique. Quelques paramètres statistiques connus sont calculés pour chaque zone située dans les enveloppes de signaux. Ensuite, les plus adaptés sont sélectionnés en appliquant la régression linéaire, la valeur-p et du R^2.

Le sixième chapitre présente le dernier objectif spécifique : examiner les enveloppes des signaux de vibration au fil du temps, générer des enveloppes de signaux de vibration et détecter des anomalies dans ces enveloppes. À cet égard, un autoencodeur variationnel convolutionnel profond est utilisé. Son architecture comprend un encodeur avec des couches permettant d'obtenir un espace latent bidimensionnel. Par la suite, toutes les enveloppes peuvent être tracées sur une figure bidimensionnelle en fonction des données de l'espace latent. De plus, en utilisant l'espace latent, il est possible de générer des enveloppes de signal. Dans le décodeur, des couches en miroir de l'encodeur sont disposées de manière inverse pour obtenir la valeur de reconstruction de l'entrée. Ensuite, en calculant l'erreur de reconstruction, il est possible de détecter des anomalies. Il convient de noter que plusieurs seuils sont testés et qu'un seuil optimal pour la détection des anomalies est identifié. Il convient de mentionner que ce chapitre correspond à un article déjà publié dans une revue prestigieuse.

Le chapitre 7 détaille les résultats et contributions de la recherche, offrant une exploration approfondie des découvertes. De plus, il décrit les travaux futurs potentiels, ouvrant la voie à des avancées continues dans le domaine de la surveillance des CPC.

Chapitre II

Revue de la littérature

Dans cette section, nous décrivons les types de CPC et leurs composants. De plus, les types de pannes sont expliqués. Enfin, nous décrivons en détail l'approche d'analyse des signaux vibro-acoustiques.

2.1. Types de CPC, composants et pannes

Le fonctionnement principal du CPC consiste à sélectionner une autre position de prise sans interruption du courant [5]. Il transfère le courant de la position de prise primaire à la position de prise finale. Si un CPC utilise un commutateur à contact unique lors d'un changement de prise, le courant sera inévitablement coupé. Pour résoudre ce problème, le concept de contact "fermer avant d'ouvrir" est proposé. Selon ce concept, lors de l'opération de commutation, la connexion à la position de prise finale se fait avant la déconnexion de la position de prise primaire. Ainsi, le commutateur se connecte à deux prises en même temps, créant un courant de circulation. Pour limiter ce courant, l'impédance de transition est mise en œuvre avec soit une résistance, soit une réactance [6].

2.1.1. Types de CPC

Les CPC peuvent être classés en deux types selon l'impédance de transition utilisée : les CPC de type Résistance et ceux de type réactance, expliqués ci-dessous.

- **CPC de type Résistance :** Ce type de dispositif est utilisé dans les transformateurs de puissance haute tension et est installé à l'intérieur du réservoir du transformateur. De plus, ce type est utilisé dans la plupart des CPC existants en Europe [6, 7]. Il convient de noter que le schéma représentant un CPC de type résistance est présenté dans la référence [28].
- **CPC de type réactance :** Ce type de dispositif est utilisé dans les transformateurs de puissance basse tension. La plupart des CPC aux États-Unis sont conçus selon ce modèle et sont situés dans un

compartiment séparé, normalement soudé au réservoir du transformateur [6]. Il convient de noter que le schéma représentant un CPC de type réactance est présenté dans la référence [28].

Il existe différents types de commutateurs utilisés dans les CPC. Ces commutateurs incluent principalement le commutateur de dérivation et le commutateur de sélection, qui sont expliqués ci-dessous.

- **Commutateur de dérivation:** Aussi appelé commutateur d'arc ou commutateur de transfert, ce dispositif inclut un commutateur de dérivation et un sélecteur de prises. Il comporte deux ensembles de contacts : des contacts mobiles et des contacts fixes. Le commutateur de dérivation, considéré comme un contact fixe, porte le courant, tandis que le sélecteur de prises, considéré comme un contact mobile, est connecté à une prise présélectionnée et ne porte pas le courant.

  Pour le changement de prise, le commutateur de dérivation est connecté à la prise primaire (la prise qui porte le courant) et doit être remplacé par le changeur de prise final, sélectionné et connecté par le sélecteur de prises. Ensuite, le commutateur du CPC est connecté à deux prises en même temps, la résistance de transition est utilisée pour limiter le courant de circulation créé. Le commutateur de dérivation passe ensuite à la prise présélectionnée. Enfin, les étapes de l'opération du changeur de prises sont terminées et le courant est porté en utilisant la prise présélectionnée [6, 7, 29]. Il convient de noter que le changement de prise dans ce commutateur se fait à une vitesse très élevée (40-120 ms) [30].
- **Commutateur de sélection :** Le commutateur de sélection, également appelé commutateur d'arc de prise, effectue une opération de changement de prise en un seul mouvement. Ce dispositif contient trois contacts : le contact principal et deux contacts auxiliaires. Le premier est connecté à la position de prise primaire qui porte le courant, tandis que les contacts auxiliaires ne sont pas connectés. En changeant de prise, le contact principal se déplace vers une autre prise appelée prise finale. Par conséquent, le contact principal est déconnecté de la position de prise primaire et le premier contact auxiliaire est connecté à cette dernière. Ensuite, le deuxième contact auxiliaire est connecté à la prise finale. Ainsi, le commutateur CPC est connecté à deux prises simultanément. Dans ce contexte, le courant de circulation est limité par la réactance de transition des contacts auxiliaires. Après cela, le

premier contact auxiliaire est déconnecté de la position de prise primaire. Enfin, le contact principal est connecté à la prise finale [5, 7, 29].

Il convient de noter que dans le mécanisme d'entraînement, un ressort est utilisé dans le CPC de type résistance pour assurer une commutation rapide et limiter l'échauffement de la résistance, alors qu'un mécanisme lent actionné par un moteur est utilisé pour le type réactance. De plus, chaque type de commutation — le commutateur de dérivation et le commutateur de sélection — peut être utilisé pour les CPC de type résistance ou de type réactance. Par ailleurs, dans certaines conceptions de CPC, la technologie d'interrupteur sous vide est utilisée à la place des contacts d'arc remplis d'huile [7, 31]. Cette technologie peut être utilisé à la fois dans le commutateur de sélection et de dérivation.

Une autre classification des CPC est basée sur le type de technologie employée :

- **CPC de type à huile :** Ce type de CPC est immergé dans l'huile du transformateur et toutes ses opérations de commutation sont effectuées sous l'huile.
- **CPC de type à vide :** Ce dispositif est basé sur la technologie de l'interrupteur à vide, qui a remplacé la technologie à huile. Voici quelques avantages des commutateurs à vide par rapport à ceux à huile [6] :
    - Les CPC de type interrupteur à vide réduisent l'arc électrique lors des changements de prise. Par conséquent, les défauts d'usure des contacts se produisent moins fréquemment dans ces commutateurs par rapport à ceux à huile.
    - Il n'y a pas d'oxydation pendant la commutation.
    - Les CPC de type interrupteur à vide ne nécessitent pas de maintenance pendant toute leur durée de vie.

Enfin, une classification finale des commutateurs de prise en charge est présentée dans la Figure II.1. Comme le montre cette figure, ils sont classés en deux types : à huile et à vide. De plus, chaque type est subdivisé en deux catégories : résistance et réactance. Dans cette thèse, nous visons à détecter les pannes liées aux modèles à huile.

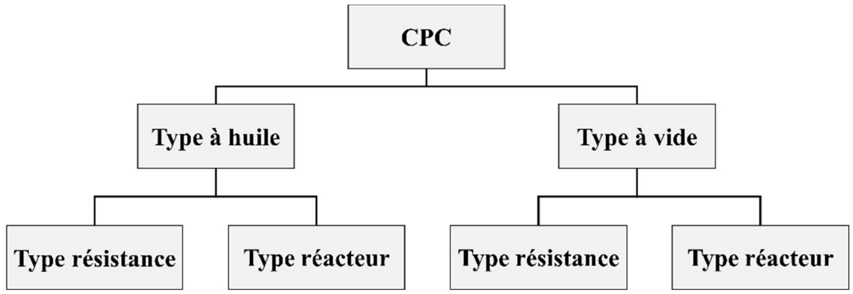

Figure II.1 Classification des types de CPC.

2.1.2. Composants et pannes du CPC

Un CPC se compose de plusieurs composants essentiels qui fonctionnent ensemble pour assurer une régulation efficace de la tension, notamment commutateur principal/d'arc, mécanisme d'entraînement et sélecteur, Inverseur, Commutateur grossier/fin. De plus, les pannes des CPC sont classées en trois groupes en fonction de ces composants : commutateur principal/d'arc, mécanisme d'entraînement et sélecteur, inverseur, commutateur grossier/fin, qui sont expliqués ci-dessous.

- **Commutateur principal/d'arc :** Le contact du commutateur d'arc et celui du sélecteur de prises sont considérés respectivement comme le contact principal et le contact de transition. Le premier est utilisé pour interrompre et connecter le courant, tandis que le second sert à sélectionner une autre position de prise. Dans ce dispositif, le contact principal subit des dommages plus tôt et plus fréquemment que le contact de transition.

  Les pannes des CPC telles que l'arc anormal, l'usure des contacts, le desserrement des contacts, le blocage des contacts, la dégradation de l'huile et la rupture/brûlure peuvent se produire dans le commutateur principal/d'arc [7, 8, 32-34]. Chacune de ces pannes survient pour des raisons spécifiques. Par exemple, le blocage des contacts du CPC peut se produire en raison d'une pression de contact insuffisante [5]. De plus, plus de 60 % des pannes de CPC sont liées aux défauts de desserrement et de blocage des contacts [32]. Un exemple de dégradation des contacts est montré dans la Figure II.2.

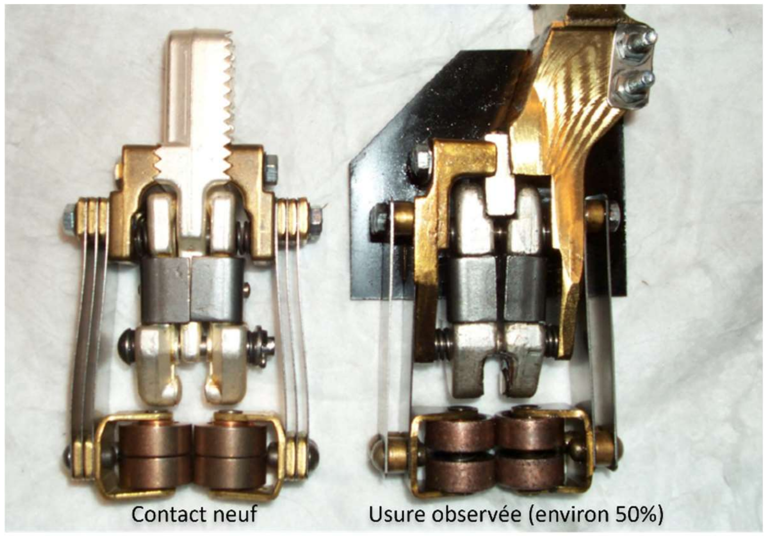

Figure II.2 Le contact neuf et le contact avec 50% d'usure observée [35].

- **Mécanisme d'entraînement :** Dans les CPC, les opérations de changement de prise sont effectuées à l'aide d'un mécanisme d'entraînement qui contient plusieurs composants, y compris une unité d'entraînement moteur, un arbre, un engrenage et un ressort [19]. Dans le commutateur de dérivation, le sélecteur de prises et le commutateur de dérivation fonctionnent respectivement à l'aide d'un engrenage et d'un accumulateur d'énergie à ressort [6]. Un accumulateur d'énergie à ressort est alimenté via l'unité d'entraînement moteur [36]. L'arbre connecte l'entraînement moteur à la tête du changeur de prises.

  Certaines pannes, telles que le glissement des engrenages, le temps de transition lent, le moteur bloqué, le jeu dans l'arbre d'entraînement, la friction et les ressorts faibles, peuvent survenir dans le mécanisme d'entraînement [32, 33].

- **Sélecteur, Inverseur, Commutateur grossier/fin :** Certaines pannes, telles que la friction, la dégradation de l'huile, les décharges/arcs électriques, le film d'huile et la cokéfaction peuvent survenir dans ces parties [33].

2.2. Approche d'analyse des signaux vibro-acoustiques

Dans cette thèse, la technique d'analyse des signaux vibro-acoustiques est utilisée pour détecter les pannes des CPC. Elle se déroule en trois étapes : la collecte, le prétraitement et l'analyse des données pour évaluer l'état du dispositif. Ces étapes sont expliquées ci-dessous.

2.2.1. Collecte des données

Les signaux vibro-acoustiques peuvent être mesurés par deux systèmes : des dispositifs sensibles à la pression sonore, tels qu'un hydrophone immergé dans l'huile, et un transducteur sensible au mouvement, tel qu'un accéléromètre. Un hydrophone immergé dans l'huile mesure le niveau de pression sonore, tandis qu'un accéléromètre capte les signaux vibro-acoustiques, tous deux générés par le fonctionnement du CPC. Lors d'un test, ces signaux ont été enregistrés simultanément à l'aide des deux dispositifs. Les données comparées ont montré que les signaux sonores et vibro-acoustiques sont très similaires et contiennent suffisamment d'informations pour détecter les pannes du CPC [37]. Il convient de noter que la plupart des propositions existantes utilisent des accéléromètres.

Dans le processus de collecte des signaux vibro-acoustiques, l'emplacement de montage et la gamme de fréquences de l'accéléromètre sont des facteurs très importants pour mesurer correctement les signaux de vibration. Ces facteurs sont expliqués ci-dessous.

- **Le lieu de montage de l'accéléromètre :** Les accéléromètres doivent être placés à un endroit approprié pour bien mesurer les signaux de vibration. Par exemple, chez Hydro-Québec, un capteur vibro-acoustique a été monté sur le réservoir du CPC près du commutateur de dérivation [21].
- **La plage de fréquence de l'accéléromètre :** Les accéléromètres avec différentes plages de fréquence peuvent être utilisés pour mesurer les signaux de vibration. Dans [38], des capteurs haute fréquence (50 kHz à 400 kHz) et basse fréquence (0,2 Hz à 15 kHz) ont été utilisés. Montés à proximité sur le CPC, ils ont mesuré simultanément les signaux. Les résultats ont

montré que le capteur haute fréquence captait tous les signaux générés par le CPC, tandis que le capteur basse fréquence ne les mesurait pas tous.

Le Tableau II.1 indique la plage de fréquence des accéléromètres utilisés dans certaines propositions connexes. Ce tableau comporte trois colonnes : Référence, Année et Plage de fréquence. La colonne Référence affiche le numéro de référence de l'article. La colonne Année représente l'année où la proposition a été faite et la colonne Plage de fréquence montre la plage de fréquence des accéléromètres utilisés.

Tableau II.1 Plage de fréquence des accéléromètres utilisés dans certaines propositions connexes.

Référence	**Année**	**Plage de fréquences**
[23]	2009	1 - 12 kHz
[25]	2010	1 - 12 kHz
[39]	2014	0.8 - 15 kHz
[15]	2017	50 – 400 kHz
[22]	2018	50 - 150 kHz
[40]	2018	50 - 400 kHz
[41]	2018	1-13kHz
[42]	2019	1-13 kHz
[27]	2023	100–900 kHz

2.2.2. Prétraitement

Comme mentionné, les signaux vibro-acoustiques du CPC sont mesurés à l'aide d'un accéléromètre. Ces signaux, de par leur complexité, ne sont pas directement utilisables pour la détection et l'analyse des défauts. Par conséquent, un prétraitement est nécessaire pour réduire leur complexité et les préparer à l'analyse. Les étapes de prétraitement incluent la normalisation, la synchronisation des signaux et l'extraction de l'enveloppe, expliquées ci-dessous.

- **Normalisation et synchronisation des signaux :** Dans les opérations de CPC, il existe une différence significative entre les amplitudes des pics principaux et le temps entre ces pics dans les signaux mesurés au même point de prise initiale et finale du CPC à différents moments. Pour comparer ces signaux, une normalisation est nécessaire, obtenue en utilisant leur valeur quadratique moyenne (RMS). Ainsi, un signal peut être normalisé en utilisant l'Équation (II.1) [23].

$$Vib_{normal}[\mathrm{n}] = \frac{Vib[\mathrm{n}]}{RMS_{vib}} = \frac{Vib[\mathrm{n}]}{\sqrt{\sum_{i=1}^{N}\left[\mathrm{Vib[i]}\right]^2}} \tag{II.1}$$

Où $Vib[\mathrm{n}]$ détermine le signal de vibration d'origine et n représente le nombre total d'échantillons dans $Vib[\mathrm{n}]$. $Vib_{normal}[\mathrm{n}]$ est le signal de vibration normalisé.

De plus, il existe un décalage temporel entre les deux signaux de vibration. Pour les comparer dans le domaine temporel, il est nécessaire de les synchroniser [23]. Une technique utilisée pour la synchronisation des signaux est le réalignement temporel de premier ordre. Cette technique considère un signal comme référence et réaligne l'autre jusqu'à atteindre le coefficient de corrélation maximum [43].

- **Extraction de l'enveloppe du signal :** Les signaux de vibration d'origine sont complexes et non linéaires. Pour une meilleure analyse, ces signaux doivent être simplifiés. L'une des approches les plus courantes utilisées pour simplifier les signaux est l'extraction de l'enveloppe du signal, qui génère un signal lisse basé sur le signal d'origine. Ci-dessous, plusieurs filtres et méthodes utilisés pour extraire une enveloppe de signal sont présentés. La transformation de Hilbert, le filtre passe-bas (LPF), la moyenne mobile, le filtre de Savitzky-Golay, la transformée en Ondelette, la Transformée de Hilbert-Huang (HHT) et la décomposition en modes variationnels (VMD) sont expliqués.
  - **Transformée de Hilbert :** Ce filtre est appliqué comme un filtre linéaire spécial. Il ne modifie pas l'amplitude des composants spectraux mais décale les phases du signal de 90 degrés [38]. La transformée de Hilbert est calculée par l'Équation (II.2).

$$H[x(t)] = \tilde{x}(t) = \pi^{-1} \int_{-\infty}^{\infty} \frac{x(\tau)}{t-\tau} d\tau \tag{II.2}$$

Où $x(t)$ est le signal d'origine.

- **LPF:** Ce filtre utilise une fréquence de coupure pour lisser les signaux d'origine. Il laisse passer les signaux dont la fréquence est inférieure à cette fréquence de coupure et atténue ceux dont la fréquence est supérieure [38].
- **Moyenne Mobile :** Ce filtre reçoit en entrée un nombre de M échantillons sur une période de temps donnée et calcule la moyenne de ces échantillons. La valeur moyenne est considérée comme un point de sortie du signal à ce moment-là. Ce filtre est utilisé pour le domaine temporel et n'est pas adapté au domaine fréquentiel. Le filtre à moyenne mobile est considéré comme un filtre passe-bas ou passe-haut. Il existe en plusieurs types, notamment la Moyenne Mobile Simple (SMA), la Moyenne Mobile Pondérée (WMA) et la Moyenne Mobile Exponentielle (EMA) [44].
- **Filtre de Savitzky-Golay :** Le filtre de Savitzky-Golay est utilisé pour obtenir des signaux lisses à partir de signaux d'origine, basé sur une approximation polynomiale locale par moindres carrés. Ce filtre extrait une enveloppe de signal tout en préservant les pics et les largeurs du signal de vibration d'origine et en éliminant les composants de bruit [15, 22]. Les paramètres du degré du polynôme (N) et de la taille de la fenêtre de données (2M+1) doivent être déterminés. Si le degré du polynôme (N) est augmenté, l'erreur de l'approximation par moindres carrés est réduite. Ainsi, les résultats du filtre de Savitzky-Golay seront plus proches du signal d'origine [22].
- **Transformée en Ondelette :** La transformée en ondelettes est une technique mathématique et une méthode efficace pour les signaux non stationnaires. Elle décompose un signal en plusieurs niveaux de résolution inférieure en contrôlant les facteurs d'échelle et de décalage d'une fonction ondelette unique appelée ondelette

mère. La transformée en ondelettes comprend plusieurs types dont l'un doit être choisi en fonction du type d'application [45]. Ces types incluent la Transformée en Ondelettes Continue (CWT), la Transformée en Ondelettes Discrète (DWT) et la Transformée en Paquets d'Ondelettes (WPT) [46], expliquées ci-dessous.

1. **Transformée en Ondelettes Continue :** La transformée en ondelettes continue d'un signal continu $x(t)$ est calculée par l'équation ci-dessous.

$$CWT(a,b) = \frac{1}{\sqrt{a}} \int_{-\infty}^{+\infty} x(t)\psi^{*}\left(\frac{t-b}{a}\right) dt \qquad \text{(II.3)}$$

   Où a et b présentent respectivement les échelles et les décalages temporels d'une ondelette mère ψ, et ψ^{*} est le conjugué complexe de l'ondelette mère.

2. **Transformée en Ondelettes Discrète :** La DWT est utilisée pour obtenir des informations temps-échelle d'un signal et est adapté aux signaux non stationnaires. Le coût computationnel de la méthode DWT est inférieur à celui de la méthode CWT.

   La DWT décompose le signal d'origine en deux parties : les coefficients d'approximation (basse fréquence) et les coefficients de détail (haute fréquence), au premier niveau de décomposition [46]. Ensuite, seule la partie d'approximation est à nouveau décomposée. Cette procédure continue aux niveaux suivants pour obtenir le niveau de décomposition souhaité.

3. **Transformée en Paquets d'Ondelettes :** Dans la DWT, la partie des coefficients de détail n'est pas décomposée à partir du premier niveau, ce qui entraîne la perte d'informations significatives sur les modes haute fréquence. Pour résoudre ce problème, la WPT est proposée, étendant la décomposition aux hautes fréquences. La WPT décompose à chaque niveau à la fois les parties des coefficients d'approximation et de détail [47].

Il existe plusieurs types d'ondelettes mères, chacune pouvant être utilisée dans la transformée en ondelettes, générant ainsi différents résultats pour le même signal. Choisir la meilleure ondelette mère pour obtenir le meilleur résultat est un défi majeur de la transformée en ondelettes. Un autre défi est de déterminer le niveau de décomposition optimal.

- **Transformée de Hilbert-Huang :** La transformée de Hilbert-Huang est une méthode efficace pour les signaux non linéaires et non stationnaires. Elle se compose de deux parties : la Décomposition en Modale Empirique (EMD) et l'Analyse Spectrale de Hilbert (HSA). L'EMD décompose un signal en une série de composantes appelées Fonctions Modales Intrinsèques (IMF) afin de réduire la nature non stationnaire du signal [48-50]. Ensuite, une représentation "temps-fréquence-énergie" est générée en appliquant la HSA aux IMF [51].
- **Décomposition en Modes Variationnels (VMD) :** Cette méthode est utilisée pour les signaux non stationnaires et non linéaires. L'objectif de la VMD est de décomposer un signal non stationnaire en un nombre discret de sous-signaux stationnaires, chacun ayant des caractéristiques spécifiques [52].

2.2.3. Analyse des données pour évaluer l'état du CPC

Le CPC génère des signaux vibro-acoustiques uniques lorsque ses composants bougent, et ces signaux changent en cas de défaillance. Ainsi, leur analyse permet de détecter les pannes [21]. Une surveillance continue du CPC permet d'identifier les changements de condition mécanique en comparant les signaux récents aux anciens. Si des différences apparaissent, des changements de condition mécanique dans le CPC peuvent être détectés. Cette approche est connue sous le nom de méthode "avant-après" [22].

De plus, la relation entre deux signaux peut être calculée à l'aide du coefficient de corrélation. La valeur du coefficient de corrélation varie de -1 à +1. Une valeur de -1 (ou proche) indique une forte relation négative, tandis qu'une valeur de 1 (ou proche) indique une forte relation positive. Une valeur de 0 (ou proche) signifie qu'il n'y a pas de relation significative. Les coefficients de corrélation les plus courants incluent ceux de Pearson, Spearman et Kendall [53-57]. Dans [22, 38], le coefficient de corrélation de Spearman, calculé à l'aide de l'Équation (II.4), est utilisé pour déterminer la corrélation entre les formes d'onde.

$$CC = \frac{\sum_{i=0}^{N-1}(Y(i) - \bar{Y})(R(i) - \bar{R})}{\sqrt{\sum_{i=0}^{N-1}(Y(i) - \bar{Y})^2 \sum_{i=0}^{N-1}(R(i) - \bar{R})^2}} \tag{II.4}$$

Où Y et R représentent deux formes d'onde simplifiées et $\bar{Y}$ et $\bar{R}$ sont la moyenne de chaque signal.

Il existe plusieurs approches pour détecter les défauts du CPC en utilisant des signaux vibro-acoustiques. Dans plusieurs travaux [23-25, 58], le comportement du CPC est évalué en se basant sur l'extraction des pics des enveloppes de signaux vibro-acoustiques. Les informations sur le nombre de pics, leurs amplitudes et le décalage temporel entre eux peuvent être utilisées pour détecter les défauts.

Dans [59], la WPT est appliquée pour traiter et analyser les signaux de vibration, obtenant des paramètres multi-résolution de bande efficace à l'aide des coefficients de paquets d'ondelettes. Ensuite, la méthode GA-SVM est utilisée pour classifier les informations de vibration mécanique et identifier l'état du CPC.

Dans [60], trois types de défauts du CPC sont étudiés : desserrement des contacts statiques, desserrement des contacts mobiles, insuffisance d'énergie dans les ressorts de stockage, ainsi que la condition normale. Pour évaluer l'état mécanique du CPC, les caractéristiques texturales dans les diagrammes de récurrence dérivés des signaux de vibration sont analysées.

Dans [22], une méthode de comparaison des formes d'onde est proposée pour détecter les changements de condition mécanique à chaque position de prise du CPC. Pour chaque position, la courbe d'enveloppe est extraite du signal de vibration mesuré à l'aide du filtre de Savitzky-Golay. En l'absence de données mesurées antérieures pour une méthode de comparaison "avant-après", tous les signaux de vibration sont comparés entre eux pour évaluer l'état de chaque position de prise. Une forme d'onde de base est sélectionnée initialement. Le coefficient de corrélation de Spearman entre les courbes d'enveloppe est calculé. La courbe d'enveloppe ayant le coefficient moyen le plus élevé est alors choisie comme courbe d'enveloppe de référence. En comparant la courbe d'enveloppe de chaque position de prise avec cette référence, les changements dans son état mécanique peuvent être déterminés.

Dans [38], l'état de chaque position de prise est évalué malgré l'absence de données antérieures sur les signaux de vibration du CPC. Deux types de filtres, la transformée de Hilbert et le LPF, sont utilisés pour extraire l'enveloppe du signal. Une forme d'onde de base est déterminée en calculant les coefficients de corrélation de Spearman entre chaque forme d'onde de position et les autres. La forme d'onde avec la moyenne de corrélation la plus élevée est sélectionnée comme référence. L'état de chaque position est ensuite évalué par comparaison avec cette référence.

Dans [61], les contacts nouveaux et anciens du CPC sont analysés. Dans cette étude, la DWT et le coefficient d'énergie sont appliqués pour détecter la dégradation des contacts.

Dans [26], les signaux vibro-acoustiques et les signaux de courant haute fréquence sont utilisés pour évaluer le comportement du CPC. Ces signaux sont mesurés sur la plateforme de test à travers différents états de fonctionnement. La WPT est appliquée pour réduire le bruit. Une analyse de corrélation explore les relations entre les signaux dans divers états. Les caractéristiques sont extraites via la décomposition en modale empirique en Ensemble et la transformée de Hilbert-Huang. Enfin, la classification de l'état des contacts du CPC est réalisée à l'aide de SVM.

Dans [27], l'étude examine divers défauts mécaniques dans les systèmes de CPC, en se concentrant sur l'identification et l'analyse des degrés d'usure des contacts symétriques et asymétriques, ainsi que sur l'évaluation des dommages aux ressorts et des déformations des contacts. Les signaux de vibration du CPC pendant ces défauts sont mesurés et normalisés en les divisant par leur valeur maximale. La DWT est utilisée pour décomposer une forme d'onde en plusieurs composants, et des indicateurs numériques, tels que la moyenne, RMS, le facteur de forme, le facteur de crête, l'écart type et l'asymétrie, sont calculés pour chaque composant. Enfin, plusieurs approches d'apprentissage automatique sont utilisées à des fins de classification, y compris les k plus proches voisins, arbre de décision, forêt aléatoire, SVM, boosting de gradient et adaptive boosting, parmi lesquelles le SVM s'est avéré être le classificateur le plus efficace.

Dans [62], le signal de vibration d'un CPC est segmenté en quatre phases distinctes : démarrage, stockage d'énergie, commutation et arrêt. L'analyse se concentre sur les segments de stockage d'énergie et de commutation, car ils sont plus riches en informations, tandis que les segments de démarrage et d'arrêt sont généralement exclus. Les caractéristiques sont extraites à l'aide de la Transformée de Fourier Rapide (FFT) et une méthode à bande de largeur égale est introduite pour segmenter le spectre de fréquence. Cette méthode, comparée à WPT et EMD, offre une plus grande simplicité et précision dans la détection des défauts. De plus, l'étude intègre des caractéristiques temporelles telles que l'accélération moyenne des vibrations, l'indice de consommation d'énergie et l'écart type du signal de vibration. Ces caractéristiques supplémentaires affinent le processus de diagnostic des défauts, démontrant l'efficacité de la combinaison de plusieurs approches analytiques pour atteindre une haute précision diagnostique avec le SVM pour la classification.

Dans [63], un accéléromètre mesure les signaux de vibration, et des signaux mesurés en laboratoire sont également utilisés. Pour débruiter les signaux, des analyses de paquets d'ondelettes et de spectre singulier sont appliquées. La décomposition du signal et l'extraction des caractéristiques du spectre frontière sont réalisées à l'aide de la transformée de Hilbert-Huang. Enfin, un algorithme amélioré de clustering flou C-means, optimisé par l'algorithme d'optimisation du loup gris, est utilisé pour déterminer l'état anormal du contact du CPC.

Dans [64], un réseau de capteurs sans fil est appliqué pour surveiller les CPC en ligne. Le logiciel de la plateforme embarquée est utilisé pour enregistrer les mesures et les analyser afin de détecter les défauts et autres problèmes. Les signaux de vibration sont décomposés en IMF à l'aide de l'EMD, ce qui facilite la surveillance des CPC. Enfin, ces IMF sont analysés avec la FFT pour évaluer le comportement des CPC et détecter les défauts.

Dans [65], les auteurs identifient un processus de dégradation monotone pour l'usure et la dégradation des contacts. Pour détecter à la fois les petites et grandes variations dans les signaux de vibration, l'article utilise les procédures Cumulative Sum (CUSUM) et Shewhart. De plus, une carte auto-organisatrice (SOM) est utilisée, entraînée avec les signatures de vibration de la condition normale du CPC pour formuler un indice de condition unique. Ainsi, une erreur de quantification minimale (MQE) plus élevée de la SOM indique une probabilité plus élevée de défauts dans le CPC.

Dans [66], le CPC est évalué sur la base des signaux de courant du moteur et des signaux vibro-acoustiques en trois étapes : débruitage du signal de vibration, extraction de l'enveloppe du signal et extraction des caractéristiques des signaux vibro-acoustiques. Plusieurs facteurs causent du bruit dans les signaux de vibration du CPC, notamment les vibrations liées au noyau et au bobinage du transformateur, le filtre à huile du CPC, l'équipement de dissipation de chaleur du transformateur, le moteur d'entraînement du CPC et le bruit créé par l'équipement de test. Les signaux de vibration sont débruités à l'aide du filtrage de Wiener. En appliquant la technique de détection d'enveloppe à diode, les enveloppes des signaux de courant moteur et des signaux de vibration sont extraites. Enfin, des caractéristiques sont extraites des enveloppes du signal de courant moteur et du signal de vibration du CPC, telles que le nombre de points de pic après le démarrage du moteur et avant l'opération de commutation. Ces caractéristiques sont analysées pour détecter les défauts et leurs types.

Dans [67], l'état du CPC est évalué en se basant sur l'EMD dans le domaine temps-fréquence. Les signaux de vibration des défauts tels que le desserrage des contacts et le desserrage des panneaux d'arc sont analysés et comparés aux signaux de vibration normaux.

Dans [68], l'effet du courant de charge sur les signaux de vibration du CPC est analysé. Les signaux du même CPC avec des courants de charge variables sont mesurés. Il est indiqué que le courant de charge n'a pas d'effet significatif sur le domaine temporel. Cependant, si l'amplitude du courant augmente, il y a des changements dans les caractéristiques du domaine fréquentiel.

Chapitre III
Surveillance de l'état des CPC de transformateurs de puissance basée sur l'extraction de caractéristiques à partir des signaux vibro-acoustiques : Pics principaux et distance euclidienne

Article publié dans Sensors, août 2023

doi :10.3390/s23167020

Surveillance de l’état des CPC de transformateurs de puissance basée sur l'extraction de caractéristiques à partir des signaux vibro-acoustiques : Pics principaux et distance euclidienne

Résumé

La détection précoce des défauts des CPC joue un rôle crucial dans la maintenance des transformateurs de puissance, qui sont les composants les plus stratégiques des sous-stations du réseau électrique. Parmi les méthodes de détection des défauts des CPC, l'analyse des signaux vibro-acoustiques est connue pour être une approche performante, capable de détecter de nombreux types de défauts. L'extraction des caractéristiques des enveloppes de signaux vibro-acoustiques mesurés est une approche prometteuse pour diagnostiquer précisément les défauts des CPC. Le présent travail de recherche se concentre sur le développement d'une méthodologie pour détecter, localiser et suivre les changements dans les enveloppes des signaux vibro-acoustiques surveillés en ligne, basée sur l'extraction des pics principaux et l'analyse de la distance euclidienne. Des systèmes de surveillance des CPC ont été installés sur des transformateurs de puissance en service, ce qui a permis l'enregistrement en temps réel d'un riche ensemble de données d'enveloppes de signaux vibro-acoustiques. L'approche proposée a été appliquée à six ensembles de données différents et une analyse détaillée est rapportée. Les résultats démontrent la capacité de l'approche proposée à reconnaître, suivre et localiser les défauts qui provoquent des changements dans les enveloppes des signaux vibro-acoustiques au fil du temps.

Power Transformers OLTC Condition Monitoring Based on Feature Extraction from Vibro-Acoustic Signals: Main Peaks and Euclidean Distance

Abstract

The detection of OLTC faults at an early stage plays a significant role in the maintenance of power transformers, which is the most strategic component of the power network substations. Among the OLTC fault detection methods, vibro-acoustic signal analysis is known as a performant approach with the ability to detect many faults of different types. Extracting the characteristic features from the measured vibro-acoustic signal envelopes is a promising approach to precisely diagnose OLTC faults. The present research work is focused on developing a methodology to detect, locate, and track changes in on-line monitored vibro-acoustic signal envelopes based on the main peaks extraction and Euclidean distance analysis. OLTC monitoring systems have been installed on power transformers in services which allowed the recording of a rich dataset of vibro-acoustic signal envelopes in real time. The proposed approach was applied on six different datasets and a detailed analysis is reported. The results demonstrate the capability of the proposed approach in recognizing, following, and localizing the faults that cause changes in the vibro-acoustic signal envelopes over time.

3.1. Introduction

Power transformers are key components in power transmission and distribution networks and, therefore, it is very important to ensure their safe and reliable operating condition [69-71]. An OLTC is one of the most important components of the power transformer and it is used to regulate the transformer voltage by changing the number of turns in one winding of the transformer (turns ratio). It is reported that around 30% of transformer faults are due to OLTC failures, hence the requirement for a timely condition assessment of this component [13, 21, 72].

Most OLTCs are based on the mechanical switching principle for the selection of the tap position without any interruption in the current. If OLTC uses a single contact switch during a tap-change operation, the current would definitely be cut-off until the switch was connected to the final tap position. To solve the current cut-off problem, the “make before break” contact concept is used. In this regard, a final tap position is bridged before breaking contact from the primary tap position. So, the OLTC switch connects the two taps at the same time and then a circulating current is created. To limit the circulating current, transition impedance is used in the form of a resistor or reactor [5-7].

There are several techniques adopted for the condition monitoring of an OLTC, such as DRM, DGA, vibro-acoustic signals analysis, motor-drive current analysis, etc. [11]. In this research work, vibro-acoustic signals analysis is used to evaluate the OLTC condition. This method is used as an on-line and real-time method, in which the faults are detected by analyzing vibro-acoustic signals generated from OLTC components.

Several approaches have been proposed to detect OLTC faults using vibro-acoustic signal envelopes [22-25, 38, 58]. The authors of references [22, 38] presented a method in which a base waveform is selected by Spearman’s Rank correlation coefficient, and the condition of each OLTC tap position is evaluated by comparing its waveform with the base waveform. In reference [73], all vibro-acoustic signals of the OLTC are split into two parts. Each part is decomposed into 16 sub-components using wavelet packet transform, and the energy entropy of each sub-component is computed to achieve the condition assessment. In several works [23-25, 58], the OLTC condition is evaluated based on the main peak extraction from vibro-acoustic signal envelopes. For example, in reference [24], the bursts are extracted based on the vertical maximum lines of CWT.

It should be noted that each generated vibro-acoustic signal envelope from OLTC consists of several main peaks. In this regard, information about the number of main peaks, their amplitude, and the time delay between individual peaks will help to detect OLTC faults in the early stage [23]. Over time, changes in the amplitude of main peaks and the time lag between the peaks indicate faults in the components that include springs, switching contacts, and gears [16].

The authors of reference [33] describe how the OLTC faults, including contact wear and weak spring, generate vibro-acoustic signal envelopes with higher amplitudes and increased transition time between peaks. The OLTC faults, including tap loosening, tap loss and tap abrasion, cause some changes in the amplitude of the bursts [42].

It is generally believed that an analysis of the main peaks of the vibro-acoustic signal envelopes is a promising approach to evaluate the OLTC condition. However, extracting the main peaks from the signal envelopes is a challenging task. The first challenge is the discrimination of the main peaks' locations, which may be very close to each other. On the other hand, and as another major challenge in main peaks extraction, there may be a variable time shift between the main peaks that occur due to reasons such as gradual contact wear and this displacement makes main peak extraction a challenging task.

To simplify the signal analysis, averaging and time realignment techniques are used to reduce the natural variations between vibro-acoustic signal envelopes of a tap-changer in good conditions [43, 74]. Trending and instantaneous algorithms are used to detect long-term changes and the sudden variation in vibro-acoustic signal envelopes [33]. An index can be used to detect changes over time and provide a metric to compare data related to several sister OLTCs [75].

The current work aims to develop a methodology for the condition monitoring of OLTC based on vibro-acoustic signal envelopes. The proposed method focuses on detecting, localizing, and tracking changes in vibro-acoustic signal envelopes utilizing main peaks extraction and Euclidean distance (ED). However, there are two sub-objectives to attain the major objective of this research. The first is to extract the main peaks from vibro-acoustic signal envelopes. This sub-objective is covered by utilizing the concept of dynamic and static windows which address the amplitude of the main peaks and the zones containing the main peak locations. The second sub-objective is to compute ED between each envelope and a reference envelope. This metric is calculated using the amplitude of the main peaks of each envelope in comparison to the reference envelope. It should be noted that this distance is not computed for the whole signal envelope. The calculation is carried out for all the main peaks existing in the envelopes. In addition, the amount of ED is also calculated for each zone located in each envelope, in comparison with the reference envelope. This metric distance is used to track changes in vibro-acoustic signal envelope patterns over time.

3.2. Data collecting and preprocessing

3.2.1. Data collecting

There are more than 2000 transformers with an average age of nearly 30 years in the Hydro-Québec's network, and approximately half of them are equipped with OLTC. To optimize the maintenance strategies of the transformers, the Hydro-Québec's Research Institute (IREQ) started a research project to monitor power transformers in OLTC. In this regard, the IREQ's technology was industrialized and OLTC monitoring systems were first installed on nine single-phase autotransformers rated 370 MVA, in a service on the Hydro-Québec's electric network [75]. The details about the functional architecture of this monitoring system are explained in reference [74]. This monitoring system measures vibro-acoustic signals and motor current using an accelerometer installed on the surface of the transformer tank near the diverter switch (for OLTC placed in the main transformer tank), and a current clamp around the wire powering the OLTC's motor, respectively. In addition, to characterize the effect of the temperature on the vibro-acoustic signal, the temperature is also measured and recorded on the surface of the tank near the accelerometer. In Figure III.1 (a), the accelerometer and temperature measurement sensors are highlighted with a red rectangle. Figure III.1 (b) shows a zoomed view of the accelerometer and temperature measurement sensors in the box. In Figure III.1 (c), the current clamp sensor is highlighted using a red rectangle. In Figure III.1 (d), the accelerometer and temperature measurement sensors are highlighted using red and green rectangles, respectively. The back of the transformer monitoring unit (TMU), which records the measurements, is shown in Figure III.2. This TMU computes, saves, and transmits, via a communication system, the envelopes of the motor current and vibro-acoustic signal, and other parameters such as the tap position and the temperature. The TMU's output can also be correlated with other data such as the transformer top-oil temperature.

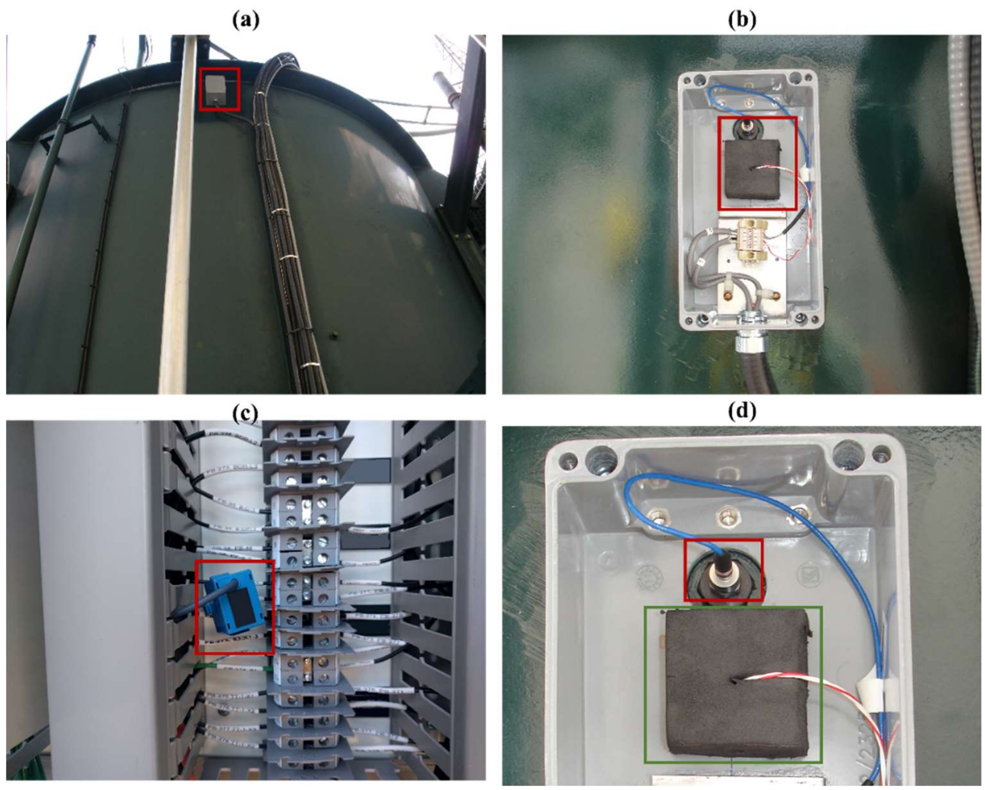

Figure III.1 Installation of the accelerometer, temperature, and the current clamp sensors: (a) the box where the accelerometer and temperature measurements are installed is highlighted with a red rectangle; (b) a zoomed view of the accelerometer and temperature measurements in the box; (c) the current clamp sensor; (d) the accelerometer and temperature measurement sensors (red and green rectangles, respectively).

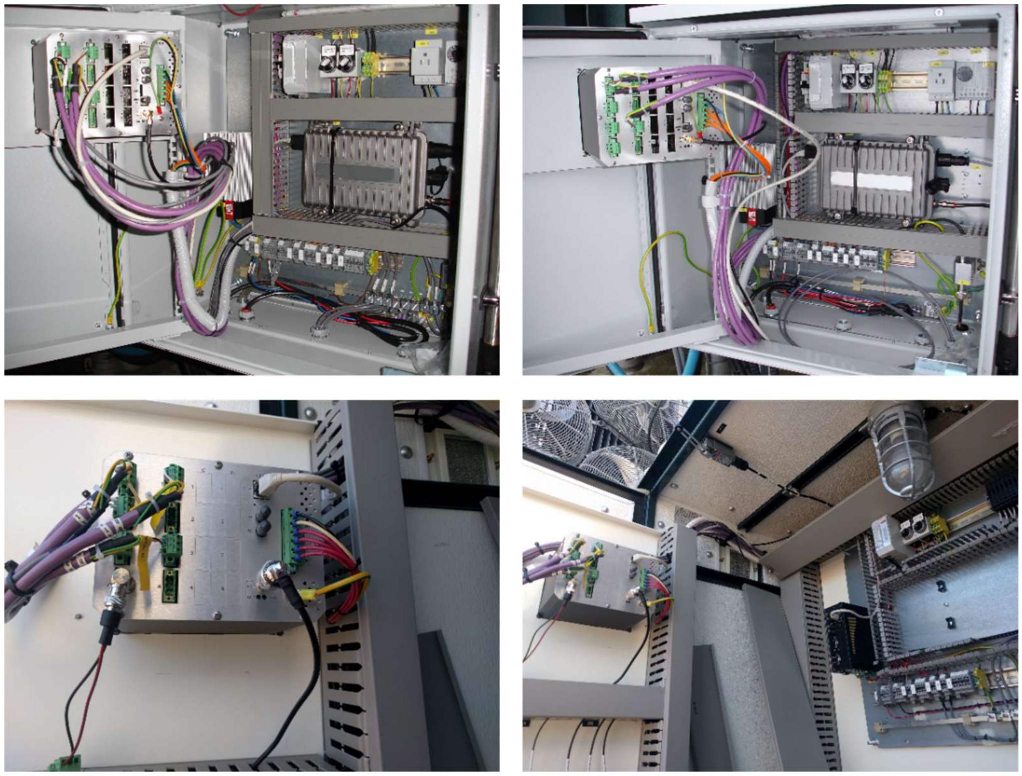

Figure III.2 The TMU and other related equipment.

This research studies the vibro-acoustic signal envelopes, specifically the switching operation portion of the signal of three OLTCs corresponding to three sister units which have been monitored continuously from 2016 to 2021. The transformers under study are referred to as T3A, T3B, and T3C hereafter in this paper. It should be noted that the in-tank brand and model of these OLTCs is ABB UC. According to the mechanical design of their main switching contacts (odd and even position) [75], it is possible to divide each dataset into these two categories, odd and even positions. This brings us to analyze six datasets that are named T3A-odd, T3A-even, T3B-odd, T3B-even, T3C-odd, and T3C-even.

3.2.2. Preprocessing

The raw measured vibro-acoustic signals are complex, not aligned, and, therefore, not suitable for extracting useful information and enabling trending. In this work, two preprocessing techniques are applied on vibro-acoustic signals. The first preprocessing is signal envelope extraction. The original vibro-acoustic signals are complex and non-linear and should be simplified to provide better analysis possibilities. One of the most common approaches that is used to simplify signals is signal envelope extraction. This approach generates a smooth signal based on the original signal. There are several filters and methods, such as Hilbert transform, LPF, moving average, wavelet transform, Savitzky–Golay filter, and HHT, that are used to extract a signal envelope [22, 38, 42, 45, 48]. In this research, Hilbert transform and LPF are used to extract the signal envelope. It should be noted that this preprocessing computing is carried out in the TMU and just the signal envelope is saved. The second preprocessing is a signal envelope alignment. Temperature and other parameters affect the vibro-acoustic signal envelopes and create a time lag between them. Therefore, vibro-acoustic signal envelopes should be aligned to simplify comparison. One of the techniques is a first-order time-realignment technique which is used in this paper [43, 74]. In addition, a moving average of ten consecutive envelopes is used to reduce the natural variations between vibro-acoustic signal envelopes. Moreover, a reference is established for each OLTC dataset individually and is achieved by computing the average of twenty envelopes starting from the commissioning of the TMU. For best results, this reference should be taken when the OLTC is in good condition, when it is new or after a maintenance or an inspection confirming its good state. Comparing measured envelopes over time with a reference helps to detect changes over time.

Figure III.3 shows the reference related to dataset T3A-odd and all the envelopes of the dataset (shown in grey). It should be noted that the envelopes are processed using the alignment technique. In addition, combined logarithmic and linear scales are also applied on vibro-acoustic signal envelopes.

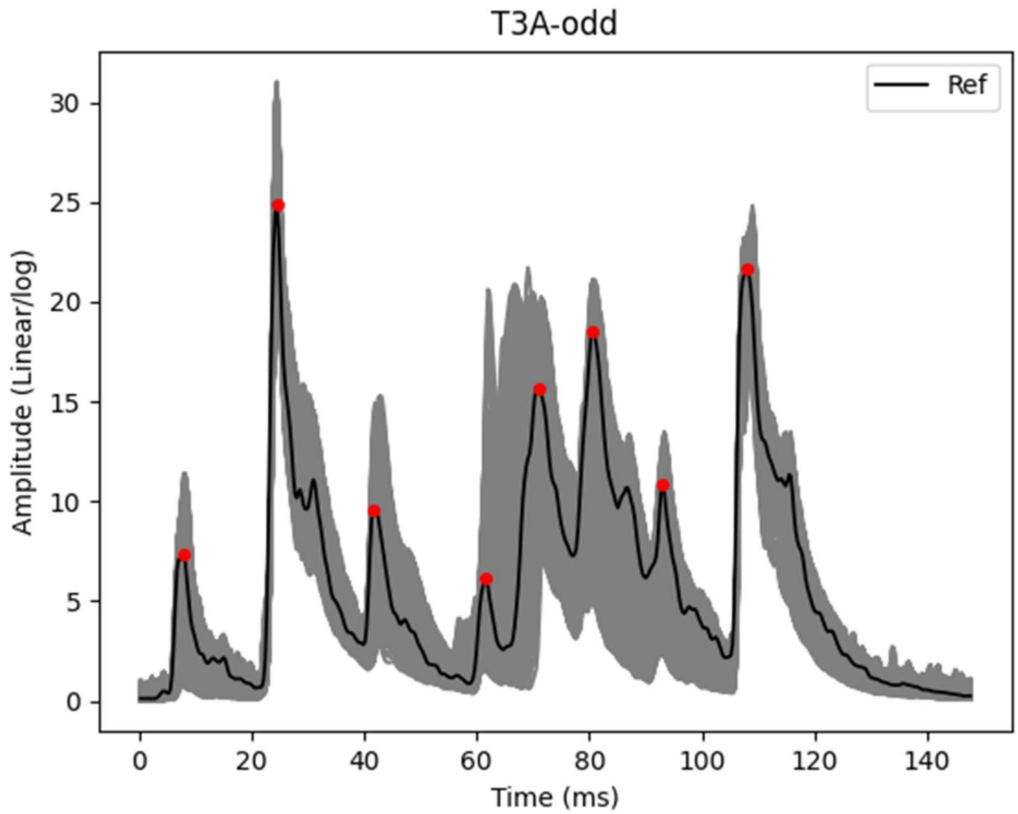

Figure III.3 The reference and all averaged and aligned envelopes (in grey) related to dataset T3A-odd. The eight main peaks of the reference are highlighted with red circles.

3.3. Extracting main peaks

As mentioned, there is a reference for each dataset. In the first step, the main peaks of the reference are extracted. It should be noted that there are many peaks in the reference, and the peaks with the maximum local amplitude over a zone are highlighted as the main peaks. In Figure III.3, the eight main peaks of the reference are highlighted using red circles. According to the time index of each reference main peak, the main peaks in all envelopes (with respect to the time) are extracted based on some window functions and comparison algorithms. Figure III.4 shows the steps to identify the main peaks. These steps are carried out for each major peak identified in the reference (see Figure III.3), individually. In this regard, dynamic windows are applied two times using different functions. It should be noted that functions (Function (1) and Function (2)) are applied parallel in order to find main peaks based on dynamic window. A comparison algorithm is then applied to select the best position of the peaks obtained from the dynamic window functions. Then, the main peaks are extracted based on a static window function in order to extract better results. The size of the static window is adapted based on the main peak location extracted from the dynamic window and comparison algorithm. In the flowchart depicted in Figure III.4, it can be clearly observed that the final peak detection block branches from both static and dynamic blocks. In fact, a comparison algorithm is applied to the results from the static and dynamic windows to extract the final localization of the main peaks. In the following, the dynamic and static window functions and comparison algorithm are explained in detail.

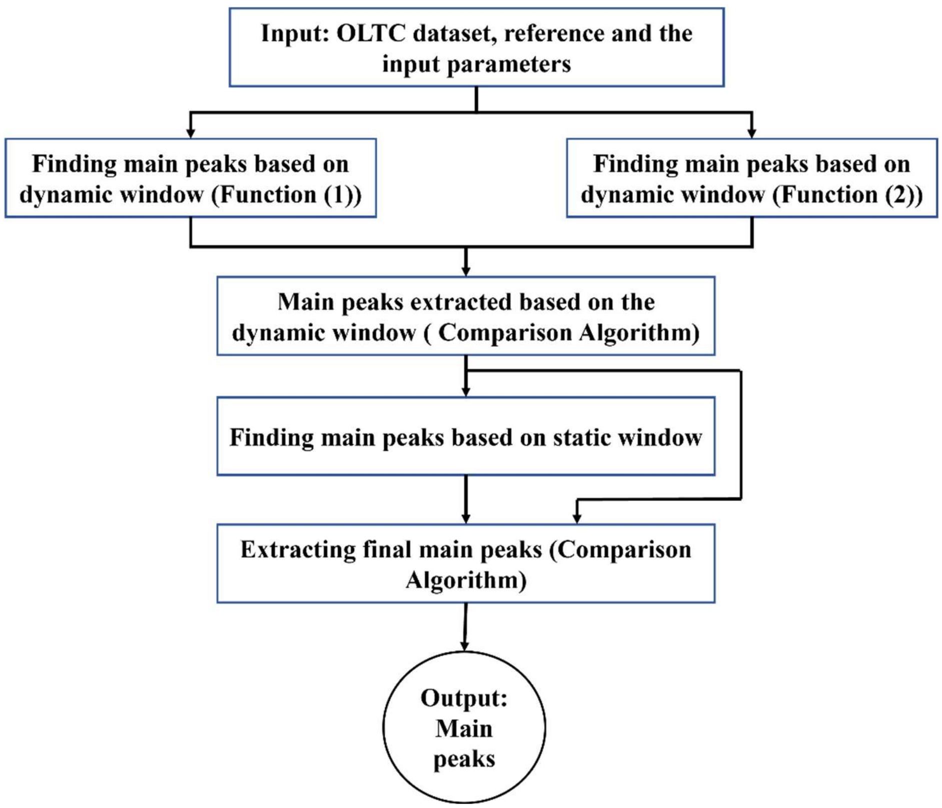

Figure III.4 The steps to identify the main peaks of vibro-acoustic signal envelopes.

3.3.1. Dynamic window

The dynamic windows slide over the zones of the main peaks with a size less than 20 samples. This small sample size minimizes the chance of wrong main peak positioning, especially in areas where there are multiple main peaks located close to each other (see, for instance, main peaks 4, 5, 6, and 7 in Figure III.3). The windows' moving ability enables the capability to track the time displacement of the main peaks (see, for instance, the main peak 5 in Figure III.3). These windows are used individually for each main peak identified in the reference.

The middle of the dynamic windows is located at the index of the reference main peaks. Then, all existing peaks within the windows are found and one of these peaks is considered as the main peak. It should not go without saying that this procedure is faced with two challenges, including the absence of peaks in the window area and the identification of one peak as the main peak among several peaks. In the following, each of these issues and the provided solutions are explained in detail.

- **Absence of Peaks in the Dynamic Window:** As mentioned, a dynamic window has a sample size smaller than 20 samples and it is normal that there are no peaks within the window. Increasing the size of the dynamic window would be more likely to lead to identifying the wrong location for the main peak. Therefore, we use a last in, first out (LIFO) stack [76] to store the index of found main peaks. When the main peak in a window is found, the position of this peak is stored in this stack (push operation). This step is carried out for the next envelopes with respect to time. In the procedure of finding peaks in envelopes, if there are no peaks within a window, the index of the corresponding reference peak is changed with the index stored in the stack. As such, the last index position entered in the LIFO stack is extracted and used as the reference index (pop operation). If there is still no peak in the window, the reference index of the last location in the LIFO stack is used. This process continues until one peak is found or the stack is empty. Figure III.5 represents this procedure. As depicted in this figure, the main peak was identified in four envelopes and their peak indexes were saved (push operation) in the LIFO stack. In this stack, Ref 4, Ref 3, Ref 2, and Ref 1 are, respectively, the last, third, second, and first index of the main peak that were found. Now, the main peak from the fifth envelope should be found. In this envelope, there is no peak in the window. Therefore, the latest index stored in the stack (Ref 4) (pop operation) replaces the reference index. If the peak is not found in the window again, the reference is changed with Ref 3. This step continues until a peak is found, or the stack is empty. If the stack is empty and no peak is found, it is considered that there is no peak in this area of the fifth envelope.

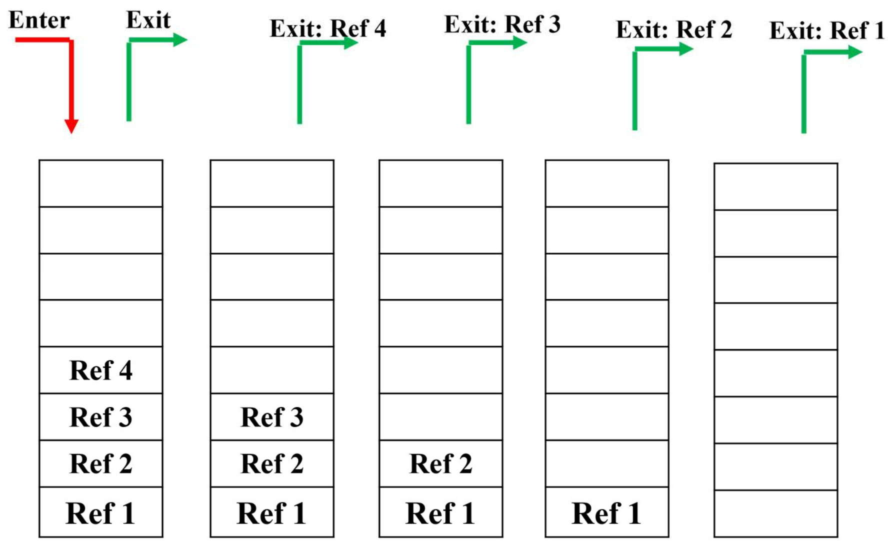

Figure III.5 LIFO stack.

- **Selecting the Best Position for the Main Peak among Several Peaks:** Generally, if there is more than one peak within the window, the peak that has a higher amplitude is considered the main peak. It should be noted that this assumption is not always true due to noise and natural variations between acoustic signatures of a tap-changer in good condition. As such, if there is more than one peak within the window, the two peaks (also referred to as separated peaks) that have the first and second highest amplitudes are identified and, later, one of them is selected as the main peak. Two functions, EF1 and EF2, are used to select the best position of the main peak between the two identified peaks. These functions represented in Equations (III.1) and (III.2) are computed between each identified peak and the reference peak.

$$EF1 = ED + MSE \tag{III.1}$$

$$EF2 = 1/ED + AP \tag{III.2}$$

$$ED\ (X_1, X_2\ ) = \sqrt{(x_1 - x_2)^2 + (y_1 - y_2)^2} \tag{III.3}$$

$$MSE = \frac{1}{n}\sum_{i=1}^{n}(env1(i) - env2(i))^2 \tag{III.4}$$

where ED is the Euclidean distance between the maximum value of the reference and identified peaks and MSE represents the mean square error between the peaks [23]. AP in (III.2) represents the amplitude value of the peak. It should be noted that MSE is computed for the area (10 samples) around the maximum value of the identified and reference peaks. env1 and env2 are two vectors that contain the samples from the regions surrounding the two identified peaks. n is the number of samples in env1 and env2, which is equal to 10 for the purpose of this study. These two evaluation functions (EF1 and EF2) are calculated for each of the two identified peaks, individually.

Following the EF1 function, a peak that has a lower EF1 value (smaller ED and MSE from the reference) is selected as the main peak. Based on the EF2 function, a peak that has a higher EF2 value is selected as the main peak.

If there is a difference between the results obtained using the EF1 and EF2 functions, the comparison algorithm explained in Section 3.3.3 is used to select the best index for the main peak.

It should be noted that the pseudocode for the dynamic window is presented in Appendix A (Section 8.1.).

3.3.2. Static window

Because the dynamic window has a small sample size (less than 20 samples), it is likely that the main peak is located out of this window and that the wrong place is selected for the main peak. In addition, the risk of selecting the wrong position based on dynamic windows, is also possible. For instance, the peaks that are close to the main peak are likely to be mistaken as a main peak. A static window is introduced to solve these issues. For each main peak, a static window with a fixed time range (zone) is defined and the main peak is constrained to be located in the static window. For example, in Figure III.3, and for the main peak 1, the size and location of the corresponding static window should consist of a time range around main peak 1 that the position of the peak in each envelope is placed in this range. As such, this window has a specific size for each main peak and its size is selected automatically for each main peak. The static window size (SWS) is computed for each main peak individually after applying the dynamic window functions for each main peak. SWS for each main peak can be computed according to (III.5).

$$SWS = HTP - LTP + 2 \tag{III.5}$$

where HTP and LTP are the highest and lowest time positions of main peaks that are found in all envelopes after applying dynamic windows and the comparison algorithm, respectively. The start and end point of the static window is located at (LTP − 1) and (HTP + 1), respectively, and a peak that has the highest value in the static window is selected as the main peak. It should be noted that this window can be used if there is no overlapping with the neighbor's main peak. In the considered datasets of this study, no overlapping is observed between the main peaks that are adjacent to each other.

It should be noted that the pseudocode for the static window is presented in Appendix A (Section 8.2.).

3.3.3. Comparison algorithm

This algorithm is used to select the best position for the main peak if there is a difference between the peak positions identified using the dynamic and static windows. To summarize, the main peaks are first identified using dynamic windows and functions EF1 and EF2. If there is a difference between the results obtained from these two functions, the comparison algorithm is used to select the best position. Subsequently, the main peaks are extracted using the static window. The comparison algorithm is applied a second time if there is a difference between the results obtained from dynamic and static windows (Figure III.4). The steps of this algorithm are explained in Figure III.6. It should be noted that the pseudocode for the comparison algorithm is presented in Appendix A (Section 8.3.).

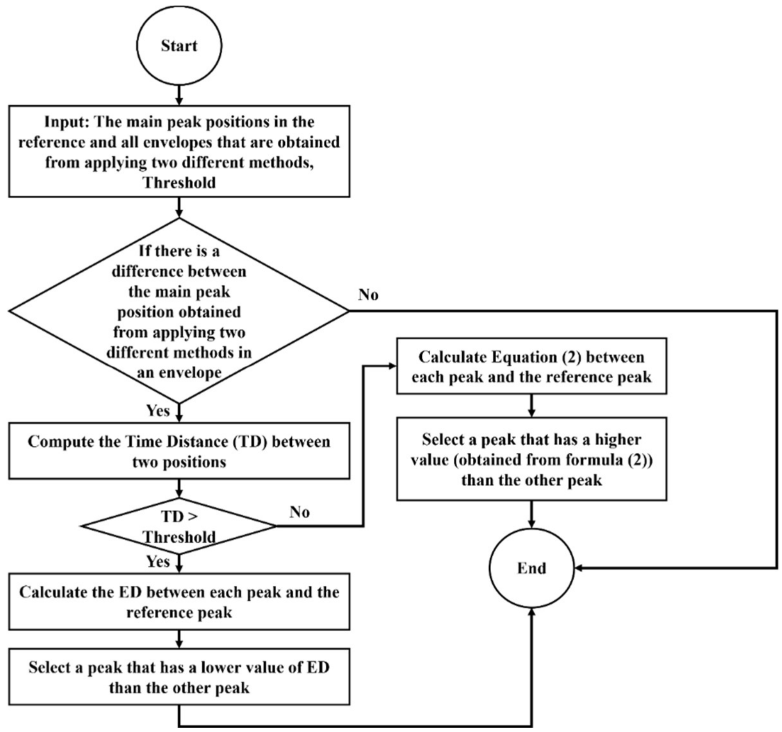

Figure III.6 The steps of comparison algorithm.

3.4. Computing ED

ED is a metric distance that is used to measure the amount of similarity between two points or two shapes. This metric is sensitive to shifting and, therefore, it is a good metric to track changes in vibro-acoustic signal envelopes. In this study, ED values are computed using data from each envelope in comparison with the reference signal envelope. It should be noted that ED is not computed for the whole signal. Two approaches are used. The first set of EDs is calculated using Equation (III.6) and it uses the main peaks localization (sample number and amplitude). The second set of EDs uses amplitude vectors in the area (zone) of the main peaks. This metric is calculated using Equation (III.6). The same number of EDs is calculated for both approaches.

$$\mathrm{ED2}\,(\mathrm{T},\mathrm{S}) = \sqrt{\sum_{i=1}^{n} (\mathrm{T_i} - \mathrm{S_i})^2} \qquad \text{(III.6)}$$

where T and S are vectors of length n (n is the number of samples in the zone). In the developed fault detection approach, the average value of each computed ED (for the amplitude of the main peak/zones) is calculated per year. Finally, the linear regression technique and R^2 are used to identify the parts of envelopes where significant changes have taken place over time.

3.5. Results

In this section, the performance of the proposed algorithms is analyzed based on the implementation in Python 3.9.5 (PyCharm was used as the IDE). The peaks in the signal envelopes are extracted using the "find_peaks" function of the SciPy signal processing package.

In addition, six individual datasets are used to analyze the proposed methodology. It should be noted that, in the preprocessing stage of the signal envelope alignment, the envelopes are aligned and limited to 500 samples in each dataset. Figure III.7 shows all envelopes in each of these datasets that have been measured from 1 September 2016 to 1 September 2021, individually in grey. In addition, in this figure, the reference of each dataset and the amplitude of main peaks of reference are displayed with a solid black line and red circles, respectively.

As mentioned, the first objective is to extract the main peaks from each envelope in each dataset. After that, in each dataset, the ED between the amplitude of each main peak in the reference and each envelope is calculated. In addition, it is possible to subdivide each dataset into the main zones based on the location of main peaks. The sizing and localization of each zone is achieved using the static window strategy presented in Section 3.3.2. After that, the ED is calculated between each zone in the reference and envelopes. In the following, the results related to the main peaks, zones, and ED are shown. It should be noted that the results of one dataset are described in this work to avoid repetition. Among the six datasets, the T3A-odd dataset was selected in this work because significant changes have been seen.

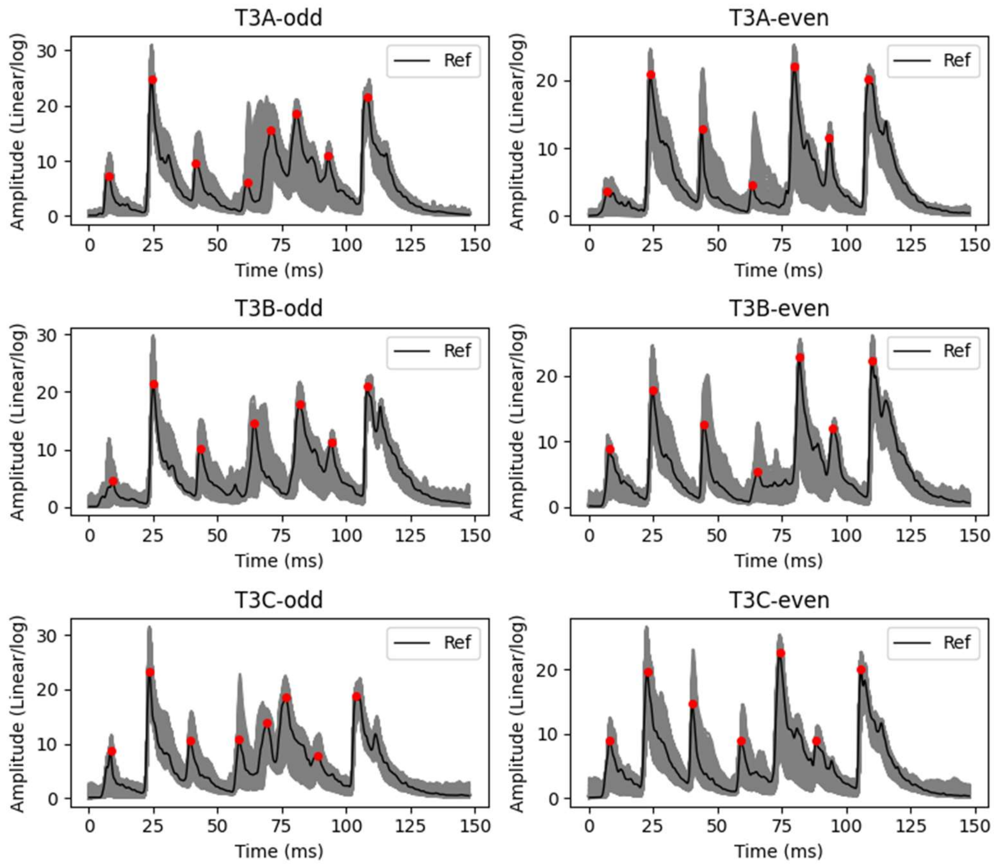

Figure III.7 All envelopes in the datasets T3A-odd, T3B-odd, T3C-odd, T3A-even, T3B-even, and T3C-even are shown in grey. In addition, the references and their main peaks are displayed with solid black line and red circles, respectively.

3.5.1. Extracting main peaks from envelopes

In this section, the main peaks are extracted (see Figure III.4). To visualize the extraction of main peaks, the results of one envelope for main peak 5 and another for main peak 6 are shown in Figure III.8 (a), (b), respectively. In these figures, the reference and its main peak are shown using a solid blue line and green circle, respectively. In addition, the solid black curve represents input envelop. As shown in Figure III.4, we use two parallel functions (Function (1) and Function (2)) to find the main peak based on the dynamic window; the main peak positions extracted using these functions are shown by red and blue circles on the envelope (black curve), respectively. Due to finding different positions for main peak 5 in the first instance envelope shown in Figure III.8 (a), the comparison algorithm is applied and the peak position, which is highlighted in blue, is selected as the best position for the main peak. After that, the main peaks based on static window are also extracted, and the blue circle is considered a result of this process. Therefore, due to obtaining similar results in the processes of main peak extraction based on dynamic and static windows, the comparison algorithm is not reapplied for a second time. In another instance, regarding the envelope shown in Figure III.8 (b), the results of two parallel functions based on the dynamic window are the same for main peak 6 that those shown by the blue circle in the envelope. Therefore, the comparison algorithm to compare the results extracted by two dynamic windows is not applied. While a different position, shown by red circle, is extracted from the static window, the comparison algorithm should be applied to select the best result between the dynamic and static windows. After comparison, the blue circle is selected as the best position. It should be noted that the threshold (input parameter) in the comparison algorithm is set to 6.

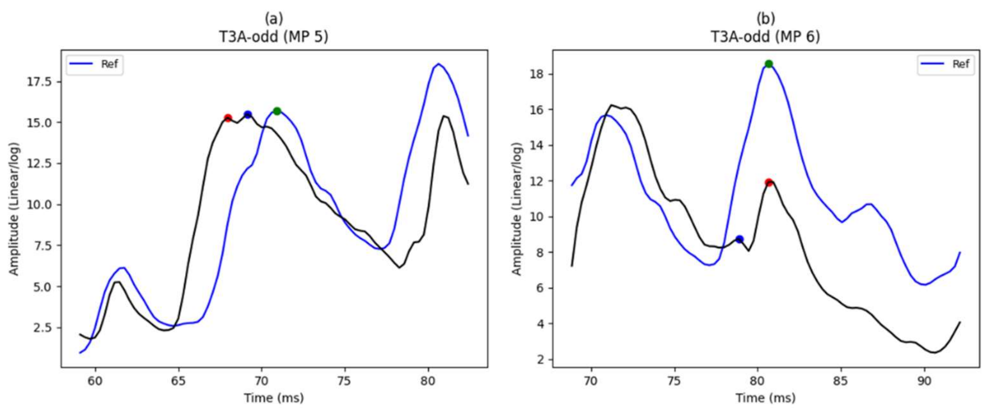

Figure III.8 The results of two instance envelopes in the T3A-odd dataset: (a) main peak locations extracted using dynamic windows; (b) main peak locations extracted using dynamic windows and static window. A solid blue line represents the reference and its main peak and green dots, while the main peak positions extracted using dynamic windows are represented by red and blue dots on the envelope (black curve).

The results of the main peaks in each envelope are shown in Figure III.9 (a). It is also possible to subdivide each dataset into several main zones. The size and location of each zone are determined based on the location of the amplitude of the main peaks shown in Figure III.9 (a). It should be noted that the size of each zone can be computed using Equation (III.5). Figure III.9 (b) displays the main zones which are highlighted in blue. The location of each zone is also provided in Table III.1.

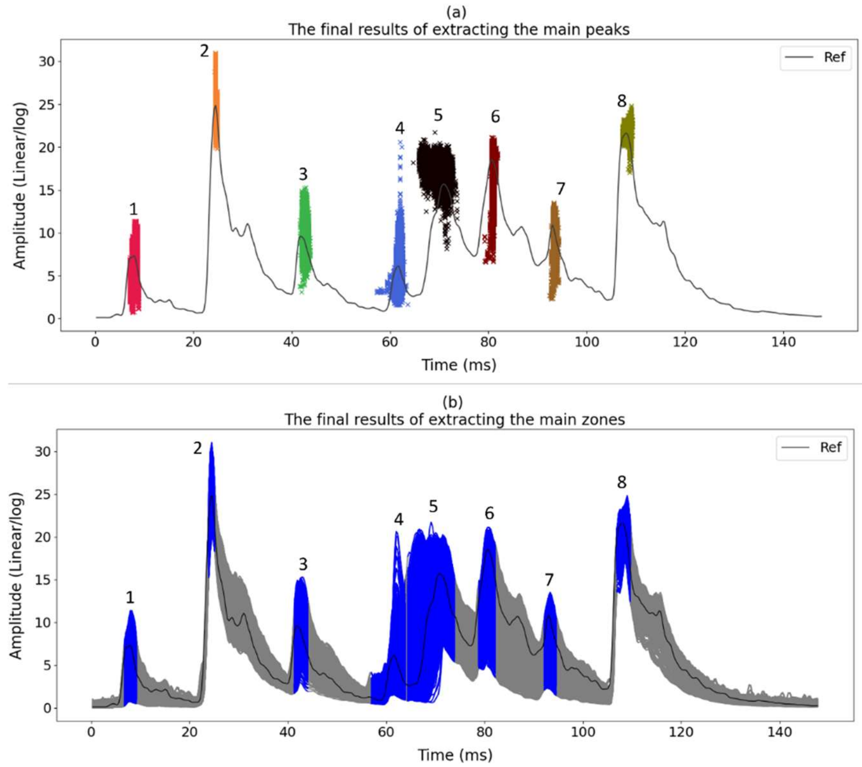

Figure III.9 (a) Main peaks extracted in dataset T3A-odd. Note that the size and location of each zone highlighted in different colors are determined based on the location of the amplitude of the main peaks; (b) The related zones are highlighted in blue.

Table III.1 Location of each main zone in dataset T3A-odd.

Zone Number	Location of Zone
1	From 6.5 ms to 9.2 ms
2	From 23.6 ms to 25.1 ms
3	From 41.1 ms to 44.0 ms
4	From 56.7 ms to 63.8 ms
5	From 64.1 ms to 73.9 ms
6	From 78.6 ms to 82.1 ms
7	From 91.9 ms to 94.5 ms
8	From 106.7 ms to 109.6 ms

3.5.2. Computing ED to track changes in signal envelopes over time

In this section, ED is calculated between the reference signal and each envelope. This step is repeated twice. The ED is first calculated using the localization of main peaks. Secondly, EDs are computed using the samples for each zone as vectors in Equation (III.6). The average ED per year is computed to detect if there is a changing or evolving trend in the data.

The ED results related to the amplitude of the main peaks and their zone are available in Figure III.10 and Figure III.11, respectively. In these figures, ED and the average ED per year are shown in individual subfigures. These figures show clearly the seasonal pattern and an increasing trend for one of the main peaks.

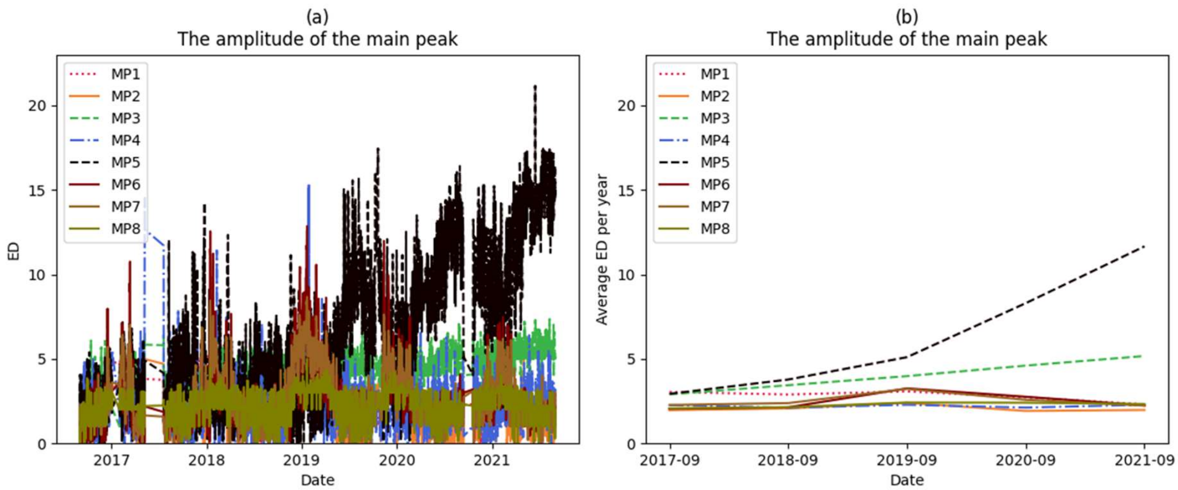

Figure III.10 ED computed on the main peaks with respect to time (in dataset T3A-odd).

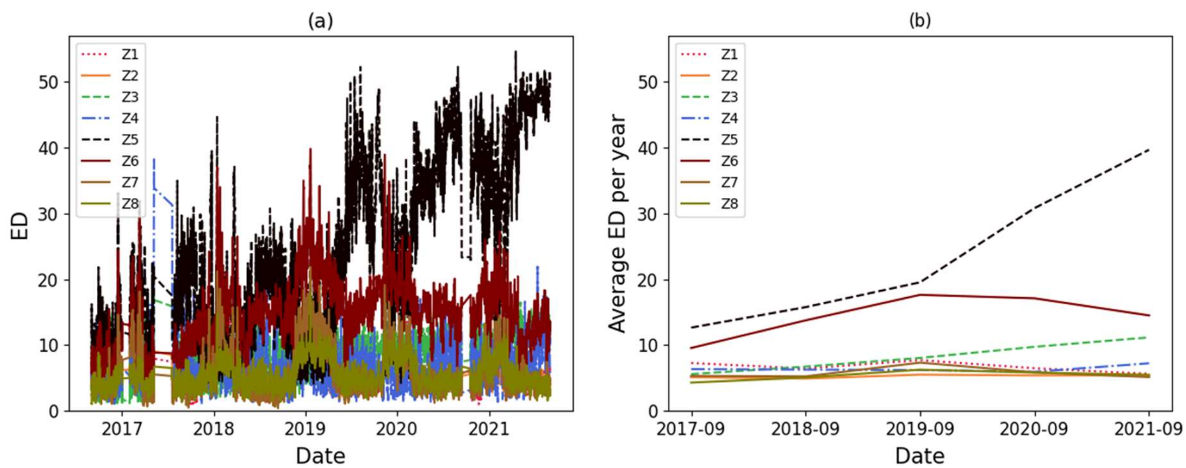

Figure III.11. ED computed on the zone of the main peaks with respect to time (in dataset T3A-odd).

3.6. Discussion

As mentioned, a significant increasing trend is seen in dataset T3A-odd. This trend is not visible in all the other datasets of the sister units located in the same substation, as shown in Figure III.12 and Figure III.13

for the T3C-odd dataset. Moreover, Figure III.14 shows the ED values computed between the 500 samples of each envelope compared to the reference. As shown in this figure, dataset T3A-odd has a different pattern compared to the other datasets [75]. It should be noted that the already implemented algorithm in the experimental setup is based on the measured global ED (see Figure III.14) and there is an alarm threshold based on the normal distribution of the recorded data. The developed algorithm in this paper, which is an effort to improve the current practice, utilizes other criteria to detect the fault, which is different than the already implemented algorithm. The proposed method aims to detect and locate the changes in the OLTC's switching vibro-acoustic signal envelopes. This is a more in-depth analysis that supports the global trending made on the whole switching signature (Figure III.14). According to this goal, the main peaks and zones containing the main peaks are extracted to detect the location of changes in vibro-acoustic signal envelopes. Figure III.9 (a), (b) represent the locations of the main peak and zones in the T3A-odd dataset, respectively. The provided results indicate that the developed algorithms succeed in extracting features from vibro-acoustic signal envelopes despite the close proximity of the main peaks 4, 5, 6, and 7, and the observed displacement of main peak 5. After that, the ED metric is used to track changes in the main peaks and zones. The results of ED values related to the main peak and zones are presented in Figure III.10 and Figure III.11, respectively. As illustrated in these figures, part 5 (MP5 and Z5) has a pattern that differs from the other parts. It can be concluded that the source of the global changes in the T3A-odd dataset (as shown in Figure III.14) is due to this specific part of the envelope.

A linear regression technique is used to determine if there is an increasing or decreasing trend in the ED's computed values. This technique is applied to the average ED per year, and if the absolute coefficient of linear regression is greater than 0.5 and R^2 is higher than 0.8, it indicates that there is a significant change over time. The coefficient value of linear regression related to the average ED per year for the main peaks and their zone are represented in Table III.2 In this table, the main peaks and zones 3 and 5 are in bold because the thresholds (coefficient and R^2) are exceeded, indicating that significant changes have been detected in these parts of the vibro-acoustic signal envelopes. Although the changes in main peak and zone 5 were clear upon a visual inspection of Figure III.10 and Figure III.11, the main peak and zone 3 also had a smooth change over time which was detected using a statistical test.

In future works, anomaly detection techniques supported by artificial intelligence will be explored to detect changes in the vibro-acoustic signal envelopes. In addition, researchers will aim towards a more in-depth understanding of the physical sources that create the main peaks, in order to achieve diagnostics after an anomaly is detected and improve the condition-based maintenance.

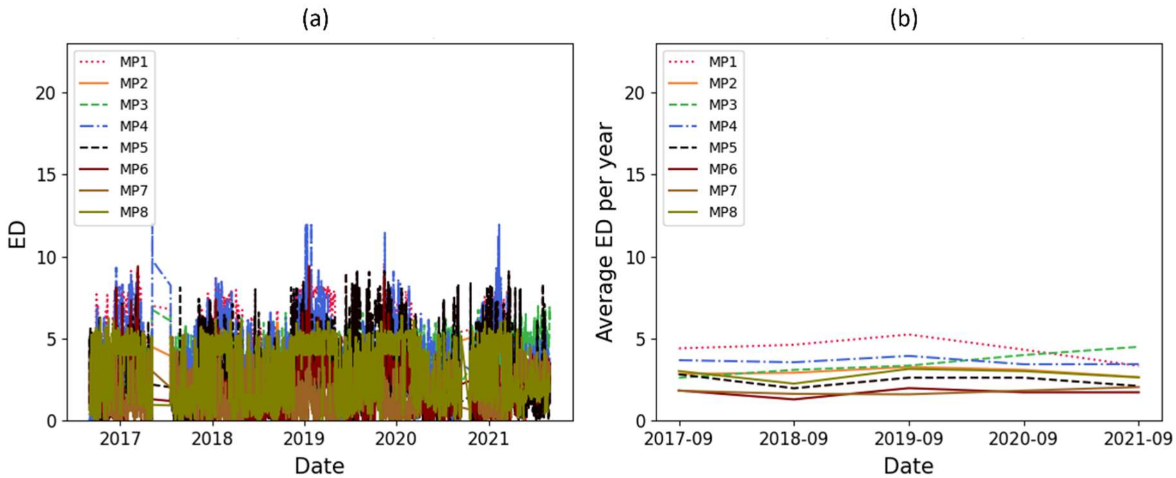

Figure III.12 ED computed on the main peaks with respect to time (in dataset T3C-odd).

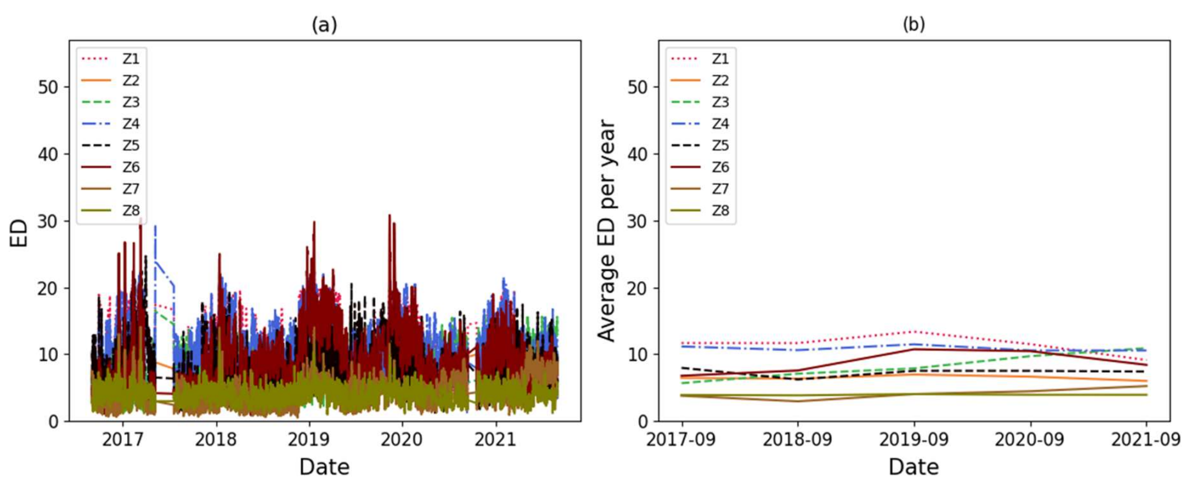

Figure III.13 ED computed on the zone of the main peaks with respect to time (in dataset T3C-odd).

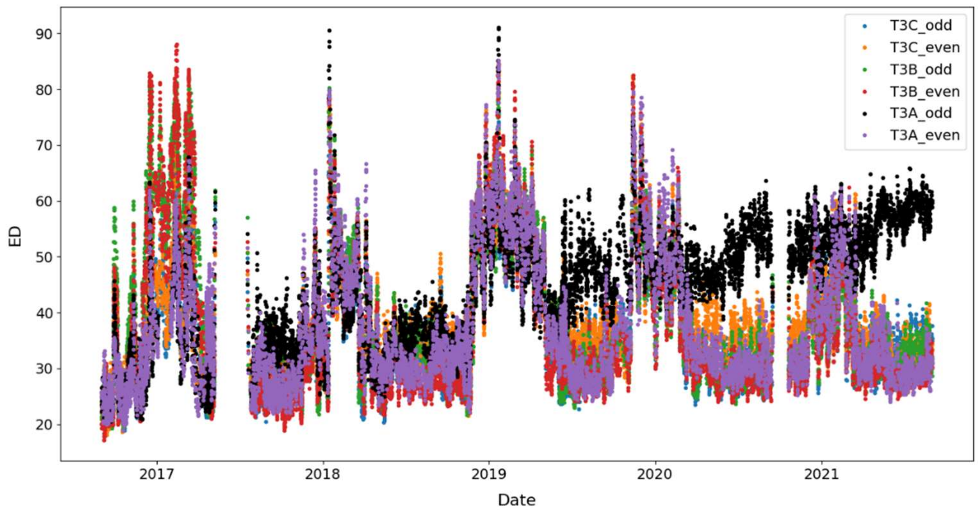

Figure III.14 ED computed on the whole envelope for all studied datasets.

Table III.2 Linear regression coefficients related to the average ED per year computed for main peaks and zones in dataset T3A-odd. The absolute coefficient of linear regression that is greater than 0.5 and R^2 is higher than 0.8 are in bold.

Main Peak and Zone Number	Coefficient (Main Peak)	Coefficient (Zone)
1	−0.16420971	−0.32365302
2	−0.01289195	0.10738021
3	**0.56964947**	**1.41485584**
4	0.00550331	0.14465934
5	**2.19588839**	**6.90356619**
6	0.1016055	1.3236921
7	0.01265612	0.02436068
8	0.07725418	0.31156756

3.7. Conclusions

In this research work, a new methodology is developed to detect, locate, and track changes in envelopes of vibro-acoustic signals related to power transformers OLTCs. The developed method accomplishes this through two major steps: main peak extractions and ED computations. As such, the main peaks are extracted from the envelopes to detect and locate the changes in the envelopes. According to the locations of these main peaks, the main zones are also extracted from envelopes. Afterwards, the ED metric is utilized to compute the amount of similarity between the over-time monitored envelopes with the reference. In this regard, ED is computed on the main peaks location and on their corresponding zone. According to the ED values, significant changes were observed in one main peak and its zone. The linear regression technique was applied on the average ED per year to enable an automated detection. The results show that this methodology is not only able to detect changes in vibro-acoustic signal envelopes, but it also provides a more in-depth analysis of the location of these changes in the vibro-acoustic signal envelopes, and the rate of change over time. The developed algorithms were applied to six different real-life datasets obtained from experimental measurements and the main peaks and zones were extracted successfully. The provided results indicate that the developed algorithms succeed in extracting features from vibro-acoustic signal envelopes. Moreover, the success in feature extraction of different datasets indicates the developed algorithms' reliability to be applied to every dataset of similar OLTC types.

Chapitre IV
Utilisation de l'apprentissage profond pour détecter des anomalies dans les Changeurs de Prises en Charge basés sur les caractéristiques des signaux vibro-acoustiques

Article publié dans Energies, mars 2024

doi : 10.3390/en17071665

Utilisation de l'apprentissage profond pour détecter des anomalies dans les Changeurs de Prises en Charge basés sur les caractéristiques des signaux vibro-acoustiques

Résumé

Le CPC qui régule la tension du transformateur est l'un des composants les plus importants et stratégiques d'un transformateur. Détecter les défauts de ce composant à un stade précoce est donc crucial pour prévenir les pannes de transformateur. Ces dernières années, Hydro-Québec a initié un projet visant à surveiller l'état des CPC dans les transformateurs de puissance en utilisant des signaux vibro-acoustiques. Un système d'acquisition de données a été installé sur des CPC réels, mesurant en continu les enveloppes des signaux de vibration générés au cours des dernières années. Dans ce travail, un autoencodeur profond multivarié, une méthode basée sur la reconstruction pour la détection non supervisée des anomalies, est employé pour analyser les enveloppes des signaux de vibration générés par les CPC et détecter les comportements anormaux. Le modèle est entraîné à l'aide d'un ensemble de données obtenu à partir des conditions de fonctionnement normales du transformateur pour apprendre les modèles. Par la suite, une estimation de densité par noyau (KDE), une méthode non paramétrique, est utilisée pour ajuster les erreurs de reconstruction (par rapport aux données normales) obtenues à partir du modèle entraîné et pour calculer les scores d'anomalie, ainsi que le seuil statique. Enfin, les anomalies sont détectées à l'aide d'un autoencodeur profond, de la Estimation Par Noyau (KDE) et d'un seuil dynamique. Il convient de noter que les variables d'entrée responsables des anomalies sont également identifiées en fonction de la valeur de l'erreur de reconstruction et de l'écart type. La méthode proposée est appliquée à six ensembles de données réels différents pour détecter les anomalies en utilisant deux approches distinctes : individuellement sur chaque ensemble de données et en comparant les six ensembles de données. Les résultats indiquent que la méthode proposée peut détecter les anomalies à un stade précoce. De plus, trois alarmes, incluant les anomalies ignorables, les changements à long terme et les altérations significatives, ont été introduites pour quantifier l'état des CPC.

Using Deep Learning to Detect Anomalies in On-Load Tap Changer Based on Vibro-Acoustic Signal Features

Abstract

OLTC that regulates transformer voltage is one of the most important and strategic components of a transformer. Detecting faults in this component at early stages is, therefore, crucial to prevent transformer outages. In recent years, Hydro-Québec initiated a project to monitor the OLTC's condition in power transformers using vibro-acoustic signals. A data acquisition system has been installed on real OLTCs, which has been continuously measuring their generated vibration signal envelopes over the past few years. In this work, the multivariate deep autoencoder, a reconstruction-based method for unsupervised anomaly detection, is employed to analyze the vibration signal envelopes generated by the OLTC and detect abnormal behaviors. The model is trained using a dataset obtained from the normal operating conditions of the transformer to learn patterns. Subsequently, kernel density estimation (KDE), a nonparametric method, is used to fit the reconstruction errors (regarding normal data) obtained from the trained model and to calculate the anomaly scores, along with the static threshold. Finally, anomalies are detected using a deep autoencoder, KDE, and a dynamic threshold. It should be noted that the input variables responsible for anomalies are also identified based on the value of the reconstruction error and standard deviation. The proposed method is applied to six different real datasets to detect anomalies using two distinct approaches: individually on each dataset and by comparing all six datasets. The results indicate that the proposed method can detect anomalies at an early stage. Also, three alarms, including ignorable anomalies, long-term changes, and significant alterations, were introduced to quantify the OLTC's condition.

4.1 Introduction

Power transformers perform an important role in balancing the voltage levels in the power system. It is therefore very important to check their reliability to prevent the power system from being interrupted [71, 77]. Among the power transformer components, OLTC, which is used to regulate the transformer's output voltage, is identified as one of the most vulnerable parts. Its failure is among the main cause of major power transformers' catastrophic failures [13, 63, 78, 79]. In this regard, it is necessary to detect OLTC faults in their incipient stages. There are several methods that allow for the detection of OLTC faults. These methods are classified into three categories: (1) offline, (2) on-line, and (3) real-time classes. The offline measurements are performed when the device is de-energized or is out of service. Even though these methods have high accuracy, they need manpower and may be costly due to the required shutdown of the equipment. The online measurements are performed on an energized or in-service device. These methods allow for users to interact with data stored in databases. These data are later accessible from anywhere at any time. The measurements are obtained whenever required. In real-time methods, the measurements also must be continuously acquired from an energized or in-service device [9, 11, 80]. In addition, real-time systems must respond to events quickly and accurately.

In this work, the vibro-acoustic signals analysis approach, which is an online and real-time method, is used to monitor the OLTC [15]. This technique can detect OLTC faults based on vibro-acoustic signals. These vibro-acoustic signals are generated when the OLTC's moving parts move. Importantly, each OLTC tap position generates a vibro-acoustic signal that can assume similar characteristics to a fingerprint. This means that two vibro-acoustic signals are similar when measured from the same tap position at two different times. Consequently, comparing the latest OLTC vibro-acoustic signals with previous vibration signals helps to detect OLTC faults.

A thorough literature review indicates the development of several approaches to detect an OLTC's fault based on vibro-acoustic signals. In several works, the OLTC condition is assessed based on the bursts existing in vibration signals. In this regard, features including the number of bursts, the time lag between them, and their amplitude are extracted to analyze the OLTC's behavior [23-25, 58]. Specifically Ref. [58] extracted the burst based on CWT technique. The CWT's vertical ridge plot serves as a straightforward, clear, and visually intuitive method for illustrating fuzzy time domain vibration signals. In addition, the physical sources of the bursts were identified via controlled experiments. In [22, 38], the status of each OLTC tap position is analyzed to compare its waveform with a reference; Spearman's Rank Correlation Coefficient was applied to select the reference waveform. In [73], the condition of the tap changer is evaluated in three steps. In the first step, each vibro-acoustic signal is divided into two parts: preparation, which involves the motor running and driving the mechanical structure, and in-position, which encompasses the operation of the tap-changer. After that, the wavelet packet transform is used to decompose each part into 16 sub-components. Finally, the tap changer is evaluated based on a computation of the energy entropy of each sub-component. In [59], effective band multi-resolution feature parameters are achieved using the wavelet packet coefficients. Then, GA-SVM method is used to classify the mechanical vibration information and identify the mechanical state of the OLTC. Therefore, this methodology succeeds in detecting OLTC faults, and can serve as a reference for the operation and maintenance of OLTCs.

In an effort to develop a real-time monitoring of power transformers' OLTC, a vibro-acoustic monitoring module was developed and installed on nine single-phase auto transformers in service on Hydro-Québec's electric network [81]. This system continuously measures vibration signals from the OLTCs and records the signal envelopes. Since the operating temperature affects the vibration signals, this module also measures them. This research aims to develop a global and automatic methodology allowing for a comparison of OLTCs' vibro-acoustic signals to detect anomalies or malfunctions.

In some previous contributions from the authors [43, 74], the temperature effects on vibration signals were addressed. The techniques of averaging and time realignment were applied to discriminate the natural variations in the acoustic signatures of a tap-changer in good condition. It was also shown that changes in vibration signals caused by OLTC faults can be subdivided into two parts, including long-term changes and sudden variation [33]. In the long-term changes, the measured signals related to many previous operations (for example, 600 previous operations) were used for the comparison. In the sudden variation, the measured signals related to a few previous operations (for example, 50 previous operations) were used for the comparison.

In this contribution, the features were extracted from vibration signal envelopes and analyzed afterwards to evaluate the OLTC's condition. Since the vibration signal envelopes were recorded over several years, each extracted feature from the envelopes (with respect time) falls in the category of time series data. Therefore, methods based on anomaly detection in the time series domain were applied to detect anomalies in the features extracted from vibration signal envelopes.

Recall that, in time series analysis, there are approaches to detect data which do not follow the expected pattern [82]. Two common technical methods that are used to detect anomalies are based on prediction error and reconstruction error [83, 84]. In the prediction-error-based algorithms, a model is trained using normal data. After that, the trained model predicts the next instances. The anomalies are extracted based on the prediction error [85]. In the reconstruction-error-based algorithms, normal data are used to train the model. After that, the reconstruction error level of the normal data is determined. Afterwards, anomalies can be detected based on reconstruction error [83]. An autoencoder, a type of neural network, is one of the algorithm-based reconstruction errors used to map the input data. This method tries to reach an output that is very close to the input. Therefore, the output dimension is similar to the input one [83]. Different types of deep autoencoder, such as the LSTM autoencoder, convolutional autoencoder, variational autoencoder, and LSTM variational autoencoder, can be found in the literature [86]. Compared to statistical models, an important reason for the use of the deep learning method in this contribution is the effectiveness and simplicity of deep-learning-based methods. Statistical methods lose effectiveness as the dimensionality of the data increases due to the increase in computational complexity.

In this contribution, a two-step methodology approach is used to detect anomalies in three sister transformer units: (1) online and offline, and (2) three parts including preprocessing, anomaly detection, and the identification of variables responsible for anomalies. In the offline part, the normal dataset is used to build an anomaly detection model and a static threshold is set while, in the online part, recent measurements are analyzed, and the anomalies are detected. The preprocessing part, which is used in both the online and offline parts, is applied to the input dataset to reduce data complexity. Additionally, in this part, the dataset is prepared to undergo both long-term changes and sudden variation. In the anomaly detection part, a model based on an autoencoder and kernel density estimation (KDE) are used to detect anomalies in continuously measured vibration signal envelopes. In this regard, in the offline section, the autoencoder (AE) is trained with a normal dataset and then the reconstruction error is calculated. Later, KDE is fitted to reconstruction errors to compute anomaly scores and a static threshold. In the online section, the recent measurements are evaluated for normality or abnormality. The identification of variables responsible for anomalies is used exclusively in the online section to determine the inputs that are the origin of the anomalies.

It should be noted that a few works have evaluated an OLTC's condition based on machine learning techniques and vibration signals [26, 27]. To the best of the author's knowledge, deep learning, which has been used to achieve state-of-the-art performance in a wide range of problems, mimicking the learning process of the human brain, is being used for the first time in OLTC monitoring based on vibro-acoustic signal analyses. Even though deep learning is computationally expensive and requires a large amount of data and computational resources to train, it is best-suited for use in this this study due to its ability to handle large and complex data.

4.2 Data collection, preprocessing, and feature extraction

An OLTC monitoring system designed at the Hydro Québec's research institute (IREQ) has been installed on nine single-phase autotransformers (rated at 370 MVA, 735/√3/230/√3 kV) in service on Hydro-Québec's electric network. Vibration signal envelopes are continuously measured and recorded via an accelerometer installed near the diverter switch. Additionally, in this monitoring system, the motor current and temperature are measured and recorded using current clamp and temperature sensors. A detailed description of this monitoring system can be found in [81].

It should be noted that the measured vibration signals are complex and contain a lot of redundant information. In this regard, the Hilbert transformer and Low Pass Filter are applied to extract the signal envelope. After that, the first-order time-realignment technique and moving average are used to discriminate the effect of temperature and to reduce the natural variations in the acoustic signatures of a tap-changer, respectively. These preprocessing techniques were reported by the authors in [43, 74].

The research approach is as follows. Three OLTCs associated with three sister transformer units, which are of the ABB UC brand and model, referred to as T3A, T3B, and T3C throughout this paper, are considered as case study units. Vibro-acoustic signal envelopes, with a focus on the segments of the signals, which represent the switching of the OLTC contacts (transformer taps), are derived from the three corresponding OLTCs. By classifying the switching contacts or transformer taps as odd and even, the datasets are divided accordingly, resulting in six subsets: T3A-odd, T3A-even, T3B-odd, T3B-even, T3C-odd, and T3C-even (illustrated in Figure IV.1) [81]. In Figure IV.1, the moving average of 10 consecutively measured vibration signal envelopes is depicted in grey, while the reference data for each dataset are represented in black. The utilization of a realignment algorithm to compensate for the temperature effects on these datasets is notable.

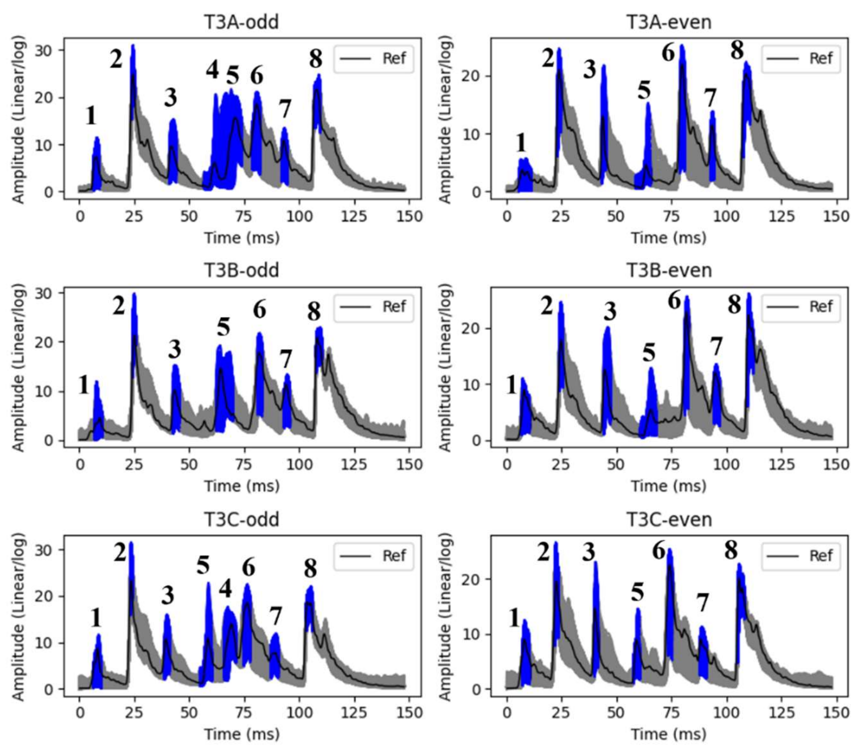

Figure IV.1 All envelopes in the T3A-odd, T3B-odd, T3C-odd, T3A-even, T3B-even, and T3C-even datasets are shown in grey. In addition, the references are displayed with solid black lines. The main zones in each dataset are highlighted in blue, and a number is assigned to each zone in each dataset.

To monitor the OLTC's condition, useful features should be extracted from the measured vibration signal envelopes. In this regard, the main zones are extracted automatically (see blue zones in Figure IV.1) based on the location of the main peaks. To detect the main peak location, at first, the location of the main peak in the reference is detected. After that, the main peaks in each vibration signal envelope are detected based on the reference main peak's location. Later, ED is computed between each zone in each envelope, realigned with time. The ED of the main zones in the T3A-odd dataset is shown in Figure IV.2. The details of the extraction of main zones are explained in the author's recent contribution [81].

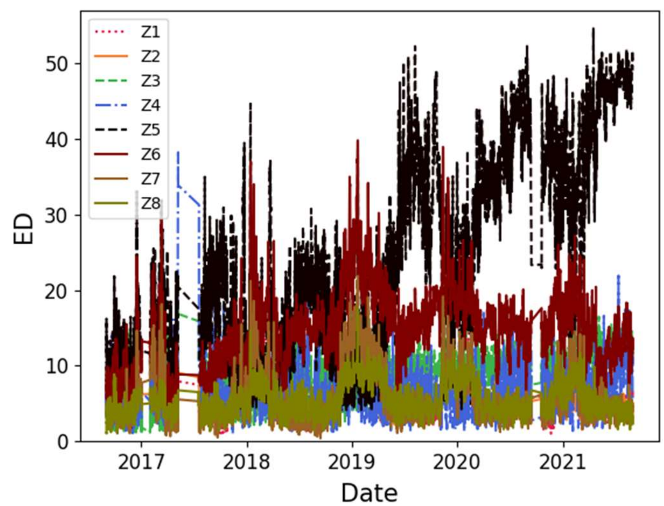

Figure IV.2 ED computed between each main zone located in each envelope, and the reference with respect to time regarding the T3A-odd dataset.

4.3 The Underlying concept

4.3.1 Time series decomposition

A time series can be split into different components. Generally, there are two types of decomposition, including additive and multiplicative. Based on these categories, a time series can be decomposed into three components: Trend (the overall trend in the time series), Seasonal (repeating patterns), and Residual (primarily considered to be noise). The decomposition function, based on addition and multiplication, is shown in Equations (IV.1) and (IV.2), respectively [87]. It is important to note that there is a delay in the real-time trend decomposition process, as this involves the utilization of past data at each time step (using non-symmetric filters) to calculate the trend [88].

$$X\ (t) = \text{Trend}\ (t) + \text{Seasonal}\ (t) + \text{Residual}\ (t) \qquad \text{(IV.1)}$$

$$X\ (t) = \text{Trend}\ (t)\ \times \text{Seasonal}\ (t) \times \text{Residual}\ (t) \qquad \text{(IV.2)}$$

4.3.2 Deep autoencoder-based anomaly detection

Another time series anomaly detection technique is based on reconstruction error. In this technique (Figure IV.3), a model is used to copy the input to the output. The model can therefore learn the pattern between the data. In the training step, the model improves itself to minimize the reconstruction error. After the training step, it is expected that the trained model will generate an output that is close to the input (lower reconstruction error) with the normal data and generate an output that is far from the input (higher reconstruction error) with the abnormal data. Consequently, anomalies can be detected using the reconstruction error. A popular technique that is used to reconstruct the input is through the use of autoencoders [86].

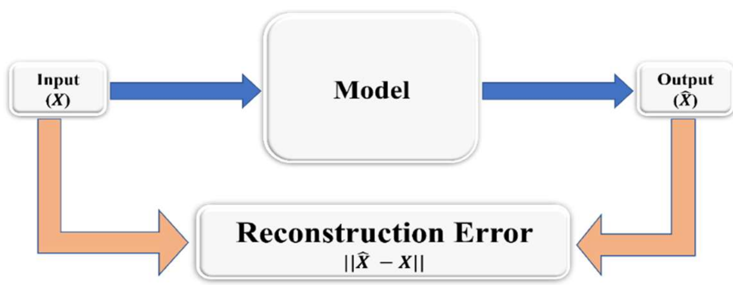

Figure IV.3 Topology of anomaly detection based on reconstruction errors.

Anomaly detection based on an autoencoder is one of the best machine learning methods to detect anomalies in a time series [89]. As shown in Figure IV.4, an autoencoder consists of an encoder and a decoder [90]. An encoder is used to reduce and compress the input dimension (X) to a latent space (Z), whereas a decoder is applied to decompress the encoded representation (Z) into the output layer ($\hat{X}$). Therefore, the input and output have the same dimension [91]. In deep learning, autoencoders use several hidden layers to reduce the dimension of the data. In hidden layers, the number of units is reduced hierarchically and, in this process, it is expected that hidden units will select features that well represent the data [92].

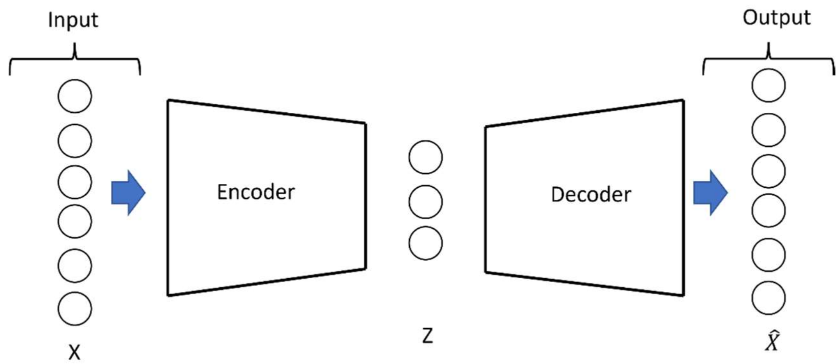

Figure IV.4 Autoencoder framework.

In time series anomaly detection, an autoencoder is trained with a normal training dataset. After that, the trained autoencoder predicts the training set. Later, the difference between the input and output is computed and a reconstruction error vector is obtained. This vector can be used to calculate the threshold. In this work, the metric of MSE is used to compute the reconstruction error.

Various types of autoencoders exist, such as convolutional autoencoders, RNN autoencoders, LSTM autoencoders, and variation autoencoders [83, 91, 92]. For this study, a convolutional autoencoder was utilized to monitor the OLTC's condition. The reason for selecting this type of architecture is that it is not fully connected, allowing it to delve deeper and undergo faster training. This type of autoencoder is based on a convolutional neural network. In a convolutional neural network architecture, convolution layers with kernels serve as adaptable filters that slide across the time steps and variables, capturing temporal patterns and relevant features. Pooling layers are generally used for the temporal down-sampling to further extract the information. In an autoencoder, the convolutional layer, and sometimes the pooling layer, are used in the encoder. In the decoder, convolution transpose layers (also known as deconvolutional layers) and up sampling layers are employed to reconstruct the encoded input [83, 93].

4.3.3 One-Class Classification

One-class classification (OCC), which is a particular case of multi-class classification, is used in the anomaly detection concept. According to OCC, there is only one class used to construct a classifier [94, 95]. Figure IV.5 shows the concept of OCC. As shown in this figure, there is one class, and the data that are placed inside the class are considered normal. In this type of classification, there are two types of objects, which are referred to as target and outlier objects. The objects inside the class are considered the target objects, while all other ones are assumed to be the outlier objects. Therefore, the data inside the class are considered normal and each new piece of data should be analyzed to detect whether it resembles the class or not [96]. KDE is a nonparametric method and can directly estimate density from the data. This technique can be used as a one-class classifier by applying a density threshold. In this regard, the data that are of low density are considered abnormal.

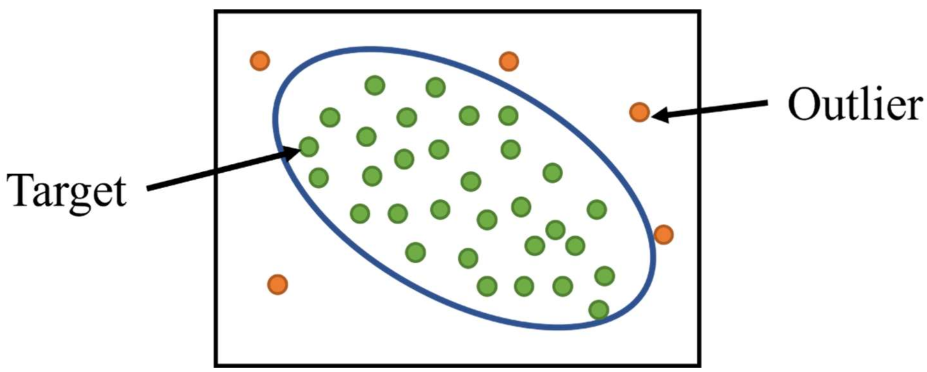

Figure IV.5 The concept of OCC.

KDE is used to estimate a probability density function from a sample of points without any assumption about the underlying distribution. There are two factors, including kernel function and bandwidth, which play an important role in KDE. There are different types of kernel functions, such as exponential, Epanechnikov, and Gaussian. The Gaussian kernel is most popular in applications and was also used in this work [95]. Bandwidth is used to determine the smoothness of the resulting density function. Selecting a very small bandwidth value generates a rough density function. However, selecting a very large value smooths out any true features of the underlying distribution [97].

4.4 Methodology

The proposed methodology is illustrated in Figure IV.6. As shown in this figure, the methodology consists of three parts, including preprocessing, anomaly detection, and the identification of variables responsible for anomalies. In the following, each part of the methodology is explained in detail.

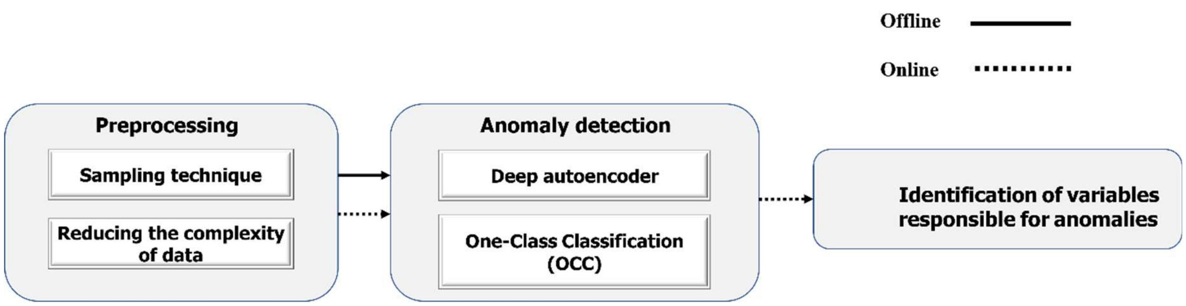

Figure IV.6 The proposed methodology.

4.4.1 Preprocessing

- **Sampling Method:** The sampling technique is applied, with the goal of comparing the six datasets. Instead of comparing the whole datasets, a subset from each dataset is isolated and used. In this regard, the data values that were measured at the same time (year, month, hour, minute) are separated from each dataset.
- **Reducing the Complexity of Data:** The theory of decomposition is used to reduce the complexity of the data. As shown in Figure IV.7, a trend filter is applied to a time series and the trend in the data is separated. After that, the trend is subtracted from the whole time series to obtain the rest of the data (called the Remainder). As such, each part is individually evaluated to detect anomalies.

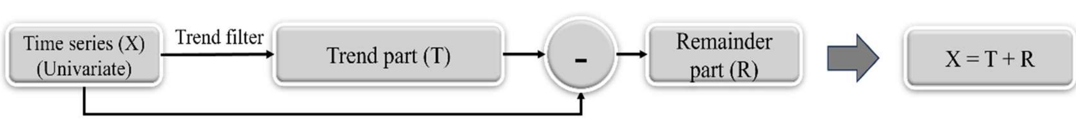

Figure IV.7 Approach used to reduce the complexity of data by applying a trend filter.

Furthermore, a simple moving average is employed to capture the trend component [88]. This technique utilizes a window size to characterize the trend component. It is worth noting that the selection of the window size is crucial. When a small window size, such as 50, is selected, the local trends and sudden variations can be captured. However, when a large window size, such as 500, is selected, the global trends and long-term changes can be captured. Subsequently, each univariate time series is decomposed into two components, the Trend and Remainder, and each component is evaluated individually to identify anomalies. This step is performed twice, using the different window sizes of 50 and 500, in the individual analysis of each dataset, while only window size 50 is used in the comparative analysis. As mentioned, there is a delay in the Trend part because the simple moving average is applied non-symmetrically.

4.4.2 Anomaly detection

The procedure used to detect anomalies is presented in Figure IV.8. As shown in Figure IV.8, anomaly detection is achieved in two ways: offline and online. In the offline technique, after the preprocessing, an autoencoder model is trained with normal data and the reconstruction errors are computed. After that, the anomaly scores of the normal data and the static threshold are computed based on KDE. In the online technique, the trained model is stored in the detection part. A new observation after preprocessing is entered into the online sector and its reconstruction output is established. After that, the reconstruction error is computed, and then its anomaly score is calculated based on the fitted KDE. Finally, if its anomaly score is lower than a dynamic threshold, the new observation is considered abnormal. In the following, the three steps of anomaly detection, including preprocessing, the offline sector, and the online sector, are explained in detail.

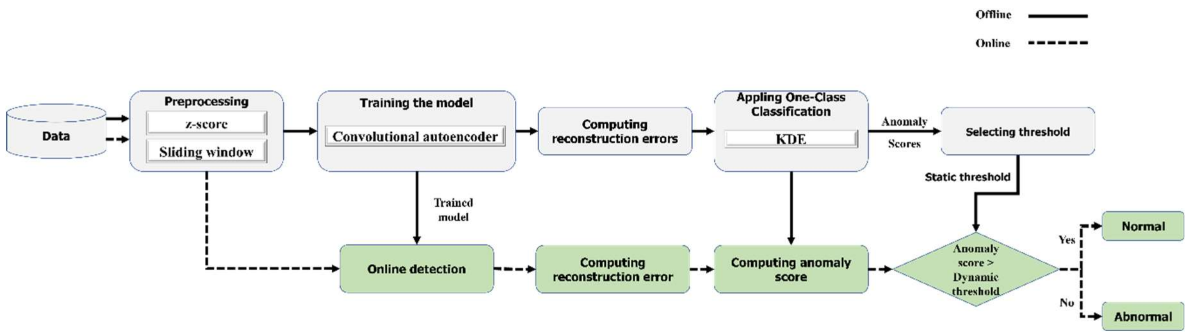

Figure IV.8 The steps of anomaly detection.

- **Preprocessing**
  - **Standardization:** z-score function, presented in Equation (IV.3), is used to standardize the time series data [98].

$$z = \frac{X - \mu}{\sigma} \tag{IV.3}$$

Where μ and σ represent the average and standard deviation of the data.

  - **Sliding window:** A time series can be subdivided into several parts of the same size using the sliding window technique. In this technique, there are two indicators, including window size (W) and step size (s), which indicate the length of the window and the amount of stride in subsequent windows, respectively. In this work, a sliding window with s = 1, which causes the creation of overlapping windows, is applied to achieve a short time series (parts).

- **Offline Sector:** The offline sector includes two parts. In the first part, the model is trained with normal data and, later, the reconstruction error of the normal data is computed. In the second part, KDE is trained with the reconstruction errors and, after that, the log-likelihood of the reconstruction errors in the normal data is computed. It should be noted that a static threshold is also defined in this part.
  - **Training the model:** A convolutional autoencoder is used as a model to detect anomalies. In this model, the encoder and decoder use two layers. It is important to note that the

model is trained using a set that contains normal data. Additionally, a validation set containing normal data is utilized to prevent overfitting and to determine when to halt the training process.

- **Reconstruction errors**: are computed between the original (X) and reconstructed ($\hat{X}$) data. MSE is then used to compute the reconstruction error.
- **The Application of One-Class Classification (extracting anomaly scores based on KDE and selecting a static threshold):** During this stage, the KDE method is utilized and tailored to the reconstruction errors of the training set. Following this, the log-likelihood of every instance in both the training and validation sets is calculated. This reconstruction log-likelihood is used as the anomaly score in the anomaly detection model. As such, a high score indicates that the input X is suitably reconstructed. The threshold is determined by considering the minimum anomaly score found within both the training and validation sets. It should be noted that the threshold is rounded down to the nearest whole number. This means that values such as 2.1 and 2.7 would be rounded down to 2.

- **Online Sector:** The recent measurement (new observation) obtained after the preprocessing steps is entered into the online sector. In the first step, the reconstruction value of the recent measurement is achieved using the trained model. After that, the reconstruction error is computed and, later, its anomaly score is calculated using fitted KDE. Finally, if the anomaly score of the new observation is less than a dynamic threshold, this observation is labeled abnormal; otherwise, it is marked as normal. It should be noted that the smaller anomaly score means that it does not follow the normal pattern.

  The dynamic threshold can be calculated based on k anomaly scores before recent measurements. According to this strategy, k anomaly scores before recent measurements are selected and KDE is fitted with these values. Then, the log-likelihood of each value is computed based on the fitted KDE. Finally, a dynamic threshold is obtained by summing the minimum value between the log-likelihood values (of k anomaly scores before recent measurements) and the static threshold.

4.4.3 Identification of variables at the origin of anomalies

Because the anomaly detection system relies on multiple variables, when an anomaly occurs, it is essential to identify the variables at the origin. To explain how an anomaly is detected, the reconstruction error calculation process should be clarified.

MSE is used to calculate reconstruction errors. For example, if the input has two dimensions (X and Y) and a sliding window as a third dimension, the actual value and its reconstruction value for recent measurements are shown in Equations (IV.4) and (IV.5), respectively. MSE is individually computed for each input variable, and is shown in Equation (IV.6). After that, the standard deviation of the MSE vector is computed and the variable that has a higher MSE value than the standard deviation is considered as the root of the anomaly. With this strategy, it is possible to have more than one variable as the root of anomalies.

$$[[X_t\ Y_t][X_{t-1}\ Y_{t-1}][X_{t-2}\ Y_{t-2}]] \tag{IV.4}$$

$$[[\hat{X}_t\ \hat{Y}_t][\hat{X}_{t-1}\ \hat{Y}_{t-1}][\hat{X}_{t-2}\ \hat{Y}_{t-2}]] \tag{IV.5}$$

$$[MSE_X\ MSE_Y] \tag{IV.6}$$

4.5 Results

The proposed algorithms were implemented in Python 3.9.5, and PyCharm 2021.2.3, which provides an Integrated Development Environment (IDE) for Python. The Keras library was utilized, employing layers of Conv1D. Conv1DTranspose and Dropout operations were used to create a convolutional autoencoder. The convolutional autoencoder architecture comprises both encoding and decoding components. The encoder consists of two consecutive Conv1D layers with n (the number of filters) and n/2 filters, respectively. These layers are used to reduce the dimensionality and extract essential features from the input data. The decoder starts with a Conv1DTranspose layer with n/2 filters, followed by another Conv1DTranspose layer with n filters. These decoder layers are responsible for reconstructing the input data from the latent space representation. The dropout layers with a rate of 0.2 are inserted after the first encoding and decoding layers to prevent overfitting. In addition, loss functions and MSE are used. It is important to note that another Conv1DTranspose layer (the final layer) is used to return the output to the original input dimensionality. In addition, several hyperparameters are optimized, including activation, the number of filters (n), the optimizer, and the batch size. For the activation parameter, two options, tanh and relu, are considered. The n parameter can be either 16 or 32. In terms of optimizers, two options are tested: Adam, with a learning rate of 0.001, and Adamax, with the same learning rate. Finally, the batch size parameter is explored with values of 128 and 256. It should be noted that information regarding the programming is available on the Keras Examples website, as referenced in [99].

The six datasets were analyzed using two distinct strategies: one involves a comparative analysis of six databases, while the other entails an individual analysis of each dataset. Additionally, each dataset is individually analyzed based on two steps: long-term changes and sudden variations. Consequently, Zones 1, 3, and 5 from the six datasets were extracted and compared individually. The data for these zones are presented in Figure IV.9 from left to right, respectively. Furthermore, each of these zones was analyzed individually in each dataset, and it should be noted that temperature was also included as an input in the individual analysis of each dataset. To avoid repetition, the results of T3A-odd and T3B-odd were discussed separately during individual analyses. Zones 1, 3, and 5, with temperature in T3A-odd and T3B-odd, are shown in Figure IV.10 and Figure IV.11.

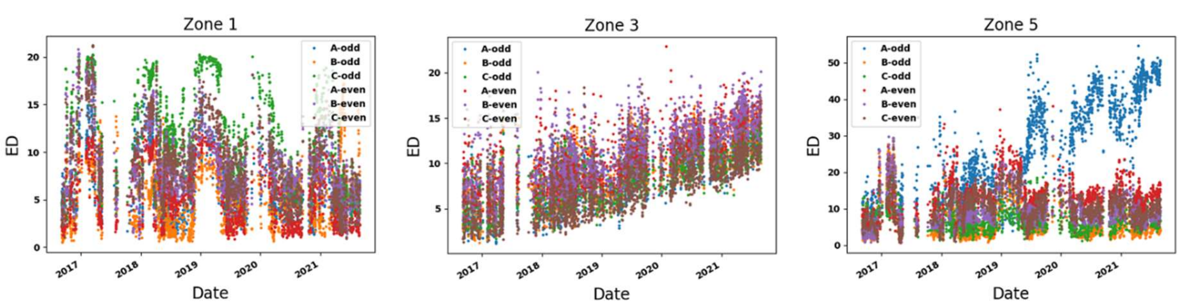

Figure IV.9 Zones 1, 3, and 5 from the six datasets are shown from left to right.

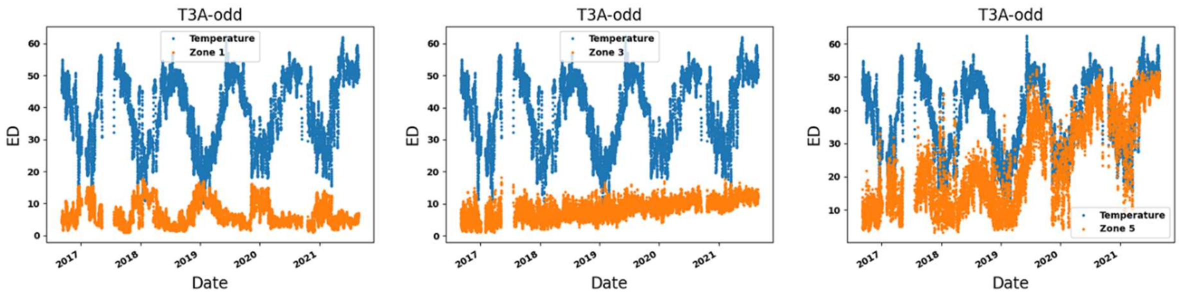

Figure IV.10 Zones 1, 3, and 5 with temperature in T3A-odd.

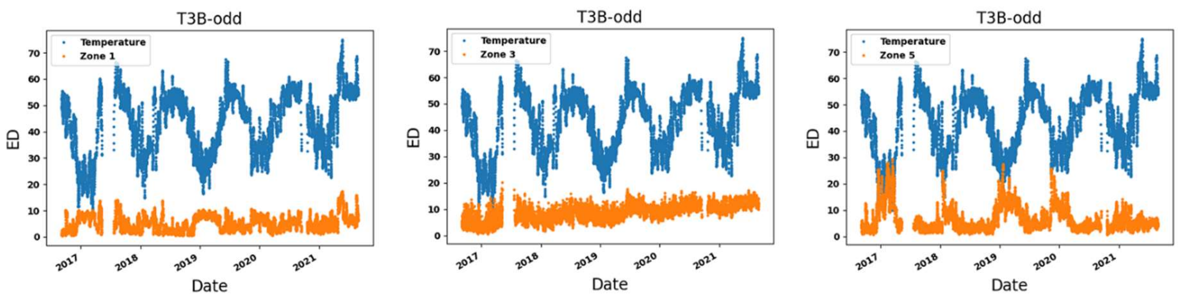

Figure IV.11 Zones 1, 3, and 5 with temperature in T3B-odd.

The OLTC anomalies are detected using two strategies: an individual analysis of each dataset and a comparative analysis. Furthermore, in the preprocessing stage, to achieve the Trend and Remainder parts, window sizes of 50 and 500 are employed in the individual analysis of each dataset, while a window size of 50 is considered in the comparative analysis. Figure IV.12 illustrates an example of the decomposition step for Zone 1 of the six datasets (comparative analysis). After that, each of these parts (the trend and remainder) is subdivided into two groups. The first group contains normal data. This group of data is subdivided into training and validation sets. The second group includes normal and sometimes abnormal data, and this group is called the test set. The convolutional autoencoder is trained using the training set (normal data). The validation set is used to avoid model overfitting. Finally, the test set is used to evaluate the model. In the following, the results related to OLTC anomalies are shown. It should be noted that, within the entire dataset, the data from 1 September 2016, to 1 September 2018, (two years) are considered the training set. The data spanning from 1 September 2018, until 1 January 2019, (four months) are also considered part of the validation set. The remaining data, from 1 January 2019, to 1 September 2021, are referred to as the test set.

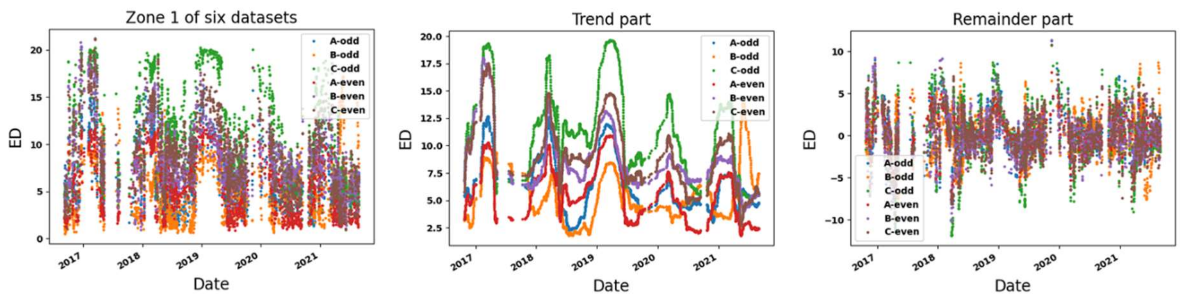

Figure IV.12 Dividing Zone 1 into trend and remainder parts for each dataset (comparative analysis).

4.5.1 Comparative analysis

The results of anomalies in Zones 1, 3, and 5, illustrated in Figure IV.9, are compared in Figure IV.13, Figure IV.14 and Figure IV.15, respectively. Consequently, subfigure (a) presents the training loss and validation loss of the model versus the number of epochs. In the other subfigures, the training, validation, and test sets are represented by blue, green, and black colors, respectively. Additionally, the detected anomalies in the test set are displayed in red. It should be noted that subgraph (b) shows all input variables and the detected anomalies using a dynamic threshold, while subgraphs (c), (d), (e), (f), (g), and (h) display the root of the anomalies shown in subgraph (b) in red. As indicated in these subgraphs, it is possible that the root of anomalies includes more than one input variable.

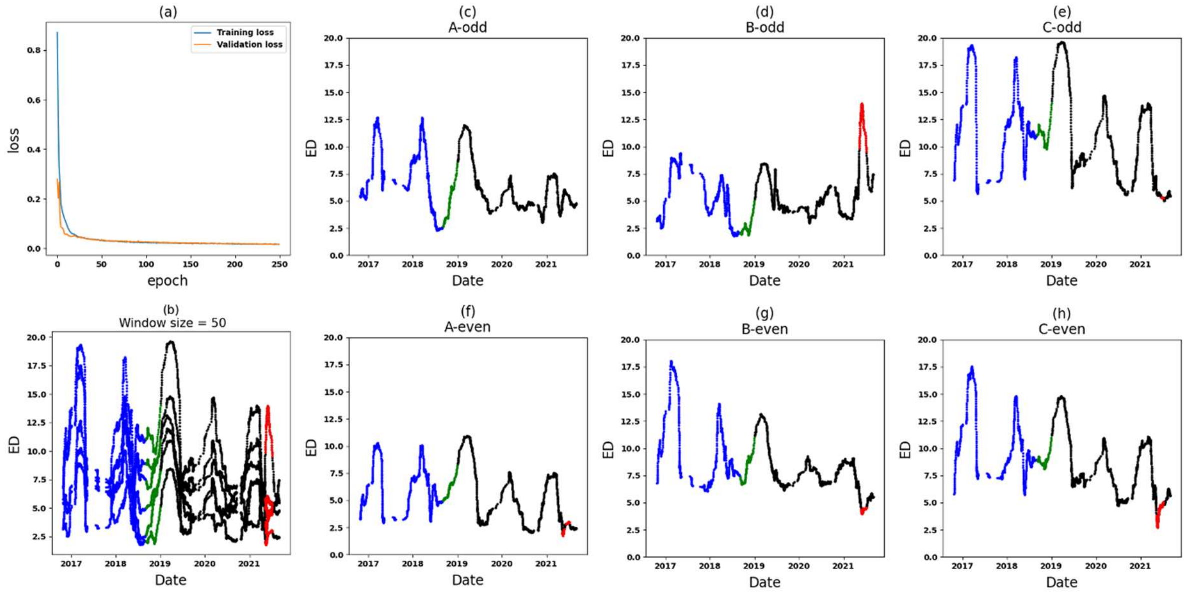

Figure IV.13 The results of anomalies in Zone 1 of the six datasets (comparative analysis). In subgraph (b–h), the training, validation, and test sets are represented by blue, green, and black colors, respectively. Additionally, the detected anomalies in the test set are displayed in red. (a) presents the training loss and validation loss of the model versus the number of epochs; (b) shows all input variables and the detected anomalies using a dynamic threshold. (c–h) display the root of anomalies shown in subgraph (b) in red.

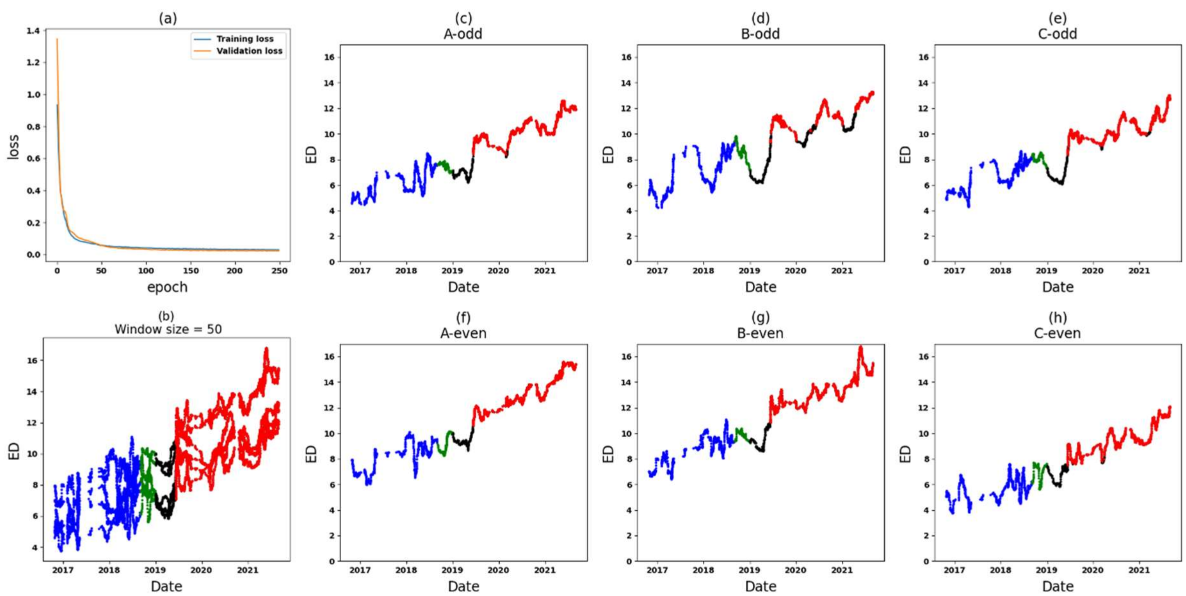

Figure IV.14 The results of anomalies in Zone 3 of the six datasets (comparative analysis). In subgraph (b–h), the training, validation, and test sets are represented by blue, green, and black colors, respectively. Additionally, the detected anomalies in the test set are displayed in red. (a) presents the training loss and validation loss of the model versus the number of epochs; (b) shows all input variables and the detected anomalies using a dynamic threshold. (c–h) display the root of anomalies shown in subgraph (b) in red.

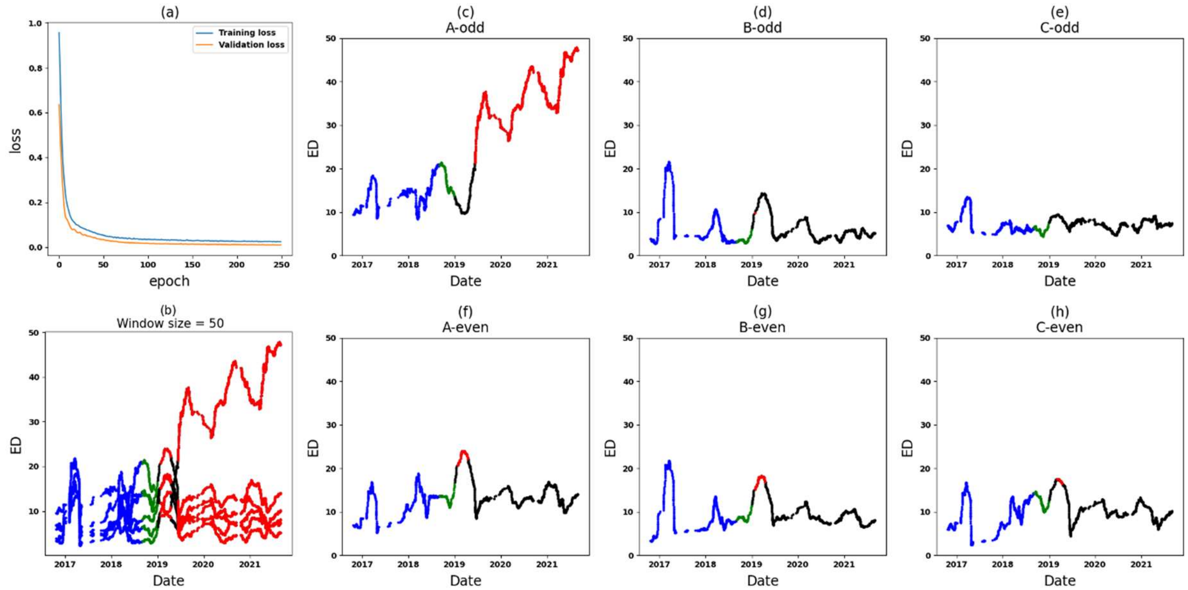

Figure IV.15 The results of anomalies in Zone 5 of the six datasets (comparative analysis). In subgraph (b–h), the training, validation, and test sets are represented by blue, green, and black colors, respectively. Additionally, the detected anomalies in the test set are displayed in red. (a) presents the training loss and validation loss of the model versus the number of epochs; (b) shows all input variables and the detected anomalies using a dynamic threshold. (c–h) display the root of anomalies shown in subgraph (b) in red.

4.5.2 Individual analysis of each dataset

As previously mentioned, the individual analysis of each dataset involves two distinct steps: identifying anomalies related to long-term changes and identifying anomalies related to sudden variations. Consequently, window sizes of 500 are used during the preprocessing step (decomposition) to capture long-term changes, while window sizes of 50 are employed to detect sudden variations. In this section, an examination of Zones 1, 3, and 5 is conducted within both the T3A-odd and T3B-odd datasets to identify anomalies associated with either long-term changes or sudden variations. Anomalies linked to sudden variations are notably detected in Zones 1 and 3 of dataset T3B-odd, showcased in Figure IV.16 and Figure IV.17, and in Zones 3 and 5 of dataset T3A-odd, showcased in Figure IV.18 and Figure IV.19, respectively. Moreover, anomalies attributed to long-term changes are identified in Zones 3 and 5 of dataset T3A-odd, presented in Figure IV.20 and Figure IV.21, along with Zone 3 of dataset T3B-odd, presented in Figure IV.22, respectively.

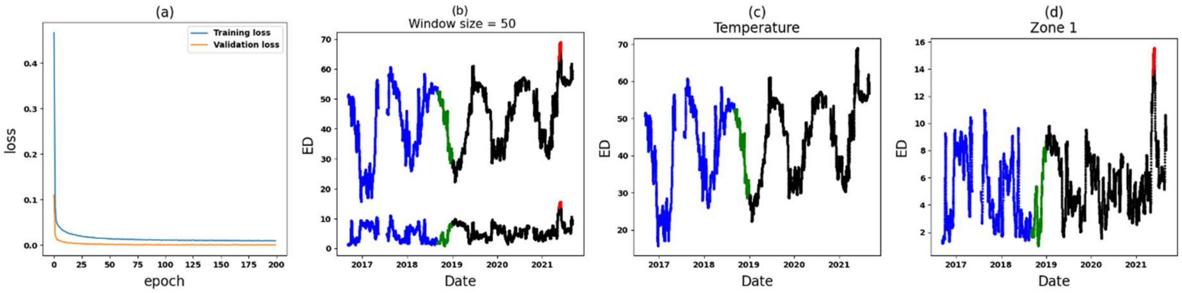

Figure IV.16 Detecting anomalies in Zone 1 of dataset T3B-odd based on sudden variation. (a) displays the model's training loss and validation loss concerning the number of epochs. Subgraphs (b–d) represent the training, validation, and test sets in blue, green, and black colors, respectively. Furthermore, anomalies detected in the test set are highlighted in red. Subgraph (b) exhibits all input variables along with the detected anomalies using a dynamic threshold, while subgraphs (c,d) display the root of the anomalies depicted in subgraph (b) using the color red.

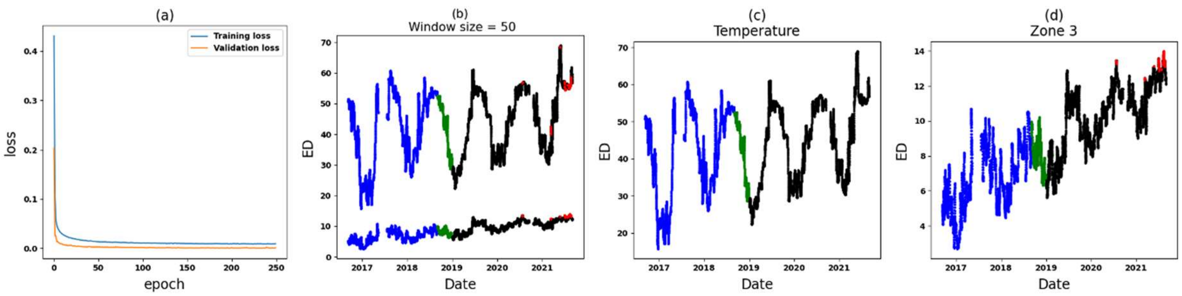

Figure IV.17 Detecting anomalies in Zone 3 of dataset T3B-odd based on sudden variation. (a) displays the model's training loss and validation loss concerning the number of epochs. Subgraphs (b–d) represent the training, validation, and test sets in blue, green, and black colors, respectively. Furthermore, anomalies detected in the test set are highlighted in red. Subgraph (b) exhibits all input variables along with the detected anomalies using a dynamic threshold, while subgraphs (c,d) display the root of the anomalies depicted in subgraph (b) using the color red.

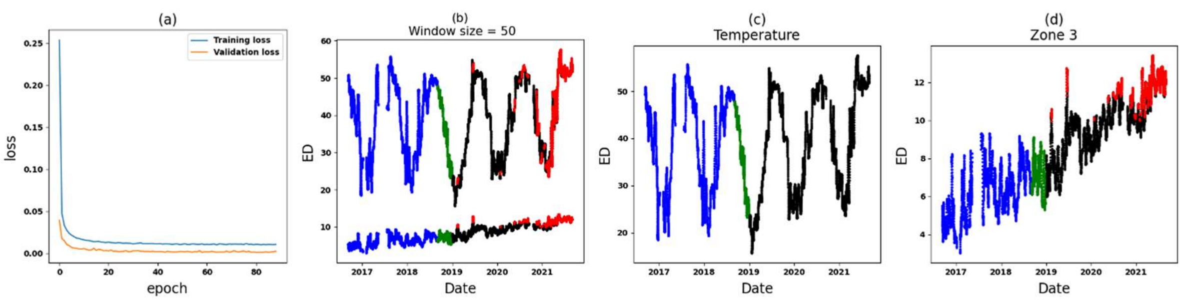

Figure IV.18 Detecting anomalies in Zone 3 of dataset T3A-odd based on sudden variation. (a) displays the model's training loss and validation loss concerning the number of epochs. Subgraphs (b–d) represent the training, validation, and test sets in blue, green, and black colors, respectively. Furthermore, anomalies detected in the test set are highlighted in red. Subgraph (b) exhibits all input variables along with the detected anomalies using a dynamic threshold, while subgraphs (c,d) display the root of the anomalies depicted in subgraph (b) using the color red.

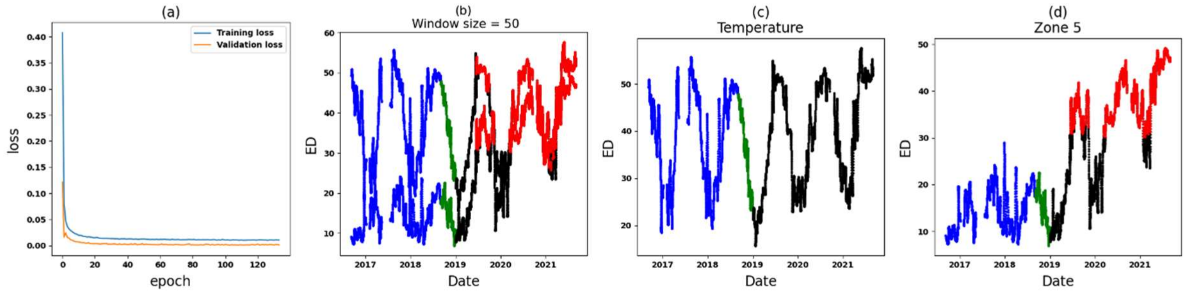

Figure IV.19 Detecting anomalies in Zone 5 of dataset T3A-odd based on sudden variation. (a) displays the model's training loss and validation loss concerning the number of epochs. Subgraphs (b–d) represent the training, validation, and test sets in blue, green, and black colors, respectively. Furthermore, anomalies detected in the test set are highlighted in red. Subgraph (b) exhibits all input variables along with the detected anomalies using a dynamic threshold, while subgraphs (c,d) display the root of the anomalies depicted in subgraph (b) using the color red.

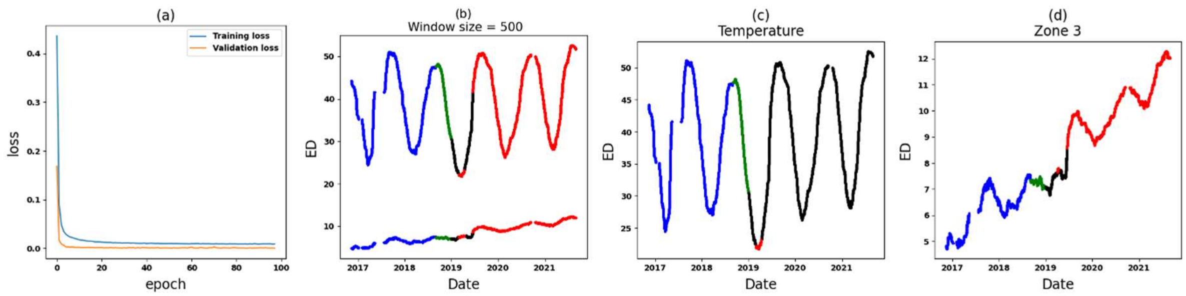

Figure IV.20 Detecting anomalies in Zone 3 of dataset T3A-odd based on long-term changes. (a) displays the model's training loss and validation loss concerning the number of epochs. Subgraphs (b–d) represent the training, validation, and test sets in blue, green, and black colors, respectively. Furthermore, anomalies detected in the test set are highlighted in red. Subgraph (b) exhibits all input variables along with the detected anomalies using a dynamic threshold, while subgraphs (c,d) display the root of the anomalies depicted in subgraph (b) using the color red.

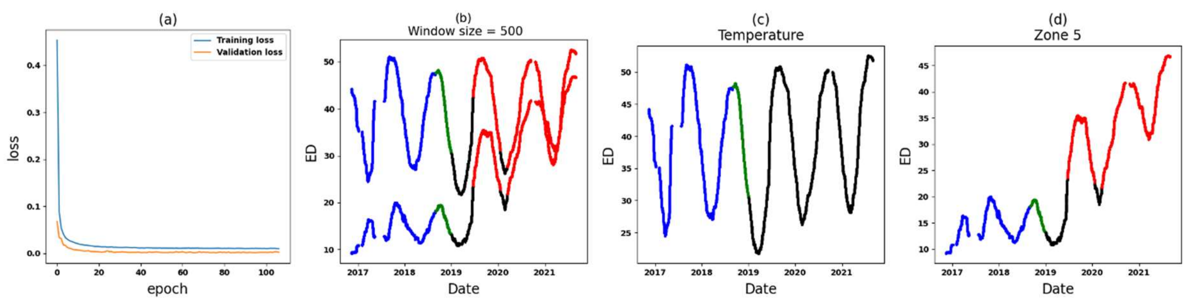

Figure IV.21 Detecting anomalies in Zone 5 of dataset T3A-odd based on long-term changes. (a) displays the model's training loss and validation loss concerning the number of epochs. Subgraphs (b–d) represent the training, validation, and test sets in blue, green, and black colors, respectively. Furthermore, anomalies detected in the test set are highlighted in red. Subgraph (b) exhibits all input variables along with the detected anomalies using a dynamic threshold, while subgraphs (c,d) display the root of the anomalies depicted in subgraph (b) using the color red.

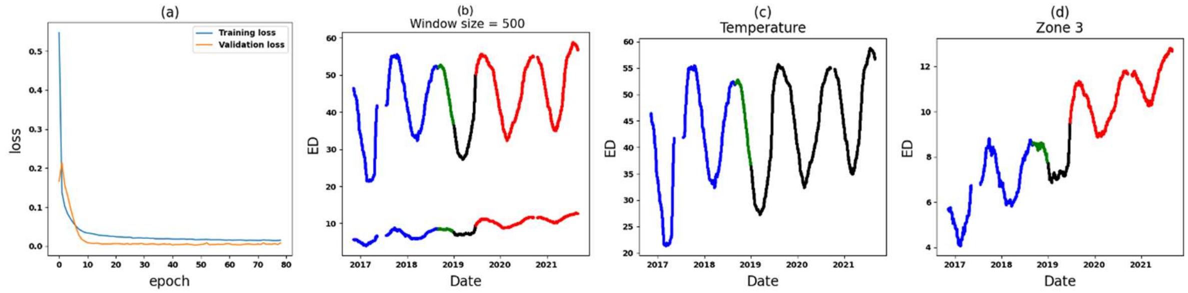

Figure IV.22 Detecting anomalies in Zone 3 of dataset T3B-odd based on long-term changes. (a) displays the model's training loss and validation loss concerning the number of epochs. Subgraphs (b–d) represent the training, validation, and test sets in blue, green, and black colors, respectively. Furthermore, anomalies detected in the test set are highlighted in red. Subgraph (b) exhibits all input variables along with the detected anomalies using a dynamic threshold, while subgraphs (c,d) display the root of the anomalies depicted in subgraph (b) using the color red.

In these figures, subgraph (a) displays the model's training and validation losses concerning the number of epochs. Subgraphs (b), (c), and (d) represent the training, validation, and test sets in blue, green, and black colors, respectively. Furthermore, anomalies detected in the test set are highlighted in red. Subgraph (b) exhibits all input variables along with the detected anomalies using a dynamic threshold, while subgraphs (c) and (d) display the variable responsible for the anomalies depicted in subgraph (b) using the color red.

It should be noted that the remaining parts were also analyzed, and a few anomalies were detected in the comparative analysis, while no anomalies were found in the individual analyses. Therefore, no significant anomalies were detected in the remaining parts.

4.6 Discussion

In this contribution, a convolutional autoencoder and KDE are used to detect anomalies in the extracted features from vibro-acoustic signal envelopes. In addition, in a preprocessing step, the sampling method and trend filter are used to reduce the complexity of the input data. Moreover, standard deviation is utilized to identify the variables that are the origin of anomalies. To evaluate the proposed methodology, Zones 1, 3, and 5 were selected. Recall that Zones 1, 3, and 5 are not random selections. In fact, they were chosen deliberately to assess the proposed methodology. Notably, Zone 3 consistently exhibits a smooth, consistent change, indicative of long-term changes across all datasets. Furthermore, a distinctive pattern is observed in Zone 5 of

T3A-odd compared to Zone 5 in other datasets [81]. Based on the findings of anomalies in Section 4.5, the following observations are made for each Zone, individually.

- **Zone 1:** In the comparative analysis, anomalies are identified in a specific segment of the test set (see Figure IV.13). Following this, Zone 1 of T3A-odd and Zone 1 of T3B-odd are individually scrutinized. Based on the outcomes of the individual analyses, anomalies attributed to sudden variations are found specifically in T3B-odd (see Figure IV.16). These anomalies continue for around 14 days, after which there are no further anomalies. Consequently, it can be inferred that there might not be a significant cause for concern or an important alarm.
- **Zone 3:** In the comparative analysis, anomalies are observed spanning from 9 June 2019, until the end of September 2021 (see Figure IV.14). Notably, a crucial observation within this timeframe is that all input variables (Zone 3 in six datasets) are implicated as the cause of these anomalies, causing significant concern. To further understand the circumstances within this zone, Figure IV.17 and Figure IV.18 depict the results for Zone 3 of the T3B-odd and T3A-odd datasets, respectively, based on sudden variation. Additionally, Figure IV.20 and Figure IV.22 illustrate the results for Zone 3 of the T3A-odd and T3B-odd datasets, respectively, based on long-term changes. Upon examination of these figures, while some anomalies are identified based on sudden variations, it is evident that long-term changes are prevalent in this area. Consequently, the presence of persistent long-term changes raises an important alarm within this particular zone.
- **Zone 5:** In the comparative analysis, anomalies were consistently observed since 9 June 2019. Primarily, these anomalies are attributed to T3A-odd (refer to Figure IV.15). Upon conducting individual analyses of Zone 5 within both T3A-odd and T3B-odd datasets, continuous anomalies are detected solely in Zone 5 of dataset T3A-odd, indicating occurrences associated with both sudden variations and long-term changes. Notably, no anomalies were found in Zone 5 of the T3B-odd dataset. Consequently, these findings strongly suggest that significant alterations occurred specifically within Zone 5 of the T3A-odd dataset (see Figure IV.19 and Figure IV.21).

Based on the above-mentioned points, anomalies can be categorized into three types of alarms: ignorable anomalies, long-term changes, and significant alterations. An analysis of anomalies in Zone 1 reveals the presence of anomalies that can be disregarded. These anomalies likely stem from natural variations such as temperature fluctuations because they occur within a short period; no further anomalies are observed afterward. In Zone 3, the anomalies suggest the existence of long-term changes. Although these changes might not immediately cause faults, they have the potential to create faults in the future. Meanwhile, Zone 5 indicates significant alterations within Zone 5 of T3A-odd, implying the potential occurrence of faults in the near future.

It would be beneficial to note that our application of deep learning for anomaly detection initially encountered challenges due to the complexity of the input variables. However, through rigorous preprocessing steps, including the sampling method and the application of a trend filter, significant improvements were achieved. These preprocessing techniques proved invaluable in managing the complexity of the input data and enhancing the performance of the deep learning model.

Furthermore, the performance of the proposed method was evaluated based on two strategies: an individual analysis of each dataset and a comparative analysis. Although the number of input variables differs between the two strategies, the proposed method is able to detect anomalies as well as identify the variables at the origin of these anomalies. Therefore, the methodology is globally applicable and can be used for any OLTC that has the same monitoring system as that mentioned in this paper.

It should be noted that this work utilizes a dynamic threshold instead of a static one. To compare the anomaly results obtained from dynamic and static thresholds, Zone 1 of T3B-odd and T3C-odd were selected. It is worth mentioning that a window size of 50 was used to establish the trend part. The anomalies based on the dynamic and static thresholds for Zone 1 (trend part) of T3B-odd and T3C-odd are depicted in Figure IV.23, Subgraphs (a), (b), (c), and (d), respectively, in red. As illustrated in these figures, the dynamic threshold was used to disregard anomalies that do not represent a significant cause for concern. Consequently, there are no anomalies in Zone 1 of T3C-odd based on the dynamic threshold (see Subfigure (c)), whereas anomalies exist based on the static threshold in this zone (see Subfigure (d)). Furthermore, it is worth noting that there are more anomalies in Zone 1 of T3B-odd based on the static threshold than the dynamic threshold (see Subfigures (a) and (b)). In future works, the impact of temperature on the vibration signal envelope will be investigated. The aim is to discriminate the effect of temperature (natural variation) on vibration signals.

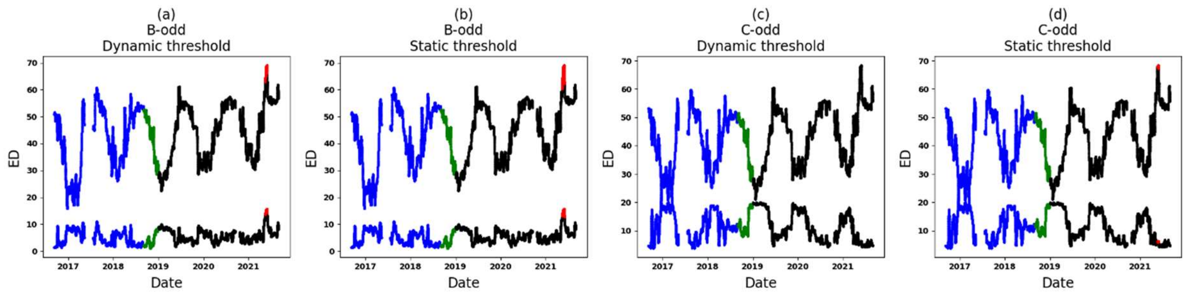

Figure IV.23 Comparison of anomaly results using dynamic and static thresholds in Zone 1 (trend part) of T3B-odd and T3C-odd. Subgraphs (a,b) display anomalies in Zone 1 of T3B-odd based on dynamic and static thresholds, respectively. Subgraphs (c,d) illustrate anomalies in Zone 1 of T3C-odd based on dynamic and static thresholds, respectively. The training, validation, and test sets are represented in blue, green, and black colors across these subgraphs, respectively. Additionally, the detected anomalies in the test set are displayed in red.

4.7 Conclusions

In this research work, the vibro-acoustic signal analysis technique was employed to monitor the power transformer OLTC's health condition. In this context, the vibration signal envelopes generated by the OLTC of three transformers over the past few years were measured. It is important to note that these envelopes were aligned, and the main zones were extracted from them. Subsequently, the ED metric was used to compute the similarity between the monitored envelopes and the reference; this metric was computed on the corresponding zone. In this regard, the extracted feature (ED computation) from the envelopes (with respect to time) was considered in the category of time series data. Based on these features, a new methodology comprising three parts, i.e., preprocessing, anomaly detection, and the identification of variables responsible for anomalies, was developed to detect the behavior of a power transformer OLTC. According to this methodology, each univariate feature was divided into two sectors, the trend and remainder sections, based on a moving average strategy. The decomposition facilitates the capturing of long-term changes and sudden variations. Subsequently, anomalies were detected in each sector based on a multivariate convolutional autoencoder and KDE. Initially, a convolutional autoencoder was applied to obtain reconstruction errors, and KDE was utilized to fit the reconstruction errors to compute the anomaly score, static threshold, and dynamic threshold. Then, a statistical parameter, standard deviation, was used to identify the variables responsible for the anomalies. This proposed methodology was evaluated using six different real datasets via two strategies: comparing OLTC sisters and performing an individual analysis for each dataset. The obtained anomaly results allow for the creation of three distinct alarms to display the OLTC's behavior. These alarms encompass ignorable anomalies, indicating natural variations like temperature that should be disregarded, while alarms indicating long-term changes and significant alterations might represent faults in the far and near future, respectively. Ultimately, the results indicate that the developed algorithms successfully detect anomalies and identify the input variables responsible for anomalies.

Chapitre V

Extraire les paramètres statistiques les mieux adaptés

5.1. Introduction

Les transformateurs de puissance sont parmi les éléments les plus stratégiques du réseau électrique, et leur fiabilité est cruciale pour la fourniture d'électricité aux utilisateurs finaux. Un CPC est l'un des composants clés d'un transformateur, utilisé pour réguler la tension. Il modifie le rapport de transformation des enroulements pour réguler la tension d'entrée/sortie. La plupart des CPC reposent sur la technologie de commutation mécanique. Un développement relativement récent, connu sous le nom de changeur de prises à semi-conducteurs, utilise la technologie thyristor. L'inconvénient de cette technologie est que tous les thyristors non conducteurs connectés aux prises non sélectionnées dissipent toujours de l'énergie en raison de leurs courants de fuite, et leur tolérance aux courts-circuits est limitée. Dans les systèmes mécaniques, une action de commutation est effectuée sans aucune interruption du fonctionnement du transformateur. Cependant, en conditions de service, les contacts se détériorent. Il est rapporté que la défaillance du CPC contribue de manière significative aux pannes de transformateurs. Par conséquent, détecter les défauts du CPC à un stade précoce aide à prévenir ces pannes [13, 21, 100]. Plusieurs techniques sont utilisées pour détecter les défauts du CPC, telles que la DRM, la DGA, l'analyse des signaux vibro-acoustiques, la tension-courant du moteur d'entraînement, l'analyse vibro-arc, etc. [11].

Récemment, plusieurs approches ont été proposées pour détecter les défauts des CPC en utilisant des signaux vibro-acoustiques [20, 22, 24, 25, 38]. Par exemple, dans [24, 25], les principaux pics sont extraits des enveloppes des signaux de vibration pour détecter les conditions des CPC. Ces auteurs utilisent la transformée en ondelettes pour extraire les pics. Dans [22, 38], après extraction de l'enveloppe du signal, une forme d'onde de base est sélectionnée en utilisant le coefficient de corrélation de Spearman, et chaque forme d'onde de position de prise est comparée à cette forme de référence pour évaluer l'état de chaque position de prise. Cependant, dans les approches existantes basées sur les signaux de vibration, il manque une technique qui extrait des caractéristiques basées sur des paramètres statistiques à partir des enveloppes des signaux de vibration.

Un module de surveillance vibro-acoustique a été installé sur des transformateurs en service. Les informations correspondant à chaque changement de prise, y compris la position de la prise, la température ambiante, la température de l'huile supérieure du transformateur et la charge, sont mesurées en continu. Jusqu'à présent, aucun défaut de CPC n'a été observé.

L'objectif de ce chapitre est d'identifier les paramètres statistiques les mieux adaptés (parmi diverses caractéristiques populaires) qui peuvent être utilisés comme caractéristiques potentielles pour détecter les défauts des CPC. Pour ce faire, tout d'abord, les principales zones sont extraites des enveloppes des signaux de vibration (voir Chapitre III). Ensuite, des paramètres statistiques populaires sont calculés pour chaque zone et les paramètres capables de reconnaître les changements dans les enveloppes des signaux sont identifiés comme les paramètres les mieux adaptés. Cela est fait en utilisant le coefficient de régression linéaire, de la valeur-p et du R^2 [101, 102]. Ces paramètres peuvent être utilisés pour détecter les défauts et la dégradation des CPC. Enfin, cette méthodologie proposée aide à détecter et localiser les changements dans les enveloppes des signaux de vibration. Cela peut permettre la localisation des défauts et réduire les coûts de maintenance.

5.2. Extraction des paramètres statistiques les mieux adaptés

Quelques caractéristiques statistiques populaires sont sélectionnées pour l'analyse des zones. Les caractéristiques statistiques sélectionnées incluent le coefficient de corrélation de Pearson (PCC), la RMS, la kurtosis (Kurt), l'asymétrie (Skew), l'écart-type (SD), la valeur minimale (Min), la valeur maximale (Max), le ratio min-max (Minmax), la différence moyenne absolue (AAD), la somme absolue des erreurs logarithmiques (ASLE) et la covariance (Cov) [103, 104]. Ces caractéristiques sont calculées individuellement pour chaque zone. Étant donné que le calcul de certaines caractéristiques implique plusieurs signaux, le signal de référence est utilisé comme deuxième signal à des fins analytiques. Par exemple, l'ASLE est calculée en utilisant le signal de référence et chaque enveloppe individuelle, tandis que certaines caractéristiques telles que la RMS sont calculées uniquement en utilisant chaque enveloppe. Il est entendu que cela est basé sur l'équation empirique des paramètres statistiques sélectionnés. Ensuite, les valeurs moyennes de chaque paramètre sélectionné sont calculées chaque année pour l'ensemble des données. Pour identifier les caractéristiques les mieux adaptées parmi celles sélectionnées, un processus de sélection incluant deux seuils est adopté. Le premier seuil est dérivé en appliquant la technique de régression linéaire, et le coefficient de régression linéaire est extrait des résultats des valeurs moyennes annuelles. Si la valeur absolue du coefficient est supérieure à 0.1 (le premier seuil), cela indique qu'il y a une augmentation ou une diminution du paramètre statistique sélectionné. S'il n'y a pas de changements (augmentation ou diminution) dans la caractéristique statistique sélectionnée, le processus est terminé. Le paramètre statistique sélectionné est considéré comme une caractéristique mieux adaptée uniquement si la valeur-p est inférieure à 0.05 et le R^2 est supérieur à 0.80 (le deuxième seuil). La Figure V.1 illustre les étapes de sélection pour les paramètres statistiques les mieux adaptés.

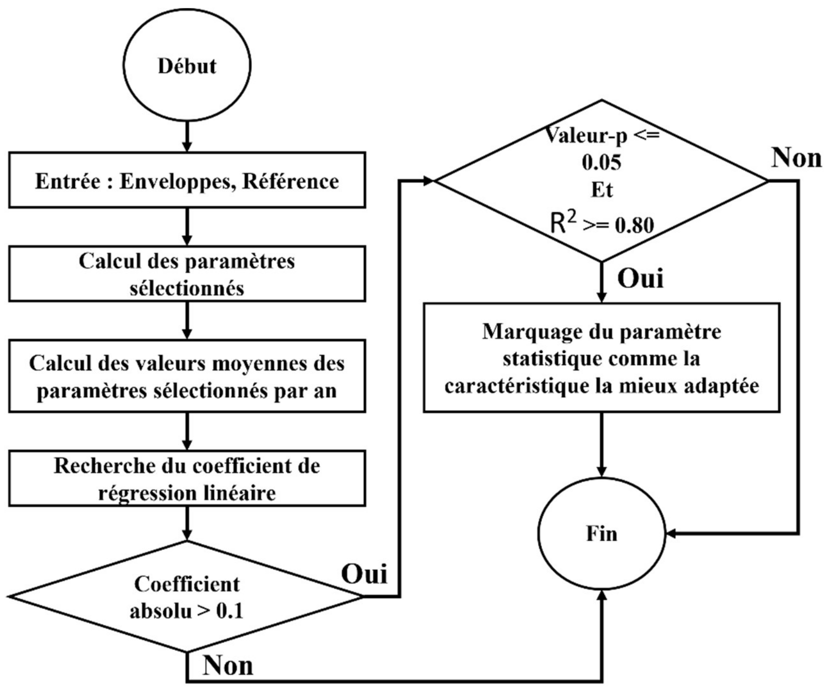

Figure V.1 Illustration du processus d'identification des paramètres statistiques les mieux adaptés.

5.3. Résultats et discussion

Comme le montre la Figure III.9 (b), les enveloppes des signaux de vibration sont subdivisées en huit zones dans le jeu de données T3A-odd. Les paramètres sélectionnés mentionnés dans la section 5.2 sont calculés pour chaque zone individuellement et les résultats relatifs à la zone 5 sont présentés dans la Figure V.2(a). La moyenne de ces valeurs annuelles est calculée et les résultats sont présentés dans la Figure V.2(b).

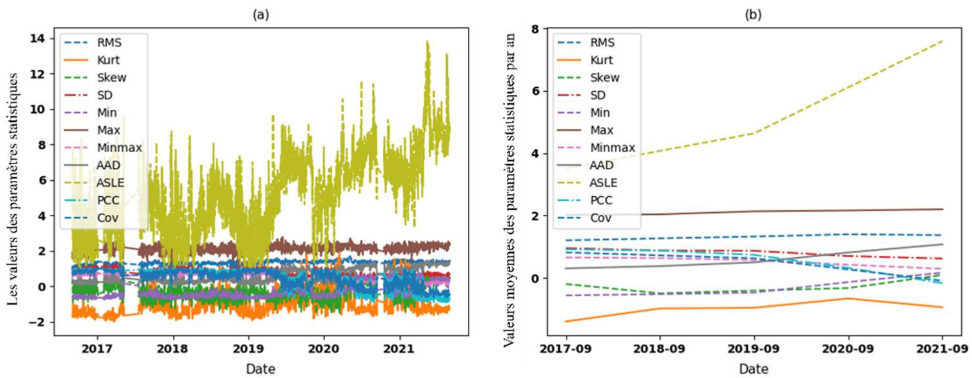

Figure V.2 (a) Les paramètres statistiques sélectionnés calculés dans la zone 5 des enveloppes des signaux de vibration. (b) Les valeurs moyennes annuelles des paramètres statistiques sélectionnés calculés dans la zone 5 des enveloppes des signaux de vibration.

Ces sous-figures montrent que certains paramètres statistiques sélectionnés, tels que la RMS, restent stables, tandis que d'autres caractéristiques, telles que l'ASLE, changent au fil du temps. Pour détecter toute tendance à la hausse ou à la baisse des paramètres, la technique de régression linéaire est appliquée aux valeurs moyennes annuelles des paramètres statistiques. Les paramètres avec des coefficients absolus de régression linéaire supérieurs à 0.1 sont sélectionnés (1er seuil). Les caractéristiques sélectionnées sur la base du premier seuil sont affichées dans la Figure V.3.

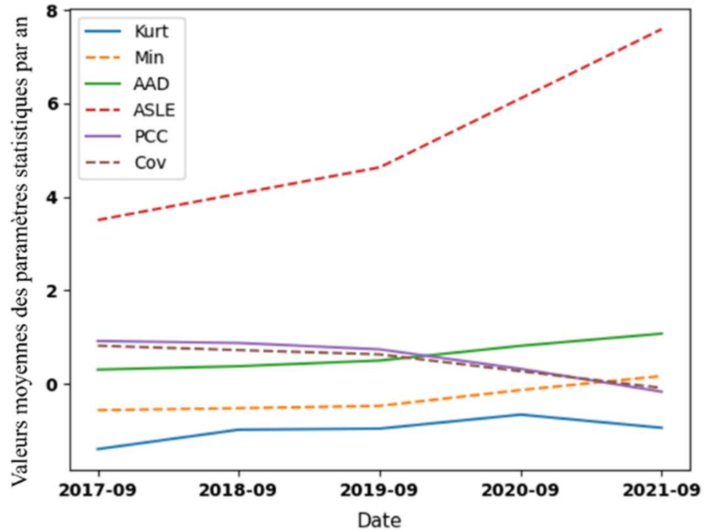

Figure V.3 Les paramètres statistiques les mieux adaptés basés sur le 1er seuil dans la zone 5.

De plus, ce processus est appliqué aux autres zones. Enfin, les résultats obtenus à partir des 1er et 2ème seuils sont sélectionnés comme les paramètres statistiques les mieux adaptés, et les meilleures caractéristiques statistiques finales pour chaque zone sont présentées dans le Tableau V.1 Comme le montre ce tableau, il y a quatre et cinq paramètres statistiques les mieux adaptés pour les zones 3 et 5, respectivement. Il convient de noter que, bien que certains paramètres soient sélectionnés pour les zones 1, 2, 6 et 7 sur la base du 1er seuil, ces paramètres ne sont pas sélectionnés sur la base des seuils de valeur-p et du R^2 (2ème seuil).

Tableau V.1 Les caractéristiques statistiques les mieux adaptées pour chaque zone des enveloppes dans le jeu de données T3A-odd.

Différentes zones dans les enveloppes	1er seuil	2ème seuil
Zone 1	Minmax	---
Zone 2	Kurt	---
Zone 3	Kurt, Minmax, ASLE, PCC	Kurt, Minmax, ASLE and PCC
Zone 4	---	---
Zone 5	Kurt, Min, AAD, ASLE, PCC and Cov	Min, AAD, ASLE, PCC, and Cov
Zone 6	Kurt, Min and ASLE	---
Zone 7	ASLE	---
Zone 8	---	---

5.4. Conclusion

Ce chapitre utilise plusieurs paramètres statistiques populaires pour analyser les signaux vibro-acoustiques dans le cadre de la surveillance des CPC. Ces paramètres statistiques sont calculés pour chaque zone. Ensuite, les paramètres appropriés sont identifiés en utilisant la technique de régression linéaire, la valeur-p et du R^2. Ces paramètres peuvent servir de critères de sélection pour détecter les défauts ou la dégradation des CPC au fil du temps.

Chapitre VI
Autoencodeur variationnel convolutionnel pour la détection d'anomalies dans les CPC

Article publié dans IEEE Access, mars 2025

doi : 10.1109/ACCESS.2025.3550097

Autoencodeur variationnel convolutionnel pour la détection d'anomalies dans les OLTC

Résumé

Les pannes de transformateurs ont un impact significatif sur la fiabilité et l'efficacité des coûts des systèmes électriques. Des études indiquent qu'environ 30 % des défaillances de transformateurs proviennent de problèmes liés aux changeurs de prises en charge (CPC), des composants cruciaux dans le fonctionnement des transformateurs. Par conséquent, la surveillance continue des CPC est essentielle pour améliorer la maintenabilité des transformateurs. Dans cette étude, nous utilisons un système de surveillance basé sur l'analyse des signaux vibro-acoustiques pour évaluer l'état des CPC. Ce système est opérationnel depuis 2016 sur trois autotransformateurs monophasés du réseau Hydro-Québec, mesurant en continu les signaux de vibration de leurs CPC. Notamment, ces transformateurs sont équipés d'unités CPC sœurs, et le système enregistre également la température et d'autres paramètres pertinents. Pour détecter les anomalies des CPC et analyser les signaux de vibration générés, nous utilisons un autoencodeur variationnel convolutionnel (CVAE), entraîné individuellement pour chaque famille de transformateurs. Cette approche nous permet de mapper l'enveloppe du signal dans un espace latent bidimensionnel à l'aide du composant encodeur du CVAE, facilitant ainsi l'investigation et l'analyse visuelles. Le composant décodeur reconstruit l'entrée originale à partir des données dans l'espace latent. Nous évaluons plusieurs seuils basés sur les erreurs de reconstruction pour détecter les anomalies, obtenant des seuils optimaux pour chaque famille. Cela se traduit par des taux de détection d'anomalies de 4 %, 5 % et 2 %, respectivement, lorsqu'ils sont testés sur des données de la même famille non utilisées pendant la phase d'entraînement. En outre, lorsqu'ils sont testés sur des données des deux autres familles, les taux de détection d'anomalies sont de 99 %, 99 % et 100 %, respectivement. Ces résultats soulignent l'exactitude et l'efficacité de la méthodologie pour identifier les anomalies dans le fonctionnement des CPC et distinguer entre différentes familles de transformateurs. Par conséquent, elle est prometteuse pour identifier de manière préventive les anomalies potentielles futures.

Convolutional Variational Autoencoder for Anomaly Detection in OLTC

Abstract

Transformer outages significantly impact the reliability and cost efficiency of power systems. Studies indicate that approximately 30% of transformer failures stem from issues with OLTC, crucial components in transformer operation. Therefore, continuous monitoring of OLTCs is essential to enhance transformer serviceability. In this study, we employ a vibro-acoustic signal analysis-based monitoring system to assess the condition of OLTCs. This system has been operational since 2016 on three single-phase autotransformers within the Hydro-Québec network, continuously measuring vibration signals from their OLTCs. Notably, these transformers are equipped with sister OLTC units, and the system also records temperature and other pertinent parameters. To detect anomalies in OLTCs and analyze the generated vibration signals, we utilize a convolutional variational autoencoder (CVAE), trained individually for each transformer family. This approach allows us to map the signal envelope into a two-dimensional latent space using the encoder component of the CVAE, facilitating visual investigation and analysis. The decoder component reconstructs the original input from data in the latent space. We evaluate several thresholds based on reconstruction errors to detect anomalies, achieving optimal thresholds for each family. This results in anomaly detection rates of 4%, 5%, and 2%, respectively, when tested on data from within the same family not used in the training phase. Furthermore, when tested on data from the other two families, the anomaly detection rates are 99%, 99%, and 100%, respectively. These findings underscore the methodology's accuracy and effectiveness in identifying anomalies in OLTC operations and distinguishing between different transformer families. Consequently, it holds promise for preemptively identifying potential future anomalies.

6.1. Introduction

Transformers play a crucial role in electric power systems by performing essential tasks such as voltage conversion and electrical isolation. Therefore, it is imperative to monitor transformer components to avoid power system outages [105, 106]. In this regard, the OLTC is a key component within transformers, primarily responsible for regulating voltage levels. Literature indicates that approximately 30% of transformer outages are due to faults in this component [13]. Consequently, detecting OLTC faults in the early stages is crucial to prevent transformer outages. Several techniques are available to detect OLTC faults, each capable of identifying specific types of faults. These techniques include dynamic resistance measurement, dissolved gas-in-oil analysis, vibro-acoustic signal analysis, motor-drive voltage-current analysis, vibro-arcing analysis, switching current analysis, and arcing power analysis [11]. In this work, vibro-acoustic signal analysis is applied to detect OLTC faults. This technique is selected because it is supposed to detect many types of faults. Additionally, this technique can be applied online and in real-time.

A thorough literature review reveals the development of several approaches to evaluate an OLTC's behavior based on vibro-acoustic signals. In several works, the bursts in vibro-acoustic signal envelopes are extracted to evaluate the OLTC's condition. In this regard, information, including the number of bursts, the amplitude of bursts, and the time lag between them, can be used to assess the condition of the OLTC [23-25, 58]. In [39], synchronization was achieved for the vibration signal using dynamic resistance measurements to filter out acoustic pulses unrelated to OLTC switching stages. Subsequently, the FFT is used to divide the frequency spectrum of the acoustic pulses into five frequency bands. After that, the energy of each band is computed to evaluate the OLTC condition. Employing this methodology enables the detection of arcing and various defects within a single-phase tap-changer. In [107], preprocessing is conducted in both the time and frequency domains, decomposing the vibration signal into voiced and silent sections. Following this step, each section of the test signal and reference signal is compared to identify normal or abnormal OLTC behavior. Additionally, in this work, the motor current signal is measured and analyzed. In [108], mechanical vibro-acoustic signals and high-frequency current signals are employed to evaluate OLTC behavior. To reduce noise in these signals, the WPT is applied. Correlation analysis is then used to understand the relationships among various states. Features are extracted by Ensemble Empirical Mode Decomposition and the Hilbert-Huang Transform. Finally, the classification of the OLTC contact state is performed using a Support Vector Machine.

A monitoring system based on vibro-acoustic signal analysis was installed on transformers of the Hydro-Québec network. Since 2016, this system has enabled continuous measurement of the vibro-acoustic signals generated by OLTCs and temperatures [81]. It is worth mentioning that vibration signals are highly complex and contain a lot of information. Consequently, the technique of signal envelope extraction is applied to effectively isolate the envelope from the vibration signals. This technique aims to extract important and useful information from the vibration signal. In this monitoring system, the Hilbert Transform and a low pass filter are utilized to extract the envelope. Additionally, a time lag between signal envelopes due to temperature changes is addressed by using the technique of time realignment to eliminate this lag [43, 74]. However, there are challenges, such as detecting anomalies and analyzing the measured vibro-acoustic signal envelopes over time.

Anomaly detection focuses on discovering unusual patterns, rare events, or deviations from expected behavior within datasets. It is crucial in various domains such as fraud detection, network security, and industrial monitoring. Depending on the availability of labeled data, anomaly detection methods are typically categorized as supervised or unsupervised [109-111]. Techniques commonly applied in this field include Artificial Neural Networks (ANN), statistical models, Support Vector Machines (SVM), clustering algorithms, and others [112]. The goal of an ANN is to function like the human brain by imitating neurons. Recently, the use of deep neural networks for anomaly detection in various fields has increased significantly, driven by their scalability and flexibility. One such method is the autoencoder [110, 112].

An autoencoder is a type of neural network that consists of an encoder and a decoder. The encoder compresses the input into a latent space, while the decoder decompresses the data to achieve the reconstructed value of the input (see Figure VI.4(a)) [113]. This architecture has been utilized in anomaly detection. As such, the autoencoder is trained with a training dataset. After training, it is expected that the model will create a large reconstruction error for anomalous data and a small reconstruction error for normal data [114-116]. In this regard, a variational autoencoder (VAE) is a specialized type of autoencoder that also consists of an encoder and a decoder. However, unlike a standard AE, where the encoder outputs a single point in the latent space, the encoder in a VAE generates a distribution over the latent variables, commonly choosing a Gaussian distribution (see Figure VI.4(b)). This characteristic enables the model to generate new data points by sampling from this distribution, making VAEs particularly useful for tasks such as generative modeling and unsupervised learning [110, 117-119]. Additionally, in [120], two dimensions are considered for the latent space, allowing each input to be displayed in a two-dimensional diagram, referred to as the 2D Visualization Tool in this article. Moreover, in [121], the study has successfully demonstrated the use of 2D latent space visualization for detecting state changes in machining processes.

In this research, we employ a CVAE, aimed at visualizing 2D data, generating and predicting anomaly envelopes, and detecting anomalies in vibro-acoustic signal envelopes. The CVAE architecture contains two main components: an encoder, and a decoder. The encoder reduce the dimensionality of the input through successive layers, transforming the data into a two-dimensional latent space, which follows a Gaussian distribution. This low-dimensional representation not only facilitates the visualization of each envelope as a point on a 2D diagram but also supports the generation and prediction of anomaly envelopes. The decoder mirrors the encoder's layers but in reverse, which causes it to progressively reconstruct the original dimensions from the latent space. Anomaly detection is achieved by calculating the absolute error between the input and its reconstruction, setting a threshold above which data is flagged as anomalous.

6.2. Switch operations, data collection, and preprocessing in OLTC model UC

In this paper, the ABB-UC OLTC model [81] is analyzed. This type of OLTC is mounted inside the transformer tank. The following subsections detail the switching operation of the OLTC and the collection and preprocessing of vibration signals from it are detailed.

6.2.1. Switching operations

In the ABB-UC model, there are two selectors (odd and even), and a switch is used to establish a connection between the even and odd sides. The details of the operation of this model, especially the transition sequence (tap changing) from the even side to the odd side in the OLTC model UC, are illustrated in Figure

VI.1. As depicted in this figure, subgraph (a) represents the current passing through the main contact of the odd selector from tap 3. Furthermore, the even selector arm is positioned at tap 2 and does not carry current, allowing it to move freely. In subgraph (b), it is shown that the even selector arm shifts from position 2 to position 4. Since it does not carry any current, no arc is generated during this movement. Meanwhile, the current continues to flow through the odd selector positioned at tap 3. In subgraph (c), it is depicted that the switch breaker begins a movement from the odd side to the even side. In subgraph (d), it is evident that the switch establishes connections simultaneously from both the odd and even sides. Consequently, a short circuit occurs, and the transition resistor helps in mitigating and limiting the impact of this short circuit. In subgraph (e), it is depicted that the switching process is completed, allowing the current to flow exclusively through position 4. Consequently, the odd selector is entirely removed from the circuit.

In addition, Figure VI.2 shows images depicting the contact of odd and even side in the OLTC model ABB-UC. In this figure, subgraph (a) displays both the odd and even sides of the OLTC model ABB-UC. As illustrated in this subgraph, the current is carried from the main switch on the even side. The tap changer is now set to change the tap from the odd side. Consequently, the main switch on the even side is disconnected (see subfigure (b)). Subsequently, the auxiliary switching on the odd side is closed and simultaneously, it is connected on both sides (see subgraph (c)). Then, the auxiliary switch on the even side is disconnected (see subgraph (d)) and the main switch on the odd side is connected (see subgraph (e)). Finally, the current is carried from the main switch on the odd side (see subgraph (f)).

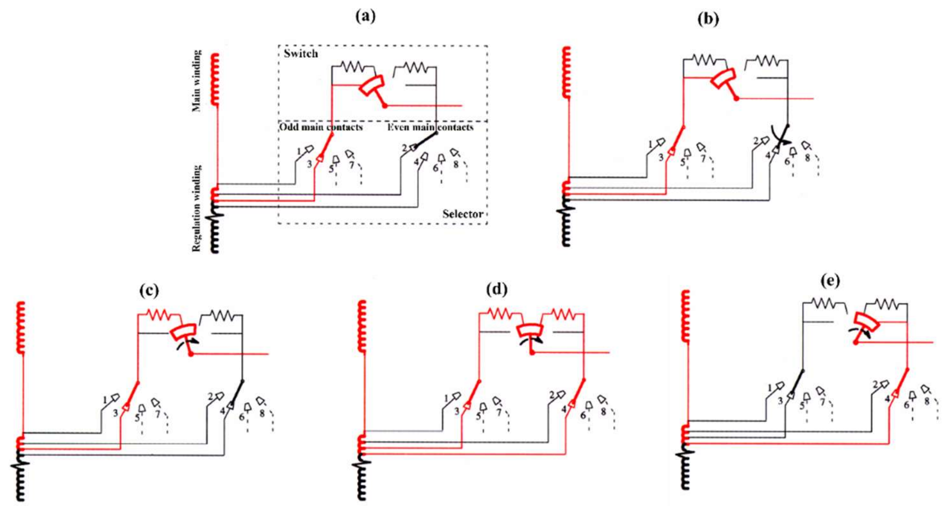

Figure VI.1 The transition sequence (tap changing) from the even side to the odd one in the OLTC model UC.

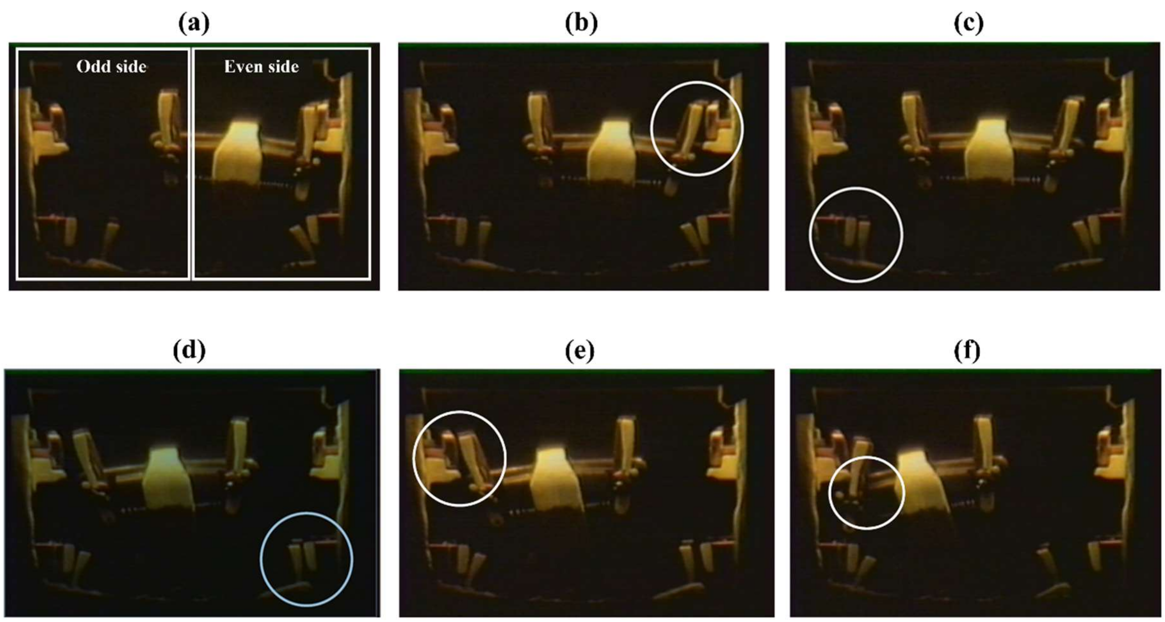

Figure VI.2 The odd and even side sequences of the OLTC model ABB-UC.

6.2.2. Data collection and preprocessing

The monitoring system was installed on three transformers, referred to as T3A, T3B, and T3C, operating on the Hydro- Québec network. The system utilizes an accelerometer sensor to measure the vibration signals generated by the OLTC. Additionally, a sensor monitors the temperature, which affects vibro-acoustic signals [81]. This system has been continuously collecting data since 2016, including vibration signals, tap position, transformer top-oil temperature, and load. Notably, due to the mechanical design of the OLTC, which includes odd and even switches, each dataset can be subdivided into odd and even sets. Consequently, there are six datasets available for analysis: T3A-odd, T3A-even, T3B-odd, T3B-even, T3C-odd, and T3C-even. In this article, the transformers T3A, T3B, and T3C are referred to as families, keeping in mind that each family contains two datasets, one for the odd and one for the even switches. It should be noted that, so far, no faults have been detected.

It should be emphasized that the measured vibro-acoustic signals are complex and contain substantial information. To reduce data storage size, the signal envelope extraction technique is employed to derive useful information. Various methods that allow for extracting a signal envelope such as Hilbert transform, Low Pass Filter (LPF), Moving Average (MA), wavelet transform, Savitzky-Golay filter, Hilbert–Huang Transform (HHT), and Variational Mode Decomposition (VMD) can be found [22, 38, 42, 45, 48, 118, 122]. For this research, the Hilbert transform and LPF are utilized to extract the signal envelope. The decision to use these two methods was made by Hydro-Québec researchers after extensive analysis conducted before 2016. Since 2016, only the envelopes of the measured vibration signals have been stored, and the original vibration signals are not retained. Recall that temperature influences vibration signals, creating a time lag between the measured vibro-acoustic signals. Therefore, to facilitate comparison of vibro-acoustic signals, it is necessary to eliminate the time lag between them. In this study, the technique of time realignment is applied to remove this time lag between vibro-acoustic signal envelopes [43, 74]. Figure VI.3 displays all the measured vibration signal envelopes (more than 13500 envelopes) from 2016 to 2023 for the odd dataset of family T3A. As shown in this figure, the time-lags between envelopes are removed. It should be noted that combined logarithmic and linear scales are also used on vibro-acoustic signal envelopes.

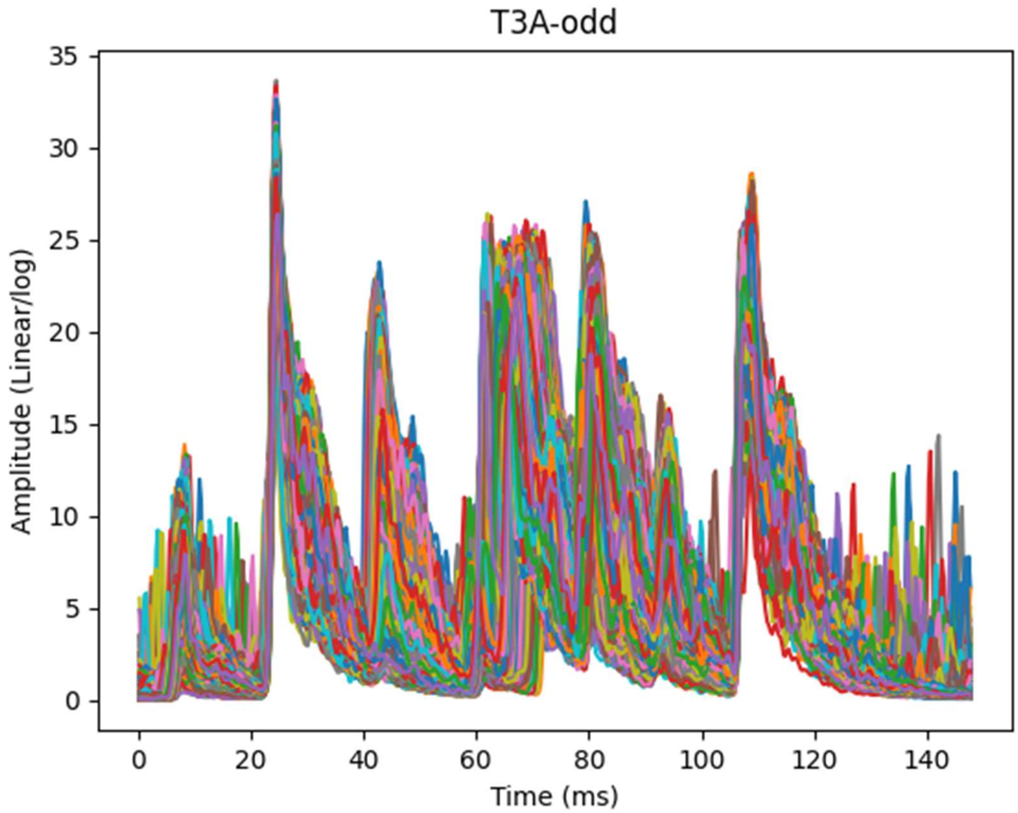

Figure VI.3 All measured vibration signal envelopes dataset recorded from 2016 to 2023 regarding T3A-odd.

6.3. The underlying concept

6.3.1. Autoencoder

An autoencoder is a type of neural network architecture specifically designed to reconstruct its input. Its primary goal is to produce an output that closely resembles the input, although there is typically some degree of error between the input and output. During the training phase, the network actively works to minimize this error. Autoencoders have various applications, including classification, anomaly detection, and dimensionality reduction, among others [123-126].

An autoencoder consists of two primary components: an encoder and a decoder. The encoder is typically used to reduce the dimension of the input into a latent space, which it accomplishes with one or more layers. Meanwhile, the decoder attempts to produce an output that closely resembles the input, thereby increasing the dimension from the latent space. This architecture is illustrated in Figure VI.4(a).

Autoencoders are notably employed in anomaly detection, categorized based on reconstruction error. This model strives to produce an output that closely resembles the input, utilizing reconstruction error to identify anomalies. Autoencoders operate in two modes for anomaly detection: offline and online. In the offline mode, the model is trained on a dataset (training set). Additionally, a threshold is established for determining anomalies. In the online mode, recent measurements are assessed against this threshold. The reconstruction value for recent measurements is achieved using the trained autoencoder. The reconstruction error is then determined, and if this error significantly deviates from the threshold (either above or below, depending on how the anomaly score is configured), the data is flagged as abnormal [115, 127].

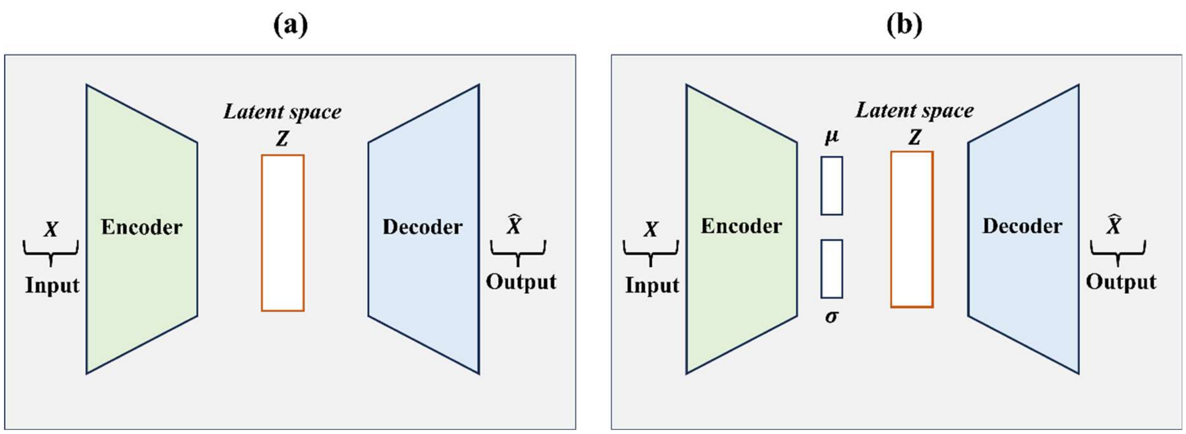

Figure VI.4 (a) The architecture of an autoencoder. (b) The architecture of a variational autoencoder.

6.3.2. Convolutional variational autoencoder

A VAE, similar to an AE, includes an encoder and a decoder in its architecture; however, the structure of the latent space differs. In a VAE, the latent space is defined by two vectors, μ and , which represent the mean and standard deviation of a normal distribution, respectively. In contrast, in an AE, the latent space is defined by a function. In this regard, VAEs have the attribute of generating diverse outputs by sampling from the defined distribution, allowing for the creation of new, varied data instances [116, 119]. Figure VI.4(b) displays the architecture of a VAE. There are several types of VAEs, including LSTM-VAE, CVAE, and GRU-VAE, among others [116, 122, 128]. In this work, the encoder and decoder used are composed of a convolutional neural network which are a multi-layer perceptron designed to recognize N-dimensional shapes with a high degree of invariance to translation, scaling and rotation (1D for time series, 2D for images, 3D for videos). In order to capture spatial organization information, each envelope signal was split into 20 vectors of 24 components to provide an image-shaped input.

A CNN, or Convolutional Neural Network, is a type of neural network primarily used in visual imagery analysis. It aims to extract local patterns from small regions within the input data. Therefore, by incorporating CNN layers into the encoder network, the local patterns in the input can be effectively extracted to achieve a meaningful latent space [129]. The encoder of the CVAE includes convolutional layers and often consists of pooling layers, while the decoder of the CVAE performs the reverse operations of convolution and pooling [130].

6.4. Methodology

This study employs a deep convolutional autoencoder targeted at 2D visualization. The encoder includes layers to reduce the dimensions of the input and compress it into a two-dimensional latent space. Conversely, the decoder utilizes convolutional transpose layers to incrementally increase the spatial dimensions and reduce feature depth, reconstructing the original input value from the latent space. This architecture enables the display of each signal envelope on a 2D graph and facilitates the generation of new signal envelopes based on latent space. Anomalies are detected by computing reconstruction errors. In the following, the preprocessing steps, the encoder and decoder models, and the detection of anomalies are explained in detail.

6.4.1. Preprocessing

- **Normalization:** Each envelope is normalized by selecting the maximum value within the envelope and dividing all samples in that envelope by this maximum value. Therefore, each vector is transformed such that its values range between 0 and 1, with the maximum value becoming 1. The minimum value will be 0 if the original envelope contained a zero sample.
- **Conversion to 2D Data:** Each envelope, containing 500 samples in a vector, is converted into 2D data with dimensions of 20×24. As the dimensions 20×24 accommodate only 480 samples, it is necessary to ignore 20 samples from each envelope. In this regard, the first and

last 10 samples are disregarded because they typically do not contain significant spatial events and are mostly stable (see Figure VI.3).

6.4.2. Architecture of CVAE network

- **Encoder:** The encoder component comprises a stack of layers, which sequentially transform the input vector and pass it to the adjacent layer. The first layer applies a convolution kernel to the layer input with no padding and a stride of (2,2) as parameters. The number of kernels is 32 and their size is fixed at 3. The second layer similarly applies a second convolution kernel, using 64 kernels. The third layer is a fully-connected layer. The fourth layer is composed of two multi-layer networks to respectively estimate the mean and variance of the normal distribution over latent space. The last layer randomly samples a point from the distribution. This architecture of the encoder is displayed in Figure VI.5.

  Utilizing the CVAE, the two-dimensional latent space enables the visualization of each envelope on a diagram plotted along axes Z[0] and Z[1]. This method allows a visual analysis of temporal and spatial changes in the data over time.

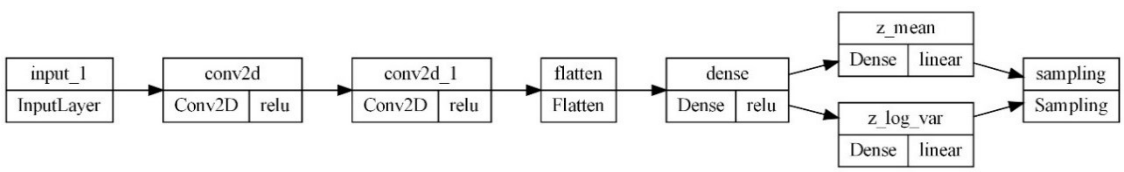

Figure VI.5 Architecture of encoder.

- **Decoder:** As shown in Figure VI.6, the decoder component consists of a set of layers that take points from latent space as input and reconstructs the corresponding vectors initially presented to the encoder.

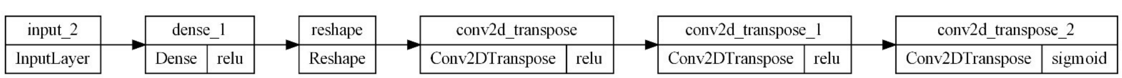

Figure VI.6 Architecture of decoder.

The subtlety and advantage of using a decoder in this architecture are that it takes a point from the latent space as input to generate or reconstruct envelopes. These envelopes are similar to the real data shown during the learning session and can exhibit various degrees of distortion and deformation.

6.4.3. Detecting anomalies

After training the CVAE network, each envelope vector is presented as input to the encoder to compute its response, which is then propagated to the next layer. This propagation continues from one layer to the next until it reaches the final layer at the decoder's output, where the input vector is reconstructed as accurately as possible. The absolute difference between the input and the output is calculated and determined as the reconstruction error. Typically, a histogram of the error vector elements is created by selecting an appropriate number of bins to cover the range of values in the error vector, and thus a threshold for anomaly detection is defined. In this work, the maximum reconstruction error on the training set is defined as the default threshold.

6.5. Results and discussion

In this study, the proposed methodology is implemented in Python using the Keras library. More details about the programming can be found on the Keras Examples website, as referenced in [131]. As such, the objectives of the methodology are to demonstrate 2D visualization, data generation from the latent space, and anomaly detection. This methodology is applied to individually analyze three distinct families: T3A, T3B, and T3C. Each family is subdivided into odd and even groups. Figure VI.7 illustrates all six subsets, which were measured from September 2016 until December 2023. The CVAE network is trained individually with each family (T3A, T3B, and T3C) for both the odd and even subsets, spanning from September 2016 until March 2022. The remaining data is used for network validation. Subsequent results for each family are presented and discussed in the following subsections, including encoding and visualization, generating envelopes, and detecting anomalies. It should be noted that the 32-64 configuration of the CVAE yielded the best results compared to other configurations tested in our experiment (e.g., 32-16, 64-32-16, 16-8, etc.).

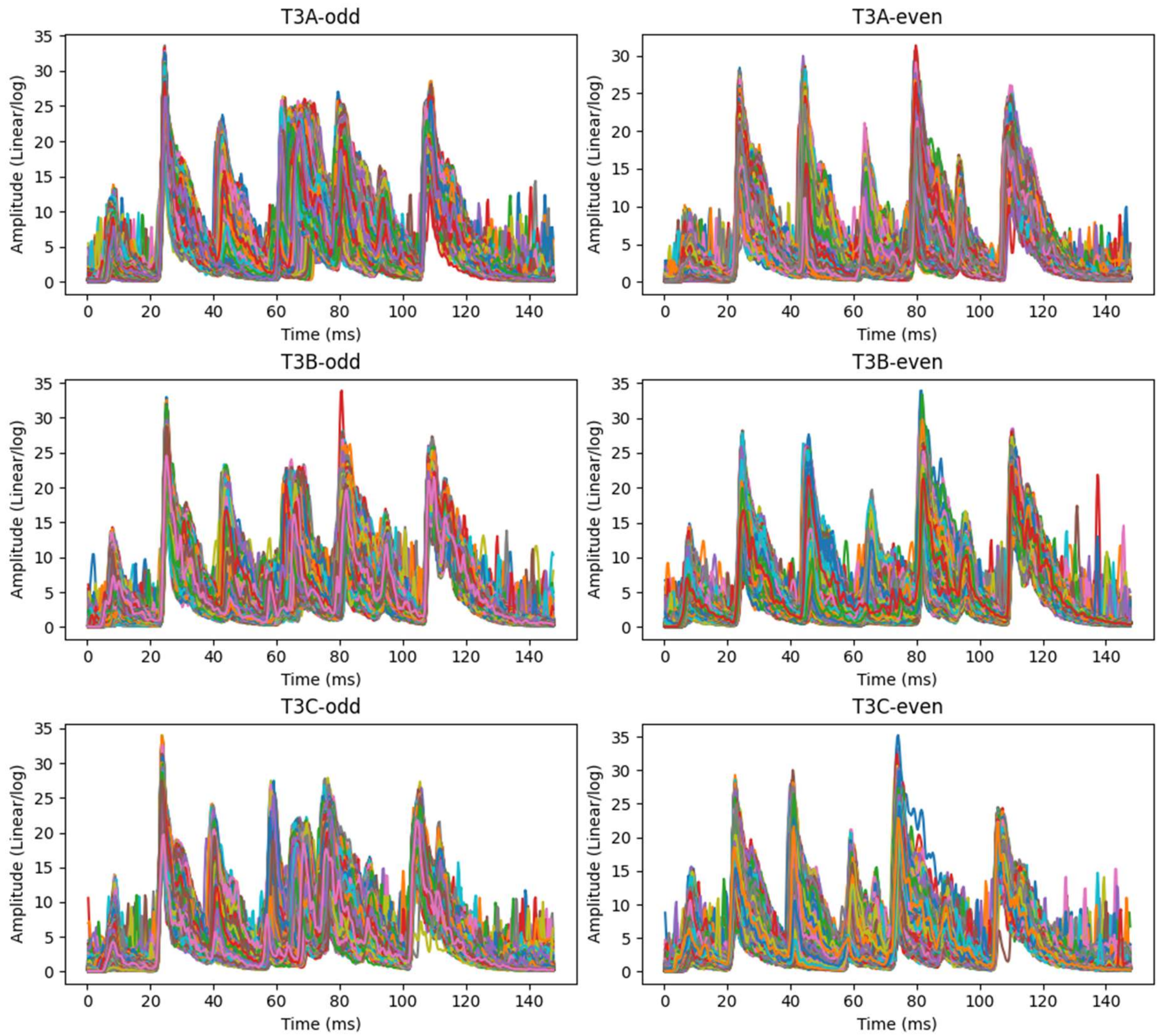

Figure VI.7 All envelopes in the datasets T3A-odd, T3B-odd, T3C-odd, T3A-even, T3B-even, and T3C-even are displayed in separate subfigures.

6.5.1. Encoding and visualization

The latent space has two dimensions, allowing each envelope to be displayed in a two-dimensional figure. The results of the training data for families T3A, T3B, and T3C are shown in Figures VI.8, VI.9, and VI.10, respectively. In these figures, subgraphs (a) and (b) present the envelopes in the two dimensions Z[0] and Z[1] from the latent space, using a color scale to represent measurements over years and temperature, respectively, aiding in the visualization of each envelope. As demonstrated in these figures, the distinction between the odd and even envelopes is visually clear. To further clarify this distinction, a red line has been added in subgraph (a) to separate the odd and even envelopes.

The boundaries are linearly separable. Therefore, as a simple approach, a perceptron with a single neuron can directly be used to classify the latent space data by category (into class A, class B or anomaly class) or by degree of membership depending on the type of activation function used (linear or sigmoid). The difficulty in this approach lies in the strategy of using target coding. However, in this work, a decoder is used to carry out and indirectly perform the categorization and classification.

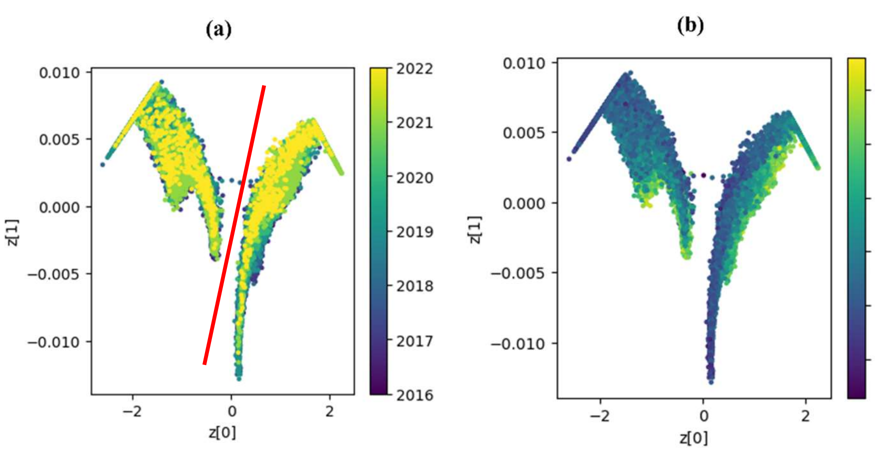

Figure VI.8 2D visualization of family T3A (both even and odd). Subgraph (a) employs a color scale to represent changes over years, while subgraph (b) utilizes a color scale to depict changes over temperature.

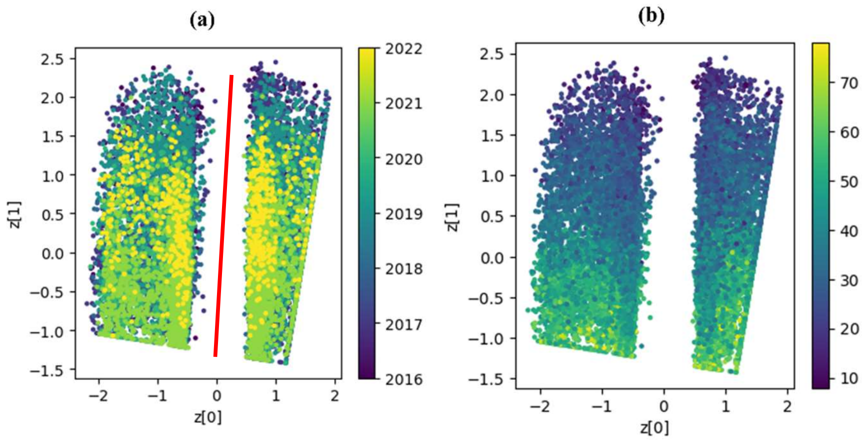

Figure VI.9 2D visualization of family T3B (both even and odd). Subgraph (a) employs a color scale to represent changes over years, while subgraph (b) utilizes a color scale to depict changes over temperature.

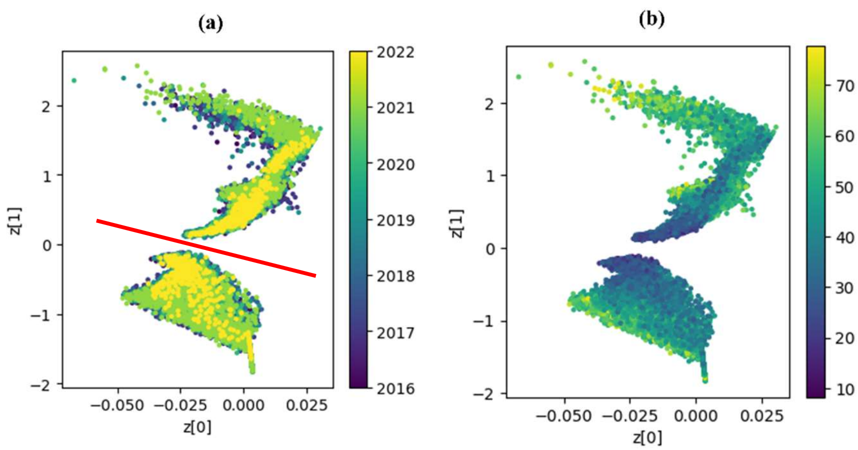

Figure VI.10 2D visualization of family T3C (both even and odd). Subgraph (a) employs a color scale to represent changes over years, while subgraph (b) utilizes a color scale to depict changes over temperature.

6.5.2. Generating envelopes

As mentioned previously, a distinctive feature of the CVAE network is its ability to generate envelopes both with and without distortions, relative to the distribution and representation of the real data. To accomplish this, data from the 2D space is selected and the decoder component of the network is utilized to generate the envelopes. For this purpose, a 10 × 10 grid coordinates in the latent space, linearly spaced, allows for the generation of 100 envelopes. Figure 11 displays the 100 generated envelopes for family T3A. All the envelopes shown in Figure VI.11 are different. It can be observed that the number, width, and height of peaks differ by exploring the envelopes generated at each point of the grid.

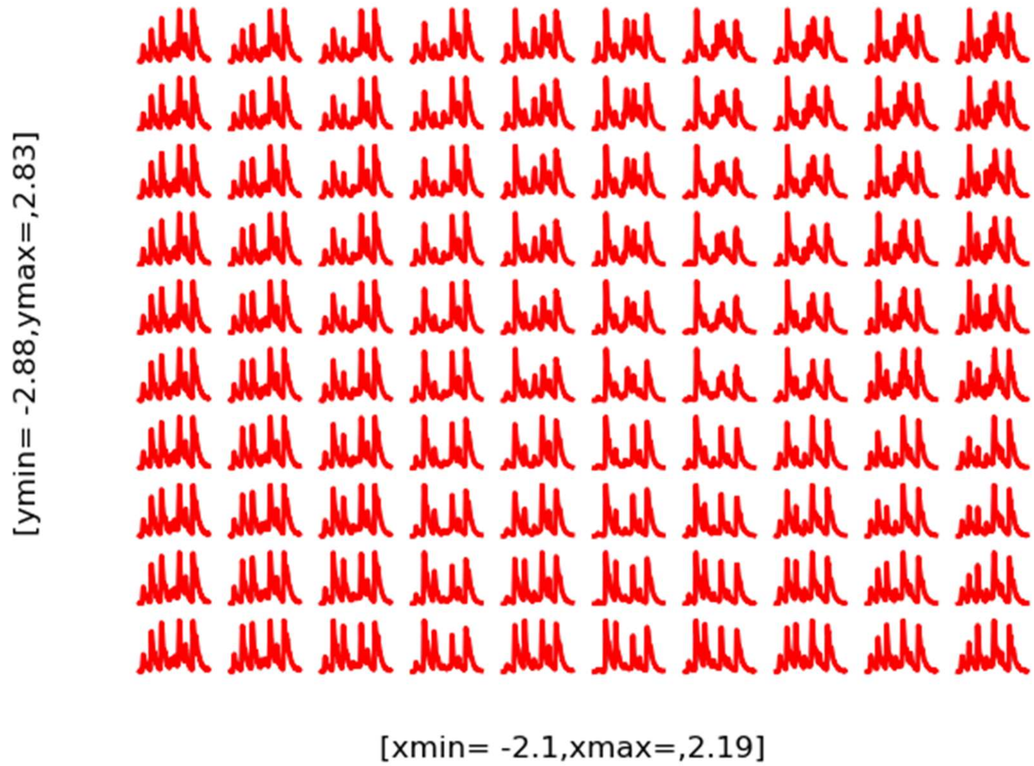

Figure VI.11 The 100 generated envelope in family T3A.

6.5.3. Detecting anomalies

The CVAE network can be used to detect anomalies by reconstructing the input envelopes. Two examples each from the odd and even envelopes in families T3A, T3B, and T3C are selected, with both the actual values and their reconstructions shown in Figures VI.12, VI.13 and VI.14, respectively. The actual and reconstructed envelopes are displayed using dotted and solid lines, respectively.

To detect anomalies, a threshold must be established. Three identical CVAE networks are trained for each family: T3A, T3B, and T3C. After training, the reconstruction errors for the training set of each network are calculated using absolute error and the maximum error is defined as the default threshold. The estimated default threshold values for the T3A, T3B, and T3C families are 0.13, 0.11, and 0.10, respectively.

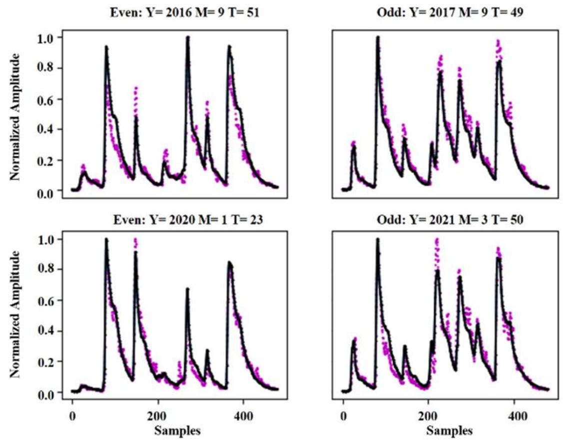

Figure VI.12 Two examples each from the odd and even envelopes in families T3A are selected. Both the actual values and their reconstructions are displayed, using dotted lines for the actual values and solid lines for the reconstructions.

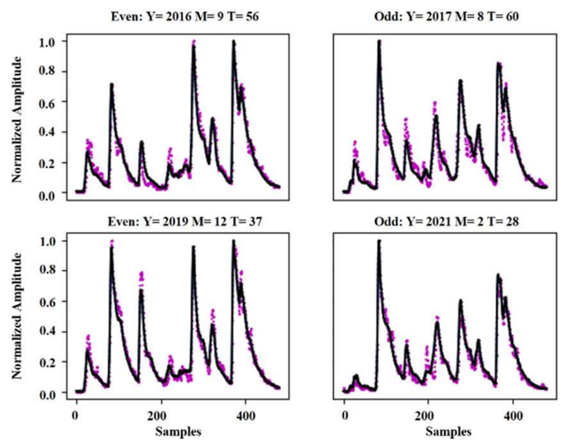

Figure VI.13 Two examples each from the odd and even envelopes in families T3B are selected. Both the actual values and their reconstructions are displayed, using dotted lines for the actual values and solid lines for the reconstructions.

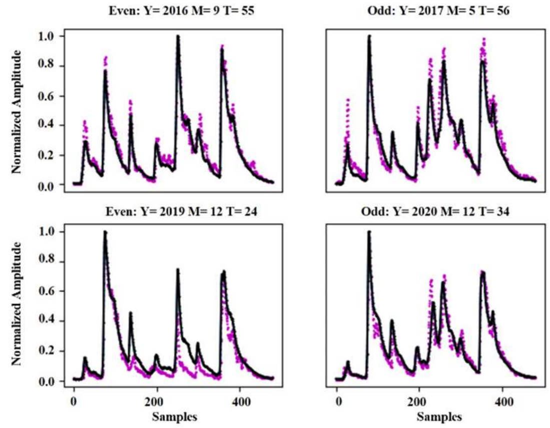

Figure VI.14 Two examples each from the odd and even envelopes in families T3C are selected. Both the actual values and their reconstructions are displayed, using dotted lines for the actual values and solid lines for the reconstructions.

To determine the optimal threshold, various percentages (ranging from 40% to 100%) of the default threshold are tested. The anomalies are detected by comparing the anomaly scores (reconstruction errors) to these thresholds. If the anomaly score exceeds the threshold, it is considered an anomaly.

When evaluating the performance of these thresholds on validation data from the same family that was not used for training, we aim to have a low number of anomalies to ensure the model's accuracy and generalization. However, when validation data from the other two families is used, we expect most of the data to be considered anomalies. This helps in distinguishing between different families and ensuring that the network can effectively detect anomalies in data it wasn't specifically trained on.

By testing these thresholds on both training and validation datasets, including data from other families, the optimal threshold for anomaly detection is identified. Tables VI.1, VI.2 and VI.3 present the percentage of detected anomalies at different threshold levels (ranging from 40% to 100% of the default threshold) for each family T3A, T3B, and T3C, respectively.

To be specified, all tests are performed separately for odd and even data type by family and the percentage of detected anomalies reported in Tables I, II and III is the mean of the even and odd.

In these tables, each row represents a different threshold level, while the columns show the results for training data, validation data from the same family, and validation data from the other two families. The first column, threshold (S), shows different percentages of the default threshold (e.g., 0.4*S means 40% of the default threshold). The explanation of the second to fourth columns in Table VI.1 regarding Network T3A is as follows:

- Family T3A Training Data: Anomalies detected in the training data of family T3A, the dataset that Network T3A is trained with it.
- Family T3A Validation Data: Anomalies detected in the validation data of family T3A, which is not used in the training step.
- Validation Data from Families T3B, T3C: Anomalies detected in the validation data from families T3B and T3C.

The explanation of the second to fourth columns in Tables VI.2 and VI.3 regarding Network T3B and Network T3C has the same structure and explanation as Network T3A.

In these tables, each row corresponds to a different threshold level, showing the percentage of anomalies detected. The optimal threshold is achieved if there is a small percentage of anomaly detection for the family being trained (both training and validation sets) and if most data from the other two families are considered anomalies. According to this strategy, optimal thresholds of 0.5*S, 0.5*S, and 0.7*S are achieved for families T3A, T3B, and T3C, respectively, which are shown in bold in Tables VI.1, VI2 and VI.3, respectively.

In future work, the impact of temperature on vibro-acoustic signals will be investigated, and efforts will be made to reduce or eliminate this effect. It should be noted that the effect of temperature is not the same on each sample of the signal envelope. Therefore, the first step is to investigate the effect of temperature on each sample to determine whether the effect is linear or non-linear. In the second step, two approaches, mathematical and neural network-based, will be employed to mitigate this impact. In the mathematical approach, we will try to find a mathematical relationship to reduce the effect. In the neural network approach, the effect will be removed by applying a method based on neural networks. These two approaches will be compared, and the best approach will be applied. Additionally, it is possible to use a combination of both approaches.

Table VI.1 Anomaly detection rates for networks T3A at various threshold levels. The table compares the percentage of anomalies detected in training data, validation data from the same family, and validation data from the other families for each network. S indicates the default threshold and is equal to 0.13 for family T3A.

Threshold	Family T3A		Families T3B, T3C
	Training data	Validation data	Validation data
0.4*S	14%	18%	100%
0.5*S	**3%**	**4%**	**99%**
*0.6*S*	1%	1%	90%
*0.7*S*	0%	0%	71%
*0.8*S*	0%	0%	38%
*0.9*S*	0%	0%	12%
1.0*S	0%	0%	3%

Table VI.2 Anomaly detection rates for networks T3B at various threshold levels. The table compares the percentage of anomalies detected in training data, validation data from the same family, and validation data from the other families for each network. S indicates the default threshold and is equal to 0.11 for family T3B.

Threshold	Family T3B		Families T3A, T3C
	Training data	Validation data	Validation data
0.4*S	11%	25%	100%
0.5*S	**2%**	**5%**	**99%**
*0.6*S*	0%	1%	96%
*0.7*S*	0%	0%	83%
*0.8*S*	0%	0%	65%
*0.9*S*	0%	0%	51%
1.0*S	0%	0%	40%

Table VI.3 Anomaly detection rates for networks T3C at various threshold levels. The table compares the percentage of anomalies detected in training data, validation data from the same family, and validation data from the other families for each network. S indicates the default threshold and is equal to 0.10 for family T3C.

Threshold	Family T3C		Families T3A, T3B
	Training data	Validation data	Validation data
0.4*S	35%	49%	100%
*0.5*S*	10%	17%	100%
*0.6*S*	2%	6%	100%
0.7*S	**1%**	**2%**	**100%**
*0.8*S*	0%	1%	98%
*0.9*S*	0%	0%	95%
1.0*S	0%	0%	90%

6.6. Conclusion

In this contribution, the monitoring of OLTC involves vibroacoustic signal analysis. A monitoring system was installed on three transformers, each equipped with sister OLTC units, and has continuously recorded their vibration signals and temperatures since 2016. The preprocessing steps included extracting the signal envelope and aligning the measured vibration signals in time. Subsequently, a deep learning technique known as CVAE was employed. The CVAE encodes and maps the higher-dimensional signal envelope into a 2D latent space, allowing for visualization and exploration of the boundaries and distribution of different data families. Simultaneously, the network's decoder reconstructs or generates signal envelopes by upsampling the low-dimensional latent vector. This model serves multiple purposes: visualizing signal envelopes on a 2D plot, generating new signal envelopes, and detecting anomalies. An anomaly detection threshold is defined based on the reconstruction error, which quantifies the absolute difference between the input signal envelope and the network's output. Throughout the research, various thresholds were evaluated, identifying one as optimal for anomaly detection. For each network, this optimal threshold was chosen to minimize false positives within its own family (from both training and validation sets), while maximizing detection of anomalies in the other two families (which were not used for training). The results demonstrate that the network effectively distinguishes its own family from unknown data, successfully identifying anomalies that may occur in the future. This capability highlights its potential for preemptive anomaly detection in OLTC operations. One potential limitation is that the threshold used to identify fault conditions can be sensitive to new samples, leading to the risk of miscalibration over time. This miscalibration can occur because new operating conditions or environmental factors can influence the acoustic signal, resulting in false positives or missed detections. Different strategies can be used to mitigate threshold sensitivity and miscalibration:

Adaptable thresholds: For example, machine learning techniques such as adaptive filtering or statistical models can be used to recalibrate thresholds continuously as the system collects more operational data.

Long-term learning: Over time, the monitoring system could "learn" the normal operational sounds of the OLTC. This would allow it to detect subtle anomalies by comparing real-time acoustic data to a baseline dataset that evolves gradually, reducing the chance of miscalibration.

Feature extraction methods such as Fourier Transforms or Wavelet Transforms can isolate the most relevant parts of the signal and reduce the impact of background noise or environmental factors.

Signal smoothing techniques can help reduce the effects of short-term fluctuations that could otherwise cause miscalibration.

Periodic recalibration based on the performance history of the OLTC may help ensuring that the system remains accurate.

Validation against known faults (from historical data or simulated tests) can help ensure the threshold settings are still appropriate for detecting true fault events without being overly sensitive to noise.

Chapitre VII
Conclusion

7.1. Résumé et principaux résultats

Cette recherche porte sur l'analyse du comportement des CPC à l'aide des enveloppes de signaux vibro-acoustiques. Les signaux ont été mesurés sur des CPC dans des conditions réelles. Un prétraitement, incluant l'extraction des enveloppes et l'alignement des enveloppes des signaux, a été effectué sur les signaux mesurés. De plus, des échelles logarithmiques et linéaires combinées ont été appliquées aux enveloppes des signaux vibro-acoustiques. Par la suite, cette recherche se concentre sur le développement d'une méthodologie pour détecter, localiser et suivre les changements dans les enveloppes des signaux de vibration comme première étape. Ensuite, les paramètres statistiques les mieux adaptés sont calculés à partir des enveloppes des signaux vibro-acoustiques, et les anomalies dans le comportement des CPC sont détectées à l'aide de l'apprentissage profond.

Les résultats significatifs obtenus dans cette thèse incluent :

- Une nouvelle méthodologie est proposée pour détecter et localiser les changements dans les enveloppes des signaux de vibration. Par conséquent, les pics principaux sont extraits pour cette détection et localisation. En fonction des emplacements de ces pics principaux, les zones principales sont également extraites des enveloppes. Par la suite, la métrique ED est calculée entre chaque zone/pic principal situé dans chaque enveloppe et la référence. Les résultats de la métrique ED sont utilisés pour déterminer s'il y a un déplacement dans l'enveloppe du signal de vibration.
- Chaque zone est analysée en fonction de paramètres statistiques, et les plus adaptés sont extraits à l'aide de la technique de régression linéaire, de la valeur-P et du R^2.
- Une architecture composée de deux secteurs, incluant un secteur hors ligne et un secteur en ligne, est utilisée pour détecter les anomalies dans les caractéristiques extraites (ED calculée à partir des zones) des enveloppes des signaux de vibration. Dans cette architecture, un autoencodeur convolutionnel et la KDE sont utilisés pour détecter les anomalies dans les signaux de vibration mesurés en continu. Dans le secteur hors ligne, l'autoencodeur

convolutionnel est entraîné avec des données normales et les erreurs de reconstruction sont ensuite calculées. Par la suite, la KDE est employée pour déterminer les scores d'anomalie et le seuil. Dans le secteur en ligne, le score d'anomalie de la mesure récente est obtenu en se basant sur le modèle entraîné et la KDE. Enfin, la mesure récente est considérée comme une anomalie si son score d'anomalie est inférieur à un seuil dynamique.

- Une autre architecture basée sur le CVAE est utilisée à plusieurs fins : visualiser les enveloppes de signal sur une figure 2D, générer des enveloppes de signal et détecter les anomalies dans les enveloppes de signaux vibro-acoustiques. Le seuil de détection des anomalies est défini en fonction de l'erreur de reconstruction, calculée comme la différence absolue entre l'entrée et la sortie du réseau. Divers seuils sont testés tout au long de cette recherche, avec un seuil identifié comme optimal pour la détection des anomalies. Pour chaque réseau, le seuil optimal est sélectionné pour garantir que seules quelques enveloppes de signal de sa propre famille (ensembles d'entraînement et de validation) sont considérées comme des anomalies, tandis que presque toutes les enveloppes de signal des deux autres familles (qui ne sont pas utilisées pour l'entraînement) sont considérées comme des anomalies. Les résultats démontrent que le réseau reconnaît efficacement sa propre famille et identifie les deux autres familles comme inconnues, distinguant ainsi avec succès les données connues des données inconnues. Cette capacité permet au réseau de détecter des anomalies potentielles futures.

7.2. Contributions de la recherche

Au cours du développement de la recherche doctorale, les articles suivants ont été produits, résumant les principaux résultats obtenus.

Trois articles de journaux:

1. Dabaghi-Zarandi, F., Behjat, V., Gauvin, M., Picher, P., Ezzaidi, H., & Fofana, I. Power Transformers OLTC Condition Monitoring Based on Feature Extraction from Vibro-Acoustic Signals: Main Peaks and Euclidean Distance. Sensors, **2023**, vol. 23, no 16, p. 7020.
2. Dabaghi-Zarandi, F., Behjat, V., Gauvin, M., Picher, P., Ezzaidi, H., & Fofana, I. Using Deep Learning to Detect Anomalies in On-Load Tap Changer Based on Vibro-Acoustic Signal Features. Energies, **2024**, vol.17, no 7, p.1665.
3. Dabaghi-Zarandi, F., Ezzaidi, H., Gauvin, M., Picher, P., Behjat, V., & Fofana, I. Convolutional Variational Autoencoder for Anomaly Detection in On-Load Tap Changers. IEEE Access, **2025,** vol.13, pp. 50838 - 50848

Et deux articles de conférence:

1. Dabaghi-Zarandi, F., Picher, P., Gauvin, M., Ezzaidi, H., Fofana, I., Mohan Rao, U., & Behjat, V. OLTC Contact Monitoring using Vibro-Acoustic Signals and Time Series Forecasting. CIGRE Conference & Expo. Calgary, Alberta, Canada. October 31 – November 3, **2022**.
2. Dabaghi-Zarandi, F., Picher, P., Gauvin, M., Ezzaidi, H., Fofana, I., Mohan Rao, U., Behjat, V., & Pedro da Costa Souza, J. Evaluating OLTC Condition Based on Feature Extraction from Vibro-Acoustic Signals. ISH, Glasgow, England. August 28 – September 1. **2023**.

7.3. Les recherches à venir et recommandations

Pour la continuité de ce sujet de recherche et pour aborder d'autres aspects de la surveillance des CPC basée sur l'analyse des signaux vibro-acoustiques, quelques sujets d'attention sont suggérés:

- **Prédiction du comportement futur des CPC :** Les contacts sont un composant important dans un CPC et ils se dégradent lentement avec le temps. La dégradation des contacts peut créer des changements dans les enveloppes des signaux de vibration au fil du temps. Il est possible de suivre ces changements et de prédire les évolutions futures. Il existe plusieurs algorithmes de prédiction différents, tels que les LSTM, qui sont utilisés pour prévoir les instances futures dans une série temporelle. En utilisant ces algorithmes, il est possible de prédire l'état futur des CPC et d'estimer le moment approximatif du remplacement des contacts.

- Investigation de l'impact de la température sur les signaux de vibration et tentative de réduction ou d'élimination de ses effets.
- Analyse des enveloppes des signaux de courant moteur.
- Essais de vieillissement en laboratoire avec différents modèles de changeurs de prise pour mieux comprendre les effets des mécanismes de dégradation sur les signaux vibro-acoustiques et le courant moteur.
- Investigation des zones silencieuses dans les signatures vibro-acoustiques (hors commutation).

Chapitre VIII
Appendice A : Pseudocodes des algorithmes pour l'extraction des pics principaux

8.1. Fenêtre dynamique

Le pseudocode de la procédure de fenêtre dynamique est illustré dans la Figure VIII.1. Les descriptions des lignes principales sont expliquées ci-dessous :

- **La ligne 1 :** L'entrée de l'algorithme comprend « reference_main_peaks », qui spécifie les positions des pics principaux dans la référence ; « signal_envelopes », qui contient toutes les enveloppes de signal mesurées ; « sample_size », spécifiant le nombre d'échantillons sélectionnés autour de la position de chaque pic nécessaire pour calculer la MSE entre chaque pic et le pic de référence (voir lignes 24 et 25) ; et « dynamic_window_size », qui détermine la taille de la fenêtre.
- **La line 2:** La matrice « all_main_peak_locations » est utilisée pour stocker les positions de tous les pics principaux dans chaque enveloppe de signal. Selon la taille de « reference_main_peaks » et le nombre de « signal_envelopes », les dimensions de la matrice « all_main_peak_locations » varient. Elle comporte des colonnes correspondant au nombre de « reference_main_peaks » et des lignes égales au nombre de « signal_envelopes ».
- **La ligne 3 :** Une pile LIFO est créée pour gérer le traitement de la fenêtre dynamique afin de trouver des pics.
- **La ligne 4 :** Un dictionnaire « missing_peaks » est créé pour stocker les pics principaux manquants dans les enveloppes (si un pic principal n'est pas trouvé).
- **La ligne 5 :** Une boucle for est définie pour répéter la procédure d'extraction des pics principaux pour chaque pic principal de la référence.
- **La ligne 6 :** Une autre boucle for est définie pour répéter la procédure pour toutes les enveloppes afin de trouver le pic.
- **Les lignes 10 à 14 :** Si aucun pic n'est trouvé à l'intérieur de la fenêtre dynamique, le pic principal de référence est remplacé par la position du pic principal des enveloppes précédentes stockées dans la pile LIFO. Cette étape continue jusqu'à ce qu'au moins un pic soit trouvé ou que la pile soit vide.
- **Les lignes 15 à 21 :** Si «peaks_found» est vide, cela indique qu'il n'y a pas de pics dans cette zone de l'enveloppe, et l'index du pic principal est stocké dans le dictionnaire « missing_peaks ».
- **Les lignes 22 à 30 :** Si plus d'un pic est trouvé à l'intérieur de la fenêtre dynamique, ces lignes de code sont utilisées pour sélectionner la meilleure position pour le pic principal. Il est à noter que dans ce pseudocode, la fonction EF1 est utilisée.
- **La ligne 41 :** La matrice « all_main_peak_locations » et le dictionnaire « missing_peaks », qui contiennent la position trouvée des pics principaux et les pics manquants dans chaque enveloppe, sont retournés.

```
Algorithm 1: Dynamic Window
procedure DYNAMIC_WINDOW(reference_main_peaks, signal_envelopes, sample_size, dynamic_window_size)
    Create a matrix named all_main_peak_locations  // Stores all main peaks
    Create a LIFO stack named lifo_stack
    Create a dictionary named missing_peaks  // Stors missing main peaks for each envelope
    For each index in range(len(reference_main_peaks)) do
        For each envelope in range(len(signal_envelopes)) do
            Place the center of the dynamic window on the position of the reference main peak.
            Copy lifo_stack to temporary_stack for processing
            peaks_found = Find all peaks within dynamic_window
            While peaks_found is empty and not temporary_stack.isEmpty() do
                temp_peak = temporary_stack.pop()  // Use temporary stack for processing
                reference_main_peaks[index] = temp_peak // Update the reference main peak with the main peak inside the stack
                peaks_found = Find all peaks within dynamic_window
            End While
            If peaks_found is empty then
                Write "No peak in this area"
                main_peak = None // Placeholder indicating no peak found
                If envelope not in missing_peaks then
                    missing_peaks[envelope] = []
                End If
                Append index to missing_peaks[envelope]  // Track the missing main peak index for this envelope
            Else if peaks_found has multiple peaks then
                Select two peaks with the highest and second-highest amplitude values, call them P1 and P2
                EF1_P1 = Calculate EF1 between P1 and reference main peak
                EF1_P2 = Calculate EF1 between P2 and reference main peak
                If EF1_P1 < EF1_P2 then
                    main_peak = P1
                Else
                    main_peak = P2
                End If
            Else
                main_peak = the peak in the peaks_found // Single peak found is automatically the main peak
            End If
            all_main_peak_locations[envelope, index] = main_peak
            If main_peak is not None then
                reference_main_peaks[index] = main_peak  // Update the reference main peak with the new main peak
                lifo_stack.push(main_peak)
            End If
        End for
    End for
    Return all_main_peak_locations, missing_peaks
end procedure
```

Figure VIII.1 Pseudocode de la fenêtre dynamique.

8.2. Fenêtre statique

Le pseudocode pour la fenêtre statique est affiché dans la Figure VIII.2. Les descriptions des principales lignes sont présentées ci-dessous :

- **La ligne 1 :** L'entrée de l'algorithme comprend « reference_main_peaks », qui spécifie les positions des pics principaux dans le pic de référence ; « signal_envelopes », qui englobe toutes les enveloppes de signal mesurées ; et « main_peak_positions », qui identifie les positions initiales des pics principaux dans chaque enveloppe de signal obtenues à partir des fenêtres dynamiques.

- **La ligne 2 :** La matrice « all_main_peak_locations » est utilisée pour enregistrer les positions de tous les pics principaux dans chaque enveloppe de signal. Elle comporte des colonnes correspondant à « reference_main_peaks » et des lignes correspondant au nombre de « signal_envelopes », respectivement.
- **La ligne 3 :** Un dictionnaire « missing_peaks » est créé pour stocker les pics principaux manquants dans les enveloppes (si un pic principal n'a pas été trouvé).
- **La ligne 4 :** Une boucle for est conçue pour exécuter de manière répétée la procédure d'extraction des pics principaux pour chaque pic de la référence.
- **Les lignes 5 à 7 :** Ces lignes sont utilisées pour déterminer la taille de la fenêtre statique en fonction des positions initiales des pics principaux obtenues par les fenêtres dynamiques.
- **La ligne 8 :** Le centre de la fenêtre statique est placé sur la position du pic de référence. Il contient la position du pic principal dans chaque enveloppe.
- **La ligne 9 :** Une autre boucle for est utilisée pour répéter la procédure dans toutes les enveloppes afin de trouver le pic.
- **Les lignes 11 à 24 :** Ces lignes sont utilisées pour extraire les pics à l'intérieur de la fenêtre statique. S'il n'y a pas de pics dans cette zone de l'enveloppe, l'index du pic principal est stocké dans le dictionnaire « missing_peaks ». S'il y a plus d'un pic, le pic avec la valeur la plus élevée est considéré comme le pic principal. S'il n'y a qu'un seul pic, il est considéré comme le pic principal.
- **La ligne 25 :** La position du pic principal est stockée dans la matrice « all_main_peak_locations ».
- **La ligne 28 :** La matrice « all_main_peak_locations » et le dictionnaire « missing_peaks » sont retournés, contenant respectivement les positions des pics principaux trouvés et des pics manquants (si aucun pic n'a été trouvé) pour chaque enveloppe.

```
Algorithm: Static Window
procedure STATIC_WINDOW(reference_main_peaks, main_peak_positions, signal_envelopes)
   Create an empty matrix named all_main_peak_locations // Stores all main peaks
   Create a dictionary named missing_peaks  // Stores missing main peaks for each envelope
   For each index in range(len(reference_main_peaks)) do
      min_peak_position = Find minimum value in main_peak_positions[:, index]
      max_peak_position = Find maximum value in main_peak_positions[:, index]
      static_window_size = max_peak_position - min_peak_position + 2
      Place the center of the static window on reference_main_peak [index]
      For each envelope_index in range(len(signal_envelopes)) do
         peaks_found = Find all peaks within static_window
         If no peaks are found then
            Write "No peak in this static window"
            main_peak = None // Placeholder indicating no peak found
            If envelope_index not in missing_peaks then
               missing_peaks[envelope_index] = []
            End If
            Append index to missing_peaks[envelope_index]  // Store the missing main peak index for this envelope
         Else
            If multiple peaks are found then
               main_peak = Select the peak with the highest amplitude
            Else
               main_peak = peaks_found // Single peak found is automatically the main peak
            End If
         End If
         all_main_peak_locations[envelope_index, index] = main_peak
      End for
   End for
   Return all_main_peak_locations, missing_peaks
end procedure
```

Figure VIII.2 Pseudocode de la Fenêtre Statique.

8.3. Algorithme de comparaison

Le pseudocode de l'algorithme de comparaison est illustré dans la Figure VIII.3. Les descriptions détaillées des lignes clés sont les suivantes :

- **La ligne 1 :** L'algorithme commence par prendre plusieurs entrées : « main_peak_results1 » et « main_peak_results2 », qui contiennent les résultats des pics principaux de deux fenêtres différentes ou de la même fenêtre avec des réglages variés ; « reference_main_peaks », spécifiant les positions des pics principaux de référence ; et « seuil», une valeur utilisée dans l'algorithme.
- **La ligne 2:** Une matrice nommée « final_main_peak_positions » est initialisée pour stocker les positions finales des pics principaux.
- **Les lignes 5 à 7 :** The algorithm computes the time distance between the positions of the peaks from both results of main peaks.
- **Les lignes 8 et 9 :** Si les positions initiales des deux résultats sont les mêmes, la position de main_peak_results1 est directement choisie sans autres vérifications.
- **Les lignes 10 à 17 :** Si cette distance est supérieure au seuil, la distance euclidienne (ED) est calculée entre chaque pic et le pic de référence. La position du pic la plus proche de la référence (ED plus petite) est sélectionnée comme pic principal.

- **Les lignes 18 à 25 :** Si la distance n'est pas supérieure au seuil, une métrique appelée EF2 est calculée pour chaque position par rapport au pic de référence. La position donnant la valeur EF2 la plus élevée est sélectionnée comme pic principal.
- **La line 27:** La position du pic principal sélectionnée est ajoutée à la matrice « final_main_peak_positions ».
- **La ligne 30 :** La matrice « final_main_peak_positions » est retournée, contenant les positions finales des pics principaux.

```
Algorithm: Comparison
1: procedure Comparison Algorithm(main_peak_results1, main_peak_results2, reference_main_peaks, seuil)
2:    Create an empty matrix named final_main_peak_positions with dimensions (number_of_envelopes, number_of_peaks)
3:    For each index in range(len(reference_main_peaks)) do
4:        For envelope in range(len(main_peak_results1)) do
5:            time1 = main_peak_results1[envelope, index].time
6:            time2 = main_peak_results2[envelope, index].time
7:            distance = abs(time1 - time2)
8:            If distance == 0 then
9:                selected_peak = main_peak_results1[envelope, index]  // Use the first result if the times are the same
10:           Else If distance > seuil then
11:               ED1 = calculate ED (time and amplitude) between main_peak_results1[envelope, index] and reference_main_peaks[index]
12:               ED2 = calculate ED (time and amplitude) between main_peak_results2[envelope, index] and reference_main_peaks[index]
13:               If ED1 < ED2 then
14:                   selected_peak = main_peak_results1[envelope, index]
15:               Else
16:                   selected_peak = main_peak_results2[envelope, index]
17:               End If
18:           Else
19:               EF2_1 = 1/ED1 + main_peak_results1[envelope, index].amplitude
20:               EF2_2 = 1/ED2 + main_peak_results2[envelope, index].amplitude
21:               If EF2_1 > EF2_2 then
22:                   selected_peak = main_peak_results1[envelope, index]
23:               Else
24:                   selected_peak = main_peak_results2[envelope, index]
25:               End If
26:           End If
27:           final_main_peak_positions[envelope, index] = selected_peak
28:       End for
29:   End for
30:   Return final_main_peak_positions
31: end procedure
```

Figure VIII.3 Pseudocode de l'Algorithme de Comparaison.

References

[1] T. Jayasree, I. Fofana, P. Rozga, U. M. Rao, K. Strzelecki, S. Brettschneider, P. Picher, E. R. Celis, and F. Stuchala, “Analysis of Breakdown Voltage of Low Pour Point Synthetic Ester Insulating Liquids under Lightning Impulse Voltage of both Polarities,” IEEE Transactions on Dielectrics and Electrical Insulation, vol. 31, no. 1, p. 254-262, 2023.

[2] K. Bacha, S. Souahlia, and M. Gossa, “Power transformer fault diagnosis based on dissolved gas analysis by support vector machine,” Electric power systems research, vol. 83, no. 1, pp. 73-79, 2012.

[3] A. Nanfak, E. Samuel, I. Fofana, F. Meghnefi, M. G. Ngaleu, and C. Hubert Kom, “Traditional fault diagnosis methods for mineral oil-immersed power transformer based on dissolved gas analysis: Past, present and future,” IET Nanodielectrics, vol. 7, no. 3, pp. 97-130, 2024.

[4] “Analysis of AC transformer reliability,” CIGRE WG A2.62, pp. Technical Brochure 939, 2024.

[5] R. Jongen, E. Gulski, and J. Erbrink, "Degradation Effects and Diagnosis of On-load Tap Changer in Power Transformers," p.8-11, 2014.

[6] M. Base, “On-load tap-changers for power transformers,” Regensburg, Germany, 2013.

[7] J. J. Erbrink, “On-load tap changer diagnosis on high-voltage power transformers using dynamic resistance measurements,” 2011.

[8] J. Liu, G. Wang, T. Zhao, and L. Zhang, “Fault diagnosis of on-load tap-changer based on variational mode decomposition and relevance vector machine,” Energies, vol. 10, no. 7, pp. 946, 2017.

[9] Z. Liu, X. Xia, S. Ji, Y. Shi, F. Zhang, Y. Fu, and Z. Jiang, "Fault diagnosis of OLTC based on time-frequency image analysis of vibration signal." Condition Monitoring and Diagnosis (CMD), Perth, WA, Australia, 23-26 September 2018, pp. 1-6.

[10] H. Cao, X. Wu, J. Zhou, X. Zhao, and J. Zhou, "Research progress on mechanical fault diagnosis of on-load tap changer based on vibration analysis." IEEE International Conference on Power Electronics, Computer Applications (ICPECA), Shenyang, China, 22-24 January 2021, pp. 948-951.

[11] B. Feizifar, Z. Müller, G. Fandi, and O. Usta, "A Collective Condition Monitoring Algorithm for On-Load Tap-Changers." Industrial and Commercial Power Systems Europe (EEEIC/I&CPS Europe), Genova, Italy, 1-14 June 2019, pp. 1-6.

[12] M. A. A. Aziz, M. A. Talib, and R. Arumugam, "Diagnosis of On-Load Tap Changer (OLTC) using dynamic resistance measurement." IEEE 8th International Power Engineering and Optimization Conference, Langkawi, Malaysia, 24-25 March 2014, pp. 494-497.

[13] F. B. Ismail, M. Mazwan, H. Al-Faiz, M. Marsadek, H. Hasini, A. Al-Bazi, and Y. Z. Yang Ghazali, “An Offline and Online Approach to the OLTC Condition Monitoring: A Review,” Energies, vol. 15, no. 17, pp. 6435, 2022.

[14] J. J. Erbrink, E. Gulski, J. J. Smit, P. P. Seitz, B. Quak, R. Leich, and R. Malewski, “Diagnosis of onload tap changer contact degradation by dynamic resistance measurements,” IEEE transactions on power delivery, vol. 25, no. 4, pp. 2121-2131, 2010.

[15] J. Seo, H. Ma, and T. K. Saha, “On Savitzky–Golay filtering for online condition monitoring of transformer on-load tap changer,” IEEE Transactions on Power Delivery, vol. 33, no. 4, pp. 1689-1698, 2017.

[16] J. Seo, H. Ma, and T. K. Saha, “A joint vibration and arcing measurement system for online condition monitoring of onload tap changer of the power transformer,” IEEE Transactions on Power Delivery, vol. 32, no. 2, pp. 1031-1038, 2016.

[17] F. Poza, P. Marino, S. Otero, and F. Machado, "Virtual instrument for condition monitoring of on-load tap changers." Third IEEE International Workshop on Electronic Design, Test and Applications (DELTA'06), Kuala Lumpur, Malaysia, 17-19 January 2006, pp. 5.

[18] Z. Li, Q. Li, Z. Wu, J. Yu, and R. Zheng, “A fault diagnosis method for on load tap changer of aerospace power grid based on the current detection,” IEEE Access, vol. 6, pp. 24148-24156, 2018.

[19] C. Plath, and M. Puetter, “Dynamic analysis and testing of on-load tap changer,” Transformers magazine, vol. 3, no. 3, pp. 104-109, 2016.

[20] F. Brikci, "Vibro-acoustic testing applied on tap changers and circuit breakers." In TechCon Innovation & Tchnology Conference, 2010.

[21] A. Secic, M. Krpan, and I. Kuzle, “Vibro-acoustic methods in the condition assessment of power transformers: A survey,” IEEE access, vol. 7, pp. 83915-83931, 2019.

[22] J. Seo, H. Ma, and T. K. Saha, "Analysis of vibration signal for power transformer on-load tap changer (OLTC) condition monitoring." IEEE Power & Energy Society General Meeting (PESGM), Portland, OR, USA, 05-10 August 2018, pp. 1-5.

[23] E. Rivas, J. C. Burgos, and J. C. Garcia-Prada, “Condition assessment of power OLTC by vibration analysis using wavelet transform,” IEEE Transactions on Power Delivery, vol. 24, no. 2, pp. 687-694, 2009.

[24] P. Kang, and D. Birtwhistle, “Characterisation of vibration sigsnals using continuous wavelet transform for condition assessment of on-load tap-changers,” Mechanical systems and signal processing, vol. 17, no. 3, pp. 561-577, 2003.

[25] E. Rivas, J. C. Burgos, and J. C. García-Prada, “Vibration analysis using envelope wavelet for detecting faults in the OLTC tap selector,” IEEE Transactions on Power Delivery, vol. 25, no. 3, pp. 1629-1636, 2010.

[26] S. Li, L. Dou, H. Li, Z. Li, and Y. Kang, “An Electromechanical Jointed Approach for Contact Pair Fault Diagnosis of Oil-Immersed On-Load Tap Changer,” Electronics, 12, no. 17,P. 3573, 2023.

[27] A. Cichoń, and M. Włodarz, “OLTC Fault detection Based on Acoustic Emission and Supported by Machine Learning,” Energies, vol. 17, no. 1, pp. 220, 2023.

[28] L. Cheim, “Transformer and Reactor Life Management.” Springer Nature, 2024.

[29] D. McPhail, “Condition analysis and assessment of on load tap changer acoustic monitoring principles and techniques,” Graduate Electrical Engineer—Ergon Energy, 2009.

[30] N. Gourov, "Diverter switch switching velocity measurement." 19th International Symposium on Electrical Apparatus and Technologies (SIELA), Bourgas, Bulgaria, 29 May 2016 - 01 June 2016, pp. 1-5.

[31] D. Shen, A. Kraemer, and D. Dohnal, "Vacuum switching technology improves the switching capacity of on-load tap-changers in HVDC applications." International Conference on Power System Technology, Chongqing, China, 22-26 October 2006, pp. 1-6.

[32] S. Gao, C. Zhou, Z. Zhang, J. Geng, R. He, Q. Yin, and C. Xing, "Mechanical fault diagnosis of an on-load tap changer by applying cuckoo search algorithm-based fuzzy weighted least squares support vector machine," Mathematical Problems in Engineering, vol. 2020, pp. 1-11, 2020.

[33] N. Abeywickrama, O. Kouzmine, S. Kornhuber, and P. Picher, "Application of novel algorithms for continuous bushing and OLTC monitoring for increasing newtwork reliability," Proceedings of the International Council on Large Electric systems (CIGRE), Paris, France, pp. 24-29, 2014.

[34] C. Wang, L. Lu, H. Ma, J.-p. Jin, and H. Zhang, "Diagnosis for loose switching contact fault of on-load tap-changer in transformer." CICED Proceedings, Nanjing, 13-16 September 2010, pp. 1-6.

[35] F. Dabaghi-Zarandi, P. Picher, M. Gauvin, H. Ezzaidi, I. Fofana, U. M. Rao, and V. Behjat, "OLTC Contact Monitoring using Vibro-Acoustic Signals and Time Series Forecasting", CIGRE-530 2022 CIGRE Canada Conference & Expo, Calgary, Alberta, October 31 – November3, 2022.

[36] E. Osmanbasic, and G. Skelo, "Tap changer condition assessment using dynamic resistance measurement," Procedia engineering, vol. 202, pp. 52-64, 2017.

[37] T. Bengtsson, H. Kols, L. Martinsson, M. Foata, F. Leonard, C. Rajotte, and J. Aubin, "Acoustic diagnosis of tap changers," International Council on Large Electric Systems (CIGRÉ), Paris, France, 1996.

[38] J. Seo, H. Ma, and T. K. Saha, "Vibration measurement and signal processing for condition assessment of OLTC of transformer." IEEE PES Asia-Pacific Power and Energy Engineering Conference (APPEEC), Brisbane, QLD, Australia, 15-18 November 2015, pp. 1-5.

[39] R. Bhuyan, A. R. Mor, P. Morshuis, G. C. Montanari, and W. Erinkveld, "Analysis of the arcing process in on-load tap changers by measuring the acoustic signature." IEEE Electrical Insulation Conference (EIC), Philadelphia, PA, USA, 08-11 June 2014, pp. 193-197.

[40] J. Seo, "A practical scheme for vibration signal measurement-based power transformer on-load tap changer condition monitoring." Condition Monitoring and Diagnosis (CMD), Perth, WA, Australia, 23-26 September 2018, pp. 1-4.

[41] Q. Huang, D. Zhang, H. Yang, R. Yang, L. Cheng, and X. Li, "Mechanical Fault Diagnostics of Power Transformer On-load Tap Changers Based on Marginal Point Distribution Coefficient." International Conference on Power System Technology (POWERCON), Guangzhou, China, 06-08 November 2018, pp. 3255-3261.

[42] R. Yang, D. Zhang, and Z. Li, "Vibration Analysis Using Variational Mode Decomposition for Mechanical Fault Diagnosis in The Diverter Switch of On-load Tap Changer." IEEE PES Innovative Smart Grid Technologies Europe (ISGT-Europe), Bucharest, Romania, 29 September 2019 - 02 October 2019, pp. 1-5.

[43] P. Picher, S. Riendeau, M. Gauvin, F. Léonard, L. Dupont, J. Goulet, and C. Rajotte, "New technologies for monitoring transformer tap-changers and bushings and their integration into a modern IT infrastructure." CIGRE: Paris, France, vol. 69, 2012.

[44] A. Kurapa, D. Rathore, D. R. Edla, A. Bablani, and V. Kuppili, “A hybrid approach for extracting EMG signals by filtering EEG data for IoT applications for immobile persons,” Wireless Personal Communications, vol. 114, pp. 3081-3101, 2020.

[45] O. Rioul, and M. Vetterli, “Wavelets and signal processing,” IEEE signal processing magazine, vol. 8, no. 4, pp. 14-38, 1991.

[46] W. K. Ngui, M. S. Leong, L. M. Hee, and A. M. Abdelrhman, “Wavelet analysis: mother wavelet selection methods,” Applied mechanics and materials, vol. 393, pp. 953-958, 2013.

[47] E. G. Plaza, and P. N. López, “Application of the wavelet packet transform to vibration signals for surface roughness monitoring in CNC turning operations,” Mechanical Systems and Signal Processing, vol. 98, pp. 902-919, 2018.

[48] H. Wang, and Y. Ji, “A revised Hilbert–Huang transform and its application to fault diagnosis in a rotor system,” Sensors, vol. 18, no. 12, pp. 4329, 2018.

[49] B. M. Battista, C. Knapp, T. McGee, and V. Goebel, “Application of the empirical mode decomposition and Hilbert-Huang transform to seismic reflection data,” Geophysics, vol. 72, no. 2, pp. H29-H37, 2007.

[50] L. Jin, and Y. Cai, "A review of fault diagnosis research on on-load tap-changers." E3S Web of Conferences, vol. 155, p. 01016,2020.

[51] N. Huang, “Overview of HHT Processing and the HHT-DPS,” White paper, NASA Goddard Space Flight Center, 2003.

[52] K. Dragomiretskiy, and D. Zosso, “Variational mode decomposition,” IEEE transactions on signal processing, vol. 62, no. 3, pp. 531-544, 2013.

[53] C. Pearson’s, “Comparison Of Values Of Pearson’s And Spearman’s Correlation Coefficients,” Comparison Of Values Of Pearson’s And Spearman’s Correlation Coefficients, 2011.

[54] A. M. Alsaqr, “Remarks on the use of Pearson’s and Spearman’s correlation coefficients in assessing relationships in ophthalmic data,” African Vision and Eye Health, vol. 80, no. 1, pp. 10, 2021.

[55] N. S. Chok, “Pearson's versus Spearman's and Kendall's correlation coefficients for continuous data,” Doctoral dissertation, University of Pittsburgh, 2010.

[56] P. Schober, C. Boer, and L. A. Schwarte, “Correlation coefficients: appropriate use and interpretation,” Anesthesia & analgesia, vol. 126, no. 5, pp. 1763-1768, 2018.

[57] F. Xie, F. Wang, Y. Zheng, and W. He, "Vibration Monitoring of On-load Tap-changer by Resonance-based Sparse Signal Decomposition." IEEE Power & Energy Society General Meeting (PESGM), Portland, OR, USA, 05-10 August 2018, pp. 1-5.

[58] P. Kang, and D. Birtwhistle, “Condition assessment of power transformer on-load tap-changers using wavelet analysis,” IEEE Transactions on Power Delivery, vol. 16, no. 3, pp. 394-400, 2001.

[59] X. Duan, T. Zhao, T. Li, J. Liu, L. Zou, and L. Zhang, “Method for diagnosis of on-load tap changer based on wavelet theory and support vector machine,” The Journal of Engineering, vol. 2017, no. 13, pp. 2193-2197, 2017.

[60] F. Wang, D. Zhou, and S. Zhang, "Mechanical condition monitoring of on-load tap changer based on textural features of recurrence plots of vibration signals." 5th International Conference on Electric Power Equipment - Switching Technology (ICEPE-ST), Kitakyushu, Japan, 08 December 2019, pp. 560-564.

[61] L. De Almeida, M. Fontana, F. Wegelin, and L. Ferreira, "A new approach for condition assessment of on-load tap-changers using discretewavelet transform." IEEE Instrumentationand Measurement Technology Conference Proceedings, Ottawa, ON, Canada, 16-19 May 2005, pp. 653-656.

[62] R. Shang, C. Peng, P. Shao, and R. Fang, "FFT-based equal-integral-bandwidth feature extraction of vibration signal of OLTC," Math. Biosci. Eng, vol. 18, no. 3, pp. 1966-1980, 2021.

[63] H. Li, L. Dou, S. Li, Y. Kang, X. Yang, and H. Dong, "Abnormal State Detection of OLTC Based on Improved Fuzzy C-means Clustering," Chinese Journal of Electrical Engineering, vol. 9, no. 1, pp. 129-141, 2023.

[64] J. Liu, G. Wang, T. Zhao, L. Shi, and L. Zhang, "The research of OLTC on-line detection system based on embedded and wireless sensor networks." IEEE International Conference on High Voltage Engineering and Application (ICHVE), Chengdu, China, 19-22 September 2016, pp. 1-4.

[65] P. Kang, and D. Birtwhistle, "Condition monitoring of power transformer on-load tap-changers. Part 2: Detection of ageing from vibration signatures," IEE Proceedings-Generation, Transmission and Distribution, vol. 148, no. 4, pp. 307-311, 2001.

[66] Z. Zhang, W. Chen, J. Lei, and H. Gu, "Vibration signal processing and state analysis technology for on-load tap-changer." International Conference on Diagnostics in Electrical Engineering (Diagnostika), Pilsen, Czech Republic, 01-04 September 2020, pp. 1-4.

[67] R. Duan, Y. Zuo, H. Zheng, R. Yao, M. Deng, and Z. Sun, "Condition monitoring of on-load tap-changers in converter transformers based on vibration method." 2nd IEEE Conference on Energy Internet and Energy System Integration (EI2), Beijing, China, 20-22 October 2018, pp. 1-6.

[68] C. Lin, D. Zhang, Q. Huang, R. Yang, J. Zhang, and J. Li, "Influence of load current on vibration signal of on-load tap changers." International Conference on Power System Technology (POWERCON), Guangzhou, China, 06-08 November 2018, pp. 3262-3268.

[69] J. Tu, and Y. Mi, "Research on transformer fast OLTC system." Journal of Physics: Conference Series, IOP Publishing, vol. 1187, p. 022002, 2019.

[70] S. Bustamante, M. Manana, A. Arroyo, A. Laso, and R. Martinez, "Determination of transformer oil contamination from the OLTC gases in the power transformers of a distribution system operator," Applied Sciences, vol. 10, no. 24, pp. 8897, 2020.

[71] U. M. Rao, I. Fofana, A. Bétié, M. Senoussaoui, M. Brahami, and E. Briosso, "Condition monitoring of in-service oil-filled transformers: Case studies and experience," IEEE Electrical Insulation Magazine, vol. 35, no. 6, pp. 33-42, 2019.

[72] D. Wotzka, and A. Cichoń, "Study on the influence of measuring AE sensor type on the effectiveness of OLTC defect classification," Sensors, vol. 20, no. 11, pp. 3095, 2020.

[73] W. Huang, C. Peng, L. Jin, J. Liu, and Y. Cai, "Fault Diagnosis of On-load Tap-changer Based on Vibration Signal." IOP Conference Series: Materials Science and Engineering, IOP Publishing, Vol. 605, No. 1, p. 012005. p. 012005, 2019.

[74] M. Gauvin, P. Picher, S. Riendeau, F. Léonard, and C. Rajotte, “Field experience with tapchanger and bushing monitoring,” CIGRE SC A, vol. 2, 2011.

[75] P. Picher, M. Gauvin, L. Vouligny, A. Zinflou, E. Frenette, S. Proulx, C. Rajotte, Development and implementation ofvtransformer condition monitoring models for the interpretation of sensor and SCADA data. CIGRE Sci. Eng. 2022. Availablevonline: https://cse.cigre.org/cse-n027/d1-development-and-implementation-of-transformer-condition-monitoring-modelsfor-the-interpretation-of-sensor-and-scada-data (accessed on 27 January 2023).

[76] B. J. LaMeres, "The Stack and Subroutines," Embedded Systems Design using the MSP430FR2355 LaunchPad™, pp. 247-254: Springer, 2023.

[77] M. Wang, A. J. Vandermaar, and K. D. Srivastava, “Review of condition assessment of power transformers in service,” IEEE Electrical insulation magazine, vol. 18, no. 6, pp. 12-25, 2002.

[78] J. Duan, Q. Zhao, L. Zhu, J. Zhang, and J. Hong, “Time-dependent system reliability analysis for mechanical on-load tap-changer with multiple failure modes,” Applied Mathematical Modelling, vol. 125, pp. 164-186, 2024.

[79] Y. Yan, Y. Qian, H. Ma, and C. Hu, “Research on imbalanced data fault diagnosis of on-load tap changers based on IGWO-WELM,” Math. Biosci. Eng, vol. 20, pp. 4877-4895, 2023.

[80] C. Zhang, W. Ren, Y. Chen, X. Yang, and D. Jiang, “Experimental investigation on electrical and mechanical vibration responses of diverter switches within OLTCs,” Electrical Engineering, vol. 106, no 1, p. 407-417, 2024.

[81] F. Dabaghi-Zarandi, V. Behjat, M. Gauvin, P. Picher, H. Ezzaidi, and I. Fofana, “Power Transformers OLTC Condition Monitoring Based on Feature Extraction from Vibro-Acoustic Signals: Main Peaks and Euclidean Distance,” Sensors, vol. 23, no. 16, pp. 7020, 2023.

[82] Y.-L. Li, and J.-R. Jiang, "Anomaly detection for non-stationary and non-periodic univariate time series." IEEE Eurasia Conference on IOT, Communication and Engineering (ECICE), Yunlin, Taiwan, 23-25 October 2020, pp. 177-179.

[83] L. Cheng, G. Dong, L. Ren, R. Yang, B. Liu, Y. Rong, and D. Li, "Anomaly detection and analysis based on deep autoencoder for the storage tank liquid level of oil depot." Journal of Physics: Conference Series, IOP Publishing, Vol. 2224. No. 1, p. 012013, 2022.

[84] G. Li, and J. J. Jung, “Deep learning for anomaly detection in multivariate time series: Approaches, applications, and challenges,” Information Fusion, vol. 91, pp. 93-102, 2023.

[85] T. Li, M. L. Comer, E. J. Delp, S. R. Desai, J. L. Mathieson, R. H. Foster, and M. W. Chan, "Anomaly scoring for prediction-based anomaly detection in time series." IEEE Aerospace Conference, Big Sky, MT, USA, 07-14 March 2020, pp. 1-7.

[86] N. Chen, H. Tu, X. Duan, L. Hu, and C. Guo, “Semisupervised anomaly detection of multivariate time series based on a variational autoencoder,” Applied Intelligence, vol. 53, no. 5, pp. 6074-6098, 2023.

[87] A. Dokumentov, and R. J. Hyndman, “STR: A seasonal-trend decomposition procedure based on regression,” Monash econometrics and business statistics working papers, vol. 13, no. 15, pp. 2015-13, 2015.

[88] A. Mishra, R. Sriharsha, and S. Zhong, “OnlineSTL: Scaling time series decomposition by 100x,” arXiv preprint arXiv:2107.09110, 2021.

[89] O. I. Provotar, Y. M. Linder, and M. M. Veres, "Unsupervised anomaly detection in time series using lstm-based autoencoders." IEEE International Conference on Advanced Trends in Information Theory (ATIT), Kyiv, Ukraine, 18-20 December 2019, pp. 513-517.

[90] S. Kim, W. Jo, and T. Shon, “APAD: Autoencoder-based payload anomaly detection for industrial IoE,” Applied Soft Computing, vol. 88, pp. 106017, 2020.

[91] H. D. Nguyen, K. P. Tran, S. Thomassey, and M. Hamad, “Forecasting and Anomaly Detection approaches using LSTM and LSTM Autoencoder techniques with the applications in supply chain management,” International Journal of Information Management, vol. 57, pp. 102282, 2021.

[92] J. An, and S. Cho, “Variational autoencoder based anomaly detection using reconstruction probability,” Special lecture on IE, vol. 2, no. 1, pp. 1-18, 2015.

[93] J. C. B. Gamboa, “Deep learning for time-series analysis,” arXiv preprint arXiv:1701.01887, 2017.

[94] P. Perera, P. Oza, and V. M. Patel, “One-class classification: A survey,” arXiv preprint arXiv:2101.03064, 2021.

[95] V. L. Cao, M. Nicolau, and J. McDermott, "One-class classification for anomaly detection with kernel density estimation and genetic programming." Genetic Programming: 19th European Conference, Porto, Portugal, March 30-April 1, 2016, pp. 3-18.

[96] F. Zhu, N. Ye, W. Yu, S. Xu, and G. Li, “Boundary detection and sample reduction for one-class support vector machines,” Neurocomputing, vol. 123, pp. 166-173, 2014.

[97] C. I. Lang, F.-K. Sun, B. Lawler, J. Dillon, A. Al Dujaili, J. Ruth, P. Cardillo, P. Alfred, A. Bowers, and A. Mckiernan, “One Class Process Anomaly Detection Using Kernel Density Estimation Methods,” IEEE Transactions on Semiconductor Manufacturing, vol. 35, no. 3, pp. 457-469, 2022.

[98] H. Chen, H. Liu, X. Chu, Q. Liu, and D. Xue, “Anomaly detection and critical SCADA parameters identification for wind turbines based on LSTM-AE neural network,” Renewable Energy, vol. 172, pp. 829-840, 2021.

[99] pavithrasv. "Timeseries anomaly detection using an Autoencoder," 2020/05/31; https://keras.io/examples/timeseries/timeseries_anomaly_detection/.

[100] W. Kim, S. Kim, J. Jeong, H. Kim, H. Lee, and B. D. Youn, “Digital twin approach for on-load tap changers using data-driven dynamic model updating and optimization-based operating condition estimation,” Mechanical Systems and Signal Processing, vol. 181, pp. 109471, 2022.

[101] M. Z. I. Chowdhury, and T. C. Turin, “Variable selection strategies and its importance in clinical prediction modelling,” Family medicine and community health, vol. 8, no. 1, 2020.

[102] J. M. Hahne, F. Biessmann, N. Jiang, H. Rehbaum, D. Farina, F. C. Meinecke, K.-R. Müller, and L. C. Parra, “Linear and nonlinear regression techniques for simultaneous and proportional myoelectric control,” IEEE Transactions on Neural Systems and Rehabilitation Engineering, vol. 22, no. 2, pp. 269-279, 2014.

[103] S. Riaz, H. Elahi, K. Javaid, and T. Shahzad, “Vibration feature extraction and analysis for fault diagnosis of rotating machinery-a literature survey,” Asia Pacific Journal of Multidisciplinary Research, vol. 5, no. 1, pp. 103-110, 2017.

[104] V. Behjat, and M. Mahvi, “Statistical approach for interpretation of power transformers frequency response analysis results,” IET Science, Measurement & Technology, vol. 9, no. 3, pp. 367-375, 2015.

[105] S. Tenbohlen, S. Coenen, M. Djamali, A. Müller, M. H. Samimi, and M. Siegel, “Diagnostic measurements for power transformers,” Energies, vol. 9, no. 5, pp. 347, 2016.

[106] A. A. Adekunle, I. Fofana, P. Picher, E. M. Rodriguez-Celis, and O. H. Arroyo-Fernandez, “Analyzing Transformer Insulation Paper Prognostics and Health Management: A Modeling Framework Perspective,” vol. 12, pp. 58349 - 5837, 2024.

[107] A. Hussain, S.-J. Lee, M.-S. Choi, and F. Brikci, “An expert system for acoustic diagnosis of power circuit breakers and on-load tap changers,” Expert Systems with Applications, vol. 42, no. 24, pp. 9426-9433, 2015.

[108] S. Li, L. Dou, H. Li, Z. Li, and Y. Kang, “An Innovative Electromechanical Joint Approach for Contact Pair Fault Diagnosis of Oil-Immersed On-Load Tap Changer,” Electronics, vol. 12, no. 17, pp. 3573, 2023.

[109] C. Fan, F. Xiao, Y. Zhao, and J. Wang, “Analytical investigation of autoencoder-based methods for unsupervised anomaly detection in building energy data,” Applied energy, vol. 211, pp. 1123-1135, 2018.

[110] M. Memarzadeh, B. Matthews, and I. Avrekh, “Unsupervised anomaly detection in flight data using convolutional variational auto-encoder,” Aerospace, vol. 7, no. 8, pp. 115, 2020.

[111] L. Erhan, M. Ndubuaku, M. Di Mauro, W. Song, M. Chen, G. Fortino, O. Bagdasar, and A. Liotta, “Smart anomaly detection in sensor systems: A multi-perspective review,” Information Fusion, vol. 67, pp. 64-79, 2021.

[112] S. Zavrak, and M. Iskefiyeli, “Anomaly-based intrusion detection from network flow features using variational autoencoder,” IEEE Access, vol. 8, pp. 108346-108358, 2020.

[113] S. Mishra, and S. Jabin, “Anomaly detection in surveillance videos using deep autoencoder,” International Journal of Information Technology, vol. 16, no. 2, pp. 1111-1122, 2024.

[114] V. Toufigh, and I. Ranjbar, “Unsupervised deep learning framework for ultrasonic-based distributed damage detection in concrete: integration of a deep auto-encoder and Isolation Forest for anomaly detection,” Structural Health Monitoring, vol. 23, no. 3, pp. 1313-1333, 2024.

[115] F. Dabaghi-Zarandi, V. Behjat, M. Gauvin, P. Picher, H. Ezzaidi, and I. Fofana, “Using Deep Learning to Detect Anomalies in On-Load Tap Changer Based on Vibro-Acoustic Signal Features,” Energies, vol. 17, no. 7, pp. 1665, 2024.

[116] Y. Alanazi, M. Schram, K. Rajput, S. Goldenberg, L. Vidyaratne, C. Pappas, M. I. Radaideh, D. Lu, P. Ramuhalli, and S. Cousineau, “Multi-module-based CVAE to predict HVCM faults in the SNS accelerator,” Machine Learning with Applications, vol. 13, pp. 100484, 2023.

[117] J. Jakubowski, P. Stanisz, S. Bobek, and G. J. Nalepa, “Anomaly detection in asset degradation process using variational autoencoder and explanations,” Sensors, vol. 22, no. 1, pp. 291, 2021.

[118] Y. Fan, G. Wen, D. Li, S. Qiu, M. D. Levine, and F. Xiao, “Video anomaly detection and localization via gaussian mixture fully convolutional variational autoencoder,” Computer Vision and Image Understanding, vol. 195, pp. 102920, 2020.

[119] V. Zilvan, A. Ramdan, A. Heryana, D. Krisnandi, E. Suryawati, R. S. Yuwana, R. B. S. Kusumo, and H. F. Pardede, “Convolutional variational autoencoder-based feature learning for automatic tea clone recognition,” Journal of King Saud University-Computer and Information Sciences, vol. 34, no. 6, pp. 3332-3342, 2022.

[120] R. Zemouri, M. Levesque, N. Amyot, C. Hudon, O. Kokoko, and S. A. Tahan, “Deep convolutional variational autoencoder as a 2d-visualization tool for partial discharge source classification in hydrogenerators,” IEEE Access, vol. 8, pp. 5438-5454, 2019.

[121] A. Proteau, R. Zemouri, A. Tahan, and M. Thomas, “Dimension reduction and 2D-visualization for early change of state detection in a machining process with a variational autoencoder approach,” The International Journal of Advanced Manufacturing Technology, vol. 111, pp. 3597-3611, 2020.

[122] S. Lu, X. Tang, Y. Zhu, and J. She, "A cloud-edge collaborative intelligent fault diagnosis method based on LSTM-VAE hybrid model." IEEE International Conference on Cyber Security and Cloud Computing (CSCloud)/ 7th IEEE International Conference on Edge Computing and Scalable Cloud (EdgeCom), Washington, DC, USA, 26-28 June 2021, pp. 207-212.

[123] D. Kim, and C. J. Matyas, “Classification of tropical cyclone rain patterns using convolutional autoencoder,” Scientific Reports, vol. 14, no. 1, pp. 791, 2024.

[124] E. Lin, S. Mukherjee, and S. Kannan, “A deep adversarial variational autoencoder model for dimensionality reduction in single-cell RNA sequencing analysis,” BMC bioinformatics, vol. 21, pp. 1-11, 2020.

[125] K. Wang, C. Yan, Y. Mo, Y. Wang, X. Yuan, and C. Liu, “Anomaly detection using large-scale multimode industrial data: An integration method of nonstationary kernel and autoencoder,” Engineering Applications of Artificial Intelligence, vol. 131, pp. 107839, 2024.

[126] A. Borghesi, A. Bartolini, M. Lombardi, M. Milano, and L. Benini, "Anomaly detection using autoencoders in high performance computing systems." Proceedings of the AAAI Conference on artificial intelligence, Vol. 33, No. 01, pp. 9428-9433, 2019.

[127] Y. Su, Y. Zhao, C. Niu, R. Liu, W. Sun, and D. Pei, "Robust anomaly detection for multivariate time series through stochastic recurrent neural network." Proceedings of the 25th ACM SIGKDD international conference on knowledge discovery & data mining, pp. 2828-2837, 2019.

[128] C. Sun, Z. He, H. Lin, L. Cai, H. Cai, and M. Gao, “Anomaly detection of power battery pack using gated recurrent units based variational autoencoder,” Applied Soft Computing, vol. 132, pp. 109903, 2023.

[129] S. M. Lee, S.-Y. Park, and B.-H. Choi, “Application of domain-adaptive convolutional variational autoencoder for stress-state prediction,” Knowledge-Based Systems, vol. 248, pp. 108827, 2022.

[130] X. Yan, D. She, and Y. Xu, “Deep order-wavelet convolutional variational autoencoder for fault identification of rolling bearing under fluctuating speed conditions,” Expert Systems with Applications, vol. 216, pp. 119479, 2023.

[131] fchollet. "Variational AutoEncoder," 2020/05/03; https://keras.io/examples/generative/vae/.